Field relationships and evolution of leucocratic, basic veins at El Porticito volcanic vent, New Mexico

by

Robert R. Horning

Submitted in Partial Fulfillment of the

Requirements of the Degree of

Master of Science in Geology

August, 1997

Department of Earth and Environmental Science

New Mexico Institute of Mining and Technology

Socorro, New Mexico, USA

ABSTRACT

El Porticito is a butte, composed of lava and interpreted to be the eroded remnant of a volcanic vent. It is located in the transition zone between the Colorado Plateau and the Basin and Range province in west-central New Mexico, USA. It is distinguished by the striking white, vertical and horizontal, millimeter- to meter-scale, coarse-grained tephritic veins that cut across the black basanite faces of the edifice. The leucocratic color of the veins is controlled by their mineralogy: black, coarse-grained augite and iron-titanium oxide crystals set in a finer-grained white groundmass consisting of alkali feldspar, nepheline, zeolites and analcime.

Substantial whole rock compositional variation within veins is due to variable concentrations of the relatively sparse augite and Fe-Ti oxide phenocrysts, flow segregation of the phenocrysts, and subordinately to post-emplacement alteration. Augite phenocryst compositions and morphologies record a cyclic growth history that was strongly influenced by varying Ti activity during vein melt cooling.

The veins occur within only one of the two basanites that constitute the bulk of El Porticito. Major and compatible trace element data suggest that vein magma evolved at depth through crystal fractionation from the older, less-evolved basanite. Stratigraphic relationships indicate that vein magma then intruded the younger basanite while the latter cooled through the rheological critical melt percentage.

Geochemical modeling suggests that the basanites crystallized from distinct parent magmas that had undergone different degrees of evolution from a common mantle source in which garnet remained in the restite. Compatible trace element concentrations preclude the evolution of one basanite from the other. The Mn and Ca contents of the cores of olivine phenocrysts found in the basanites suggest equilibration at different depths with magmas having comparable Si and Fe activities, while rim compositions reflect distinct chemical conditions in the host basanites during final crystal growth.

ACKNOWLEDGMENTS

The author wishes to thank J. M. Farren, D. P. Miggins, and W. B. Vandermolen for invaluable assistance in the field; M. G. Snow for extensive help with the electron microprobe at the Los Alamos National Laboratory ; W. C. McIntosh, L. Peters and R. P. Esser, of the New Mexico Geochronology Research Laboratory at NMT for $^{40}Ar/^{39}Ar$ dating; P. R. Kyle and C. G. McKee for assistance in the X-ray Fluorescence and INAA laboratories at NMT; L. A. Brandvold for precious metals analyses at the New Mexico Bureau of Mines and Mineral Resources Chemistry Lab; and O. T. Ramo of the Academy of Finland for $^{143}Nd/^{144}Nd$ analyses. P. R. Kyle provided preliminary major and trace element analyses of samples from El Porticito. K. Panter provided assistance in mass balance modeling. Special thanks are due N. G. Baca for allowing access to the study area. The author would particularly like to thank his advisors, N. W. Dunbar and P. R. Kyle and his graduate committee consisting also of W. S. Baldridge and A. R. Campbell for their guidance in this study. The XRF lab at NMT was partially funded by NSF grant (EAR93-16467). The New Mexico Bureau of Mines and Mineral Resources provided partial funding, which is greatly appreciated, for this study.

TABLE OF CONTENTS

Abstract	i
Acknowledgments	iii
Table of Contents	iv
List of Illustrations	vii
List of Tables	viii
Introduction	1
Geologic Setting	3
Previous Work	5
Field Relationships	6
El Porticito	7
Tejana Mesa	13
Eruptive Sequence	16
Analytical Procedures	17
Results	19
Petrography	19
Pyroclastic deposits, Tp	19
Early basanite, Tepb1	19
Late basanite, Tepb2	21
Veins, Tepv	22
Mineral Chemistry	27

Olivines 27
Pyroxenes 30
Feldspars 34
Fe-Ti oxides 34
Whole Rock Geochemistry 36
Dating 45
Discussion 47
Petrogenesis 47
Mass balance models 47
Veins 47
Late Basanite 54
Mantle derivation models 55
Vein Color 60
Emplacement Model 61
Post-emplacement Alteration 69
Conclusions 71
Appendix A: Microprobe Mineral Analysis 73
Olivines 75
Pyroxenes 82
Feldspars 93
Nephelines 99

Fe-Ti oxides 100

Appendix B: Thin Section Petrography 102

Appendix C: Whole Rock Compositions 123

Appendix D: Pyroclastic deposits stratigraphic column 131

Appendix E: Sample Locations 132

References 134

List of Illustrations

Figure 1: Geologic map 4

Figure 2: East face of El Porticito 8

Figure 3: Stratigraphic columns of El Porticito and Tejana Mesa 9

Figure 4: Vein in brittle fracture 11

Figure 5: Vein textures 12

Figure 6: Vein complex 15

Figure 7: Exsolved Fe-Ti oxide crystal 25

Figure 8: Pyroxene and olivine compositions 28

Figure 9: MnO *vs.* CaO in olivines 29

Figure 10: Al and Ti in pyroxenes 33

Figure 11: Feldspar compositions 35

Figure 12: Total alkalis *vs.* SiO_2 37

Figure 13: MgO variation diagrams 39

Figure 14: Compatible trace element concentrations 41

Figure 15: Normalized incompatible trace element spidergram 43

Figure 16: Normalized rare earth element concentrations 44

Figure 17: Zr/Y *vs.* Zr/Nb of El Porticito rocks 58

Figure 18: K_2O/Th *vs.* La/Ta of El Porticito rocks 59

Figure 19: Emplacement model 63

Plate 1: Sample location map Pocket

List of Tables

Table 1: Generalized Petrographic Summary 20

Table 2: Summary of $^{40}Ar/^{39}Ar$ Results 46

Table 3: Representative Mineral Compositions 48

Table 4: Major Element Mass Balance Summary 50

Table 5: Measured and Calculated Trace Element Concentrations 51

Table 6: Published Mineral/Melt Partition Coefficients 52

INTRODUCTION

Veins and pods of evolved silicate rocks are found within a wide variety of crystalline host bodies. Such veins occur in the Shonkin Sag laccolith, Montana (Barksdale, 1937; Hurlbut & Griggs, 1939); Antarctic diabases (Hamilton *et al.*, 1965); the Slaufrudalur granophyre intrusion, Iceland (Saemundsson, 1979); the Makaopuhi and Kilauea Iki lava lakes, Hawaii (Peterson & Moore, 1987); the flood basalts of the Hartford Basin, Connecticut (Philpotts, *et al.*, 1996); and the Columbia River Basalt province, Washington (Puffer & Horter, 1993).

Sources of vein magma include the mush of the lower (Marsh *et al.*, 1991) and, in the case of Hawaiian lava lakes, upper (Helz *et al.*, 1989) solidification zones of the crystallizing bodies. The formation of magmatic veins and pods depends upon three processes: evolution and separation of vein magma from its source, transport to its destination, and emplacement into space created in the host. Mechanisms involved in separation of vein melt from the crystallizing lower solidification zone include crystal mush compaction (Helz *et al.*, 1989) and upward or lateral porous flow of low density liquid through the crystal mush (Philpotts *et al.*, 1996). Ascent of relatively low density vein magma to the zone of emplacement may be facilitated by (1) the formation of diapirs that ascend through intervening melt or along magma chamber walls, as in La Gloria pluton, Chile, (Mahood & Cornejo, 1992) and Kilauea Iki lava lake (Helz *et al.*, 1989); (2) entrainment of melt in streams of vesicles propagating

through intervening melt (Helz *et al.*, 1989, Puffer & Horter, 1993); or (3) formation of vertical pipes through nearly solid magma, as at Shonkin Sag (Marsh *et al.*, 1991).

The space needed for vein emplacement is provided by dilation and formation of cracks in the crystal mush within or above the upper solidification front. These cracks may result when pore pressure exceeds the tensile strength of the crystal mush in the upper zone (Philpotts & Carroll, 1996), by thermal contraction of crystallizing magma, by gravity-induced tearing of the crystal mush, or by detachment and foundering of solid roof rock (Marsh *et al.*, 1991).

Vein magma may become depleted of crystal nuclei by porous flow through a mesh of interlocking crystals (Philpotts *et al.*, 1996) or by fusion caused by heating while traversing higher temperature magma in the largely uncrystallized, central portion of a chamber, dike, or flow (Puffer & Horter, 1993). This depletion of nuclei increases the likelihood that veins will have the coarse textures often observed.

At El Porticito and adjacent Tejana Mesa, one sees striking centimeter to meter scale, coarse grained, white tephrite veins set in black, fine grained basanite. At El Porticito, veins appear as horizontal, elongate anastomozing arrays and isolated bodies with subjacent interconnecting vertical pipes or dikes. At Tejana Mesa, a latticework of subvertical veins merge upward into a single 10 m thick subhorizontal vein that extends some 200 m along the cliff

face. The purpose of this paper is to describe the vein and host rocks of El Porticito and adjacent Tejana Mesa and to postulate the processes by which they formed.

GEOLOGIC SETTING

El Porticito is located in the transition zone (Menzies *et al.*, 1991) between the Colorado Plateau and the Basin and Range province in west-central New Mexico. It lies near the southern margin of the Jemez Lineament (Fig. 1) (Chapin *et al.*, 1978), an alignment of volcanic centers extending northeast from the White Mountains in eastern Arizona, across the Rio Grande Rift, to the Raton-Clayton Volcanic Field of northeastern New Mexico. The lineament has been interpreted as coinciding with the buried boundary between the Proterozoic Yavapai and Mazatzal crustal provinces (Karlstrom & Bowring, 1993; Karlstrom and Daniel, 1993).

Geophysical studies have shown that the regional upper mantle P-wave velocity is 5-8% lower under the Rio Grande rift, southeastern Colorado Plateau transition zone, and Basin and Range province than beneath the Great Plains (Davis *et al.*, 1984; Parker *et al.*, 1984; Spence & Gross, 1990; Slack *et al.*, 1996). Data provided by Slack *et al.* (1996) indicate a zone of particularly low seismic velocities near the southeastern margin of the Colorado Plateau. This zone has a NE trend, intermediate between those of the Jemez Lineament and the Rio Grande rift. The data are permissive of, but do not require, up to ~1%

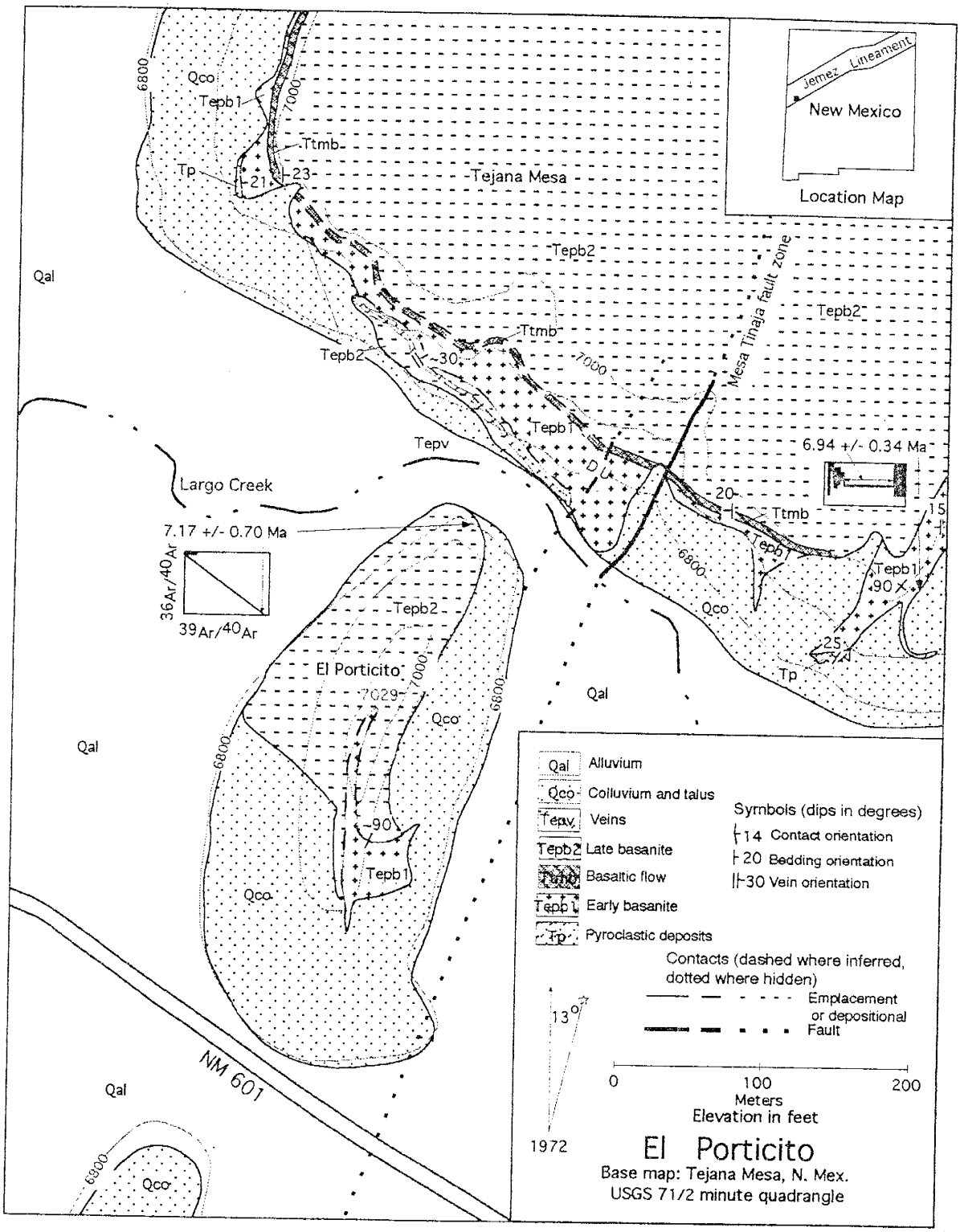

Fig. 1: Geologic map of El Porticito and nearby Tejana Mesa. The portion of Tejana Mesa included in the study area is a small projection of the landform, which extends northward approximately 10 km.

partial melt. The vertical velocity anomaly (averaged through the depth range of 35 to 255 km) beneath El Porticito is ~-7% relative to the Great Plains region (Slack *et al.*, 1996, Fig. 10). Spence & Gross (1990) had earlier detected a low velocity anomaly in the area and suggested that it might indicate a zone of weakness, or flaw, in the lithosphere which could provide conduits for ascending magmas from the mantle. However, Slack *et al.* (1996) concluded that multiple phases of extension and magmatism early in the history of the Rio Grande rift would have annealed Precambrian lower crustal-lithospheric mantle "flaws" so that they would play little or no role in subsequent events.

Minier & Reiter (1991) observed anomalously high heat flow in numerous shallow wells in the central Jemez Lineament. They inferred the existence of a NE trending basement fracture zone centered ~6 km NW of El Porticito. This zone may have influenced the location of the Mesa Tinaja fault, which passes within ~50 m of the East face of El Porticito, and probably controlled its location and orientation (Fig. 1). Several other volcanic vents occur along the Mesa Tinaja fault outside the current study area (Chamberlin *et al.*, 1994).

PREVIOUS WORK

Most previous geologic investigations that have included El Porticito have been regional (e.g., Willard & Weber, 1958) or topical (e.g., Roybal, 1982) in nature. A comprehensive general geologic study of Tejana Mesa, NE of El Porticito, was made by Guilinger (1982). He reported a maximum vertical

offset on the Mesa Tinaja fault (which he called the Tejana Mesa fault zone) of ~75 m, and observed the "graben-like" feature in which the present study area is included. He also noted in passing the "dike-like geometry" of El Porticito.

Within the present study area, Baldridge *et al.* (1989) and Baldridge (1994) briefly described the volcanic stratigraphy of El Porticito and adjacent Tejana Mesa and the vein petrography and the compositions of vein minerals. They noted particularly the textures that distinguish veins from host lavas.

Two studies have reported measured ages for the volcanic rocks of El Porticito and nearby Tejana Mesa. Dethier *et al.* (1986) obtained a K-Ar age of 6.73 ± 0.18 Ma for volcanic rocks capping Tejana Mesa about 1.1 km NE of El Porticito. More recently, McIntosh & Cather (1994) reported an $^{40}Ar/^{39}Ar$ plateau age of 7.92 ± 0.40 Ma (2σ) for a whole rock sample (nm1104) of basanite (here mapped as Tepb2) taken from El Porticito.

FIELD RELATIONSHIPS

El Porticito is a ~70 m high, elongate basaltic body located approximately 8 km NW of Quemado, New Mexico (Fig. 1), interpreted by Chamberlin *et al.* (1994) to be a "fissure vent". Tejana Mesa, across Largo Creek from El Porticito, is of somewhat greater height and extends northwards some 10 km. The portion of Tejana Mesa included in Fig. 1 is but a small protrusion from the SW corner of the mesa. This protrusion is bounded on the

E and W sides by canyons cut into the lava cap and underlying sedimentary deposits.

El Porticito

El Porticito consists of two fine-grained, melanocratic basanite units, Tepb1 and Tepb2, and numerous leucocratic tephrite/phonotephrite veins, Tepv (Figs. 2 and 3). Both basanite units are fine grained and generally structureless. In outcrop and hand specimen, these units have very similar color and mineralogy; but weathered surface textures can usually be employed to distinguish them. The first-erupted unit, Tepb1, can be distinguished in outcrop by its relatively fresh appearance and smoothly weathered surfaces. Near the S end of the E side of El Porticito, Tepb1 exhibits a strong joint pattern, with joints striking ~N7°E and dipping ~80°E, suggesting that Tepb1 is texturally foliated in this area. The second black basanite unit, Tepb2, usually has a rough, knobby weathered surface. The contact between the two basanite units is approximately vertical on the E side of El Porticito (Figs. 1 & 2).

Intruding Tepb2 are leucocratic, holocrystalline, porphyritic, non-vesicular tephrite/phonotephrite veins, ranging in orientation from vertical to horizontal and in thickness from ≤1 cm to ≥2 m (Figs. 2 and 3). Large, anastomosing arrays of horizontal veins are present in the northern portion of the outcrop, and smaller arrays are found to the south. Horizontal vein thickness increases

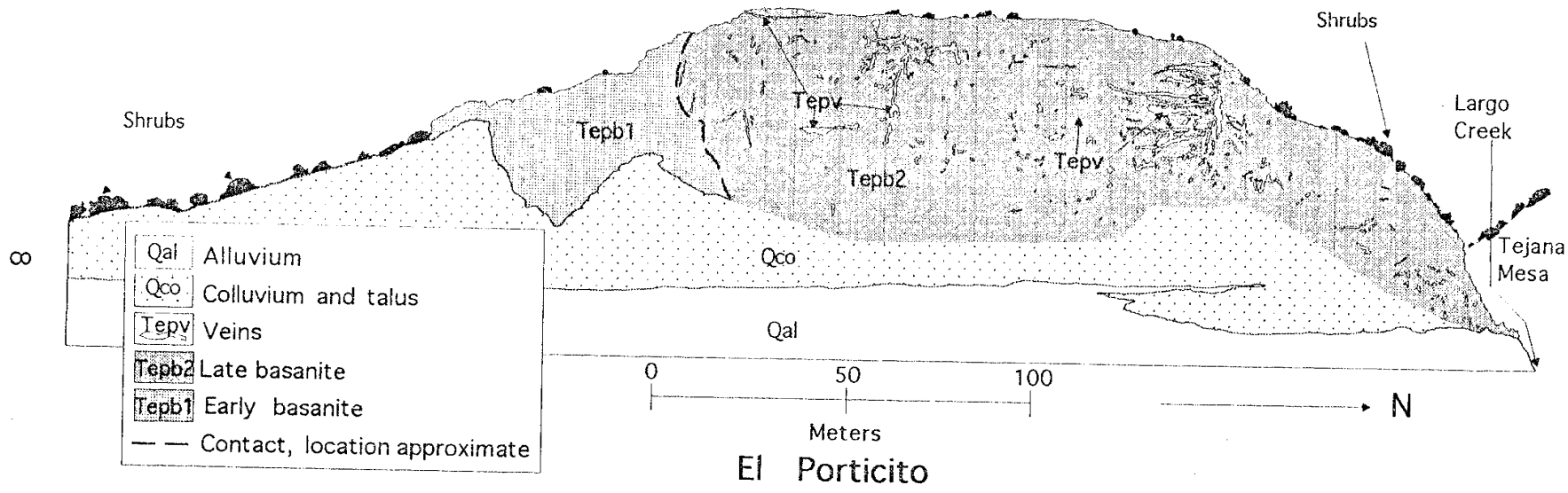

Fig. 2: Outcrop pattern of the east face of El Porticito taken from photos. Only the largest white veins (Tepv) are shown, and these only occur in the more evolved black basanite unit, Tepb2. The surface of Tepb1 exposed at the S (left) end of the outcrop exhibits prominent jointing. Note the inferred near vertical contact between Tepb1 and Tepb2.

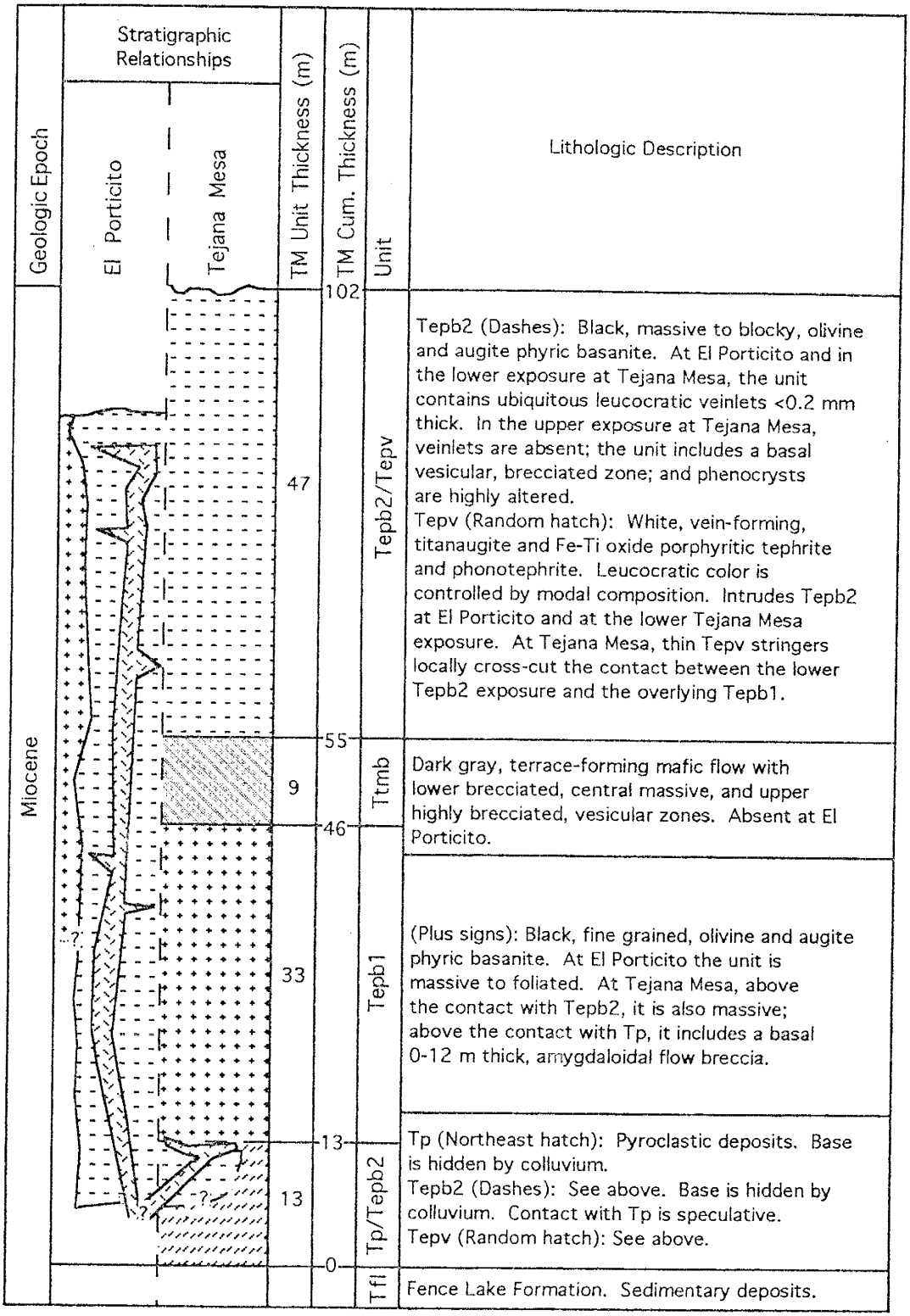

Fig. 3: Stratigraphic columns of volcanic deposits of El Porticito and nearby Tejana Mesa. Unit thicknesses at Tejana Mesa vary considerably with location, as shown in Fig. 1.

upward, reaching a maximum about 85% of the way up the E side of El Porticito. Above this level, thickness decreases dramatically; and at the top veins are generally ≤1 cm thick. Beneath and between these horizontal arrays are subvertical veins of generally lesser thickness. Subvertical veins occasionally form upward-merging patterns similar to the roots of large trees beneath horizontal arrays. Most veins follow smoothly-curved paths through the host, suggesting generally ductile deformation during vein emplacement. Veins tend to remain consistently coarse-grained up to within ~10 m of the top of El Porticito, suggesting similar thermal conditions throughout most of edifice. But in at least one location a vein twice changes orientation abruptly (Fig. 4). This is interpreted to indicate that magma at this location was intruded into a brittlely deformed fracture.

Many veins exhibit internal textures that indicate magma flow, such as phenocryst concentrations along magmatic flow foliations (Fig. 5). Partially to completely detached fragments of Tepb2, some decimeters in length, can be seen in outcrop and hand specimen included in veins. Very small, mafic crystals along the vein-wall rock interface can also be seen in Fig. 5. These appear to have nucleated and grown in place after flow had essentially ceased. Thin cracks, usually filled by silicate phases, are frequently observed following vein-wall rock interfaces.

Leucocratic veinlets, typically <0.2 mm in thickness and a few cm in length, are common throughout the vein-hosting unit, Tepb2, and probably

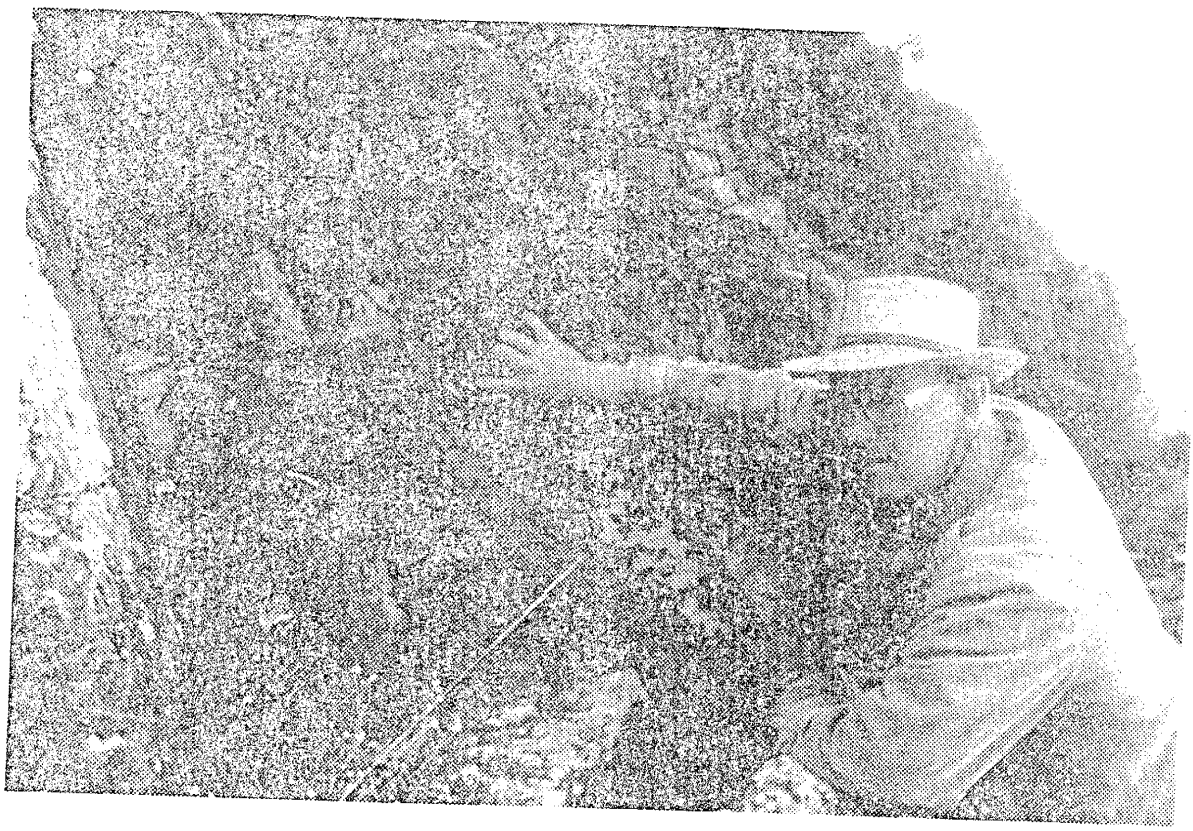

Fig. 4: Photo of vein occupying angular, brittle fracture at N end of El Porticito. Brittle fracture suggests that this portion of El Porticito had cooled more than most before vein magma was entruded.

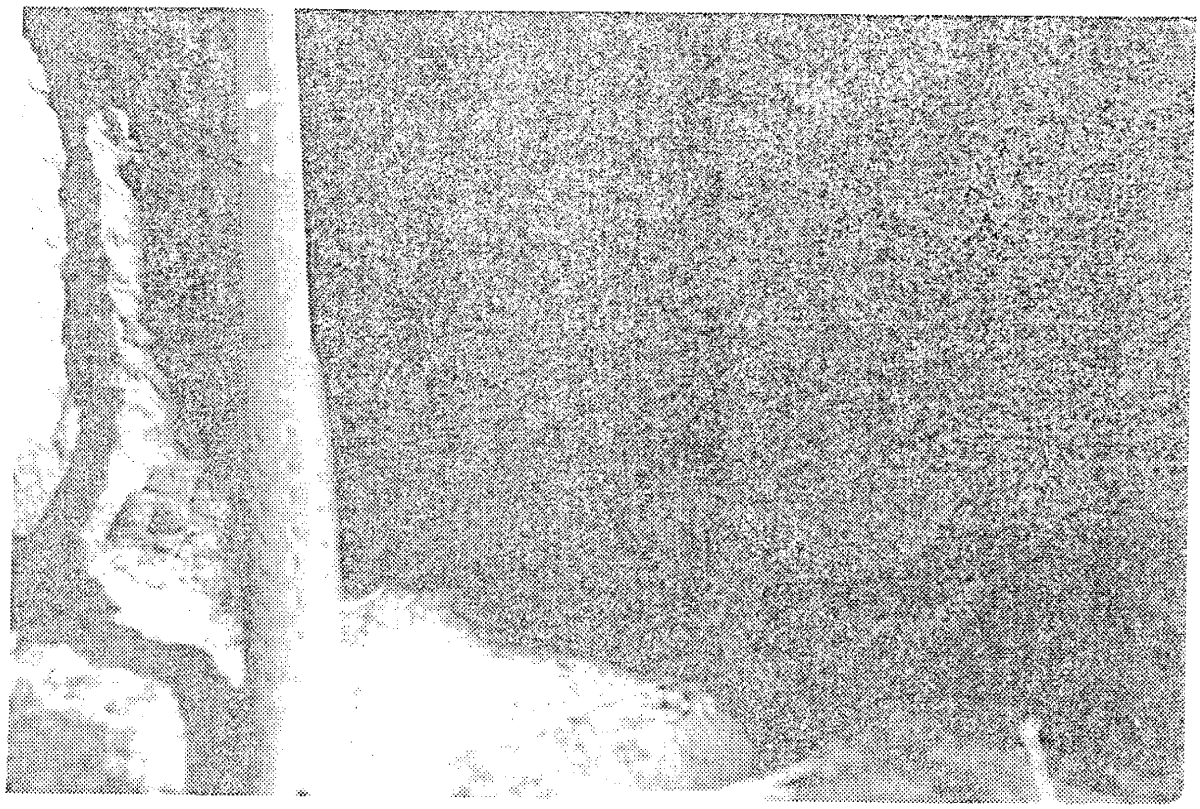

Fig. 5: Photo illustrating vein textures resulting from magma flow. Note concentrations of mafic phenocrysts in irregular patches and along flow foliations. Note also the very small mafic phenocrysts that nucleated on, and are still attached to, wall rock. Hammer grip is 3.5 cm wide.

account for its knobby appearance. These veinlets occasionally cross vein-wall rock interfaces, but more often grade into veins. All observed veinlets have a horizontal orientation, and are composed of silicate phases.

Tejana Mesa

The stratigraphically lowest volcanic rocks in the study area consist of pyroclastic deposits of limited exposure near the base of Tejana Mesa (Fig. 1). The lower contacts of these deposits are hidden by colluvium, but shallow excavations reveal poorly consolidated, scoriaceous lapillistones. Overlying these are structureless to cross-bedded, often agglutinated, pyroclastic breccias, lapilli tuffs, lapillistones, and tuffs. Bombs found in the deposits are subspherical to flattened and range up to ~0.6 m in maximum dimension. Bombs tend to be more oxidized at the SE corner of Tejana Mesa than at the SW corner. Observed vesicles in bombs tend to be spherical; and most are <2 mm in diameter. Calcite frequently lines, and sometimes fills, vesicles. Some bombs exhibit distinctive surface streamlines, interpreted as having formed during flight from their source vent.

Dark-colored, coarse-grained tephra deposits are probably products of magmatic eruptions; light-colored, fine-grained, laminated beds, some of which contain mafic, vesicular bombs, are considered to be phreatomagmatic in origin. The internal structures of the tephra layers are interpreted to indicate

that they are wet and dry surge deposits (Cas & Wright, 1993) that possibly formed part of a tuff ring.

Overlying the pyroclastic deposits are aphyric, black lava flows with upper and lower vesicular zones (Aubele *et al.*, 1988) and brecciated bases. As will be discussed later, the lowest of these units is chemically and petrographically indistinguishable from the first-erupted basanite of El Porticito, and is here mapped as the same unit, Tepb1. A ~6 m thick, fine-grained unit of Tepb1 composition also crops out near the top of the SE corner of Tejana Mesa. The unit's orientation changes from vertical to 15° W dip (Fig. 1). This unit is interpreted to constitute a small Tepb1 fissure vent and its flow.

West of the Mesa Tinaja fault, Tepb2 locally crops out at the upper boundary of colluvium and talus beneath Tepb1 (Fig. 1). Because the lower contact of this Tepb2 outcrop is hidden, it is unclear whether it intruded beneath, or into, Tepb1. This Tepb2 unit is interpreted to be a mafic sill. A complex of leucocratic veins (Fig. 6) indistinguishable from Tepv at El Porticito, cut Tepb2 at a high angle and merge upward to form a ≤10 m thick leucocratic sill at the contact between the two black lavas. Rarely, centimeter-scale veins extend above the leucocratic sill into the overlying Tepb1. The Tepv sill pinches out toward the northwest and repeatedly breaks up into thinner strands toward the southeast. No leucocratic veins have been observed southeast of the western strand of the Mesa Tinaja fault shown in Fig. 1.

Fig. 6: Photo of complex of veins penetrating Tepb2 beneath the 10 m thick subhorizontal vein near the base of Tejana Mesa, about 75 m NW of the Mesa Tinaja fault. Notebook is 19.5 cm tall.

Resting atop Tepb1 is a narrow terrace that slopes toward the Mesa Tinaja fault. Unit Ttmb (Figs. 1 and 3) defines this terrace. Ttmb, but apparently not the lava above it, is offset, down to the northwest, a few meters by the western strand of the Mesa Tinaja fault. East of the fault, Ttmb dips west and the terrace is quite prominent. West of the fault, the flow dips east and outcrops are discontinuous, tending to be covered by talus.

As will be discussed later, the lava flow overlying Ttmb is geochemically indistinguishable from Tepb2 of El Porticito. This unit is therefore interpreted to be part of Tepb2 in Figs. 1 and 3. No veins have been observed in this rock, but a few veinlets occur in it at the SW corner of Tejana Mesa. The Tepb2 flow thickens markedly toward the Mesa Tinaja fault; probably indicating that this flow filled a structurally-controlled paleovalley underlain by Ttmb.

Eruptive Sequence

In summary, the first eruptive products were the pyroclastic deposits, Tp, now found at Tejana Mesa. Tepb1 occurs as a flow unit lying atop Tp at Tejana Mesa, and in turn is overlain by the Ttmb flow. Tepb2 is found both above Ttmb (as a flow unit) and beneath Tepb1 at Tejana Mesa, and beside Tepb1 at El Porticito. Thus Tepb2 followed Tepb1 and Ttmb. At Tejana Mesa, veins intrude both Tepb1 and the lower outcrop of Tepb2, indicating that Tepv postdated both lavas.

ANALYTICAL PROCEDURES

Mineral compositions in thin sections of representative rock specimens were determined employing standard procedures with a Caméca model SX50 electron microprobe at the Los Alamos National Laboratory (LANL). A 10 μm diameter, 10 nA, 15 kV beam was used for most measurements. Calibrations were performed using several natural and synthetic standards (Appendix A). Matrix effects were corrected using the PAP procedure (Pouchou & Pichoir, 1985). The manufacturer's software was used to calculate elemental and oxide concentrations.

In preparation for whole rock chemical analyses, three hundred gm to 1 kg splits (Iyengar *et al.*, in press), depending upon maximum grain size in the sample, were crushed with a steel rotating plate wheel grinder. Selected samples were then subjected to repeated leaching in 3% acetic acid solutions until effervescence ceased, to remove any calcite that might be present. After drying at 100°C for at least 1 hour, samples were ground to 10 μm, or finer, powder using a tungsten carbide swing mill.

Whole rock compositional analyses were performed at the New Mexico Institute of Mining and Technology (NMT) X-ray Fluorescence Lab employing a Philips model PW2400 XRF spectrometer on fused disks for major element oxides, and pressed powder pellets for selected minor and trace elements (Norrish & Chappell, 1977, Hallett & Kyle, 1993).

Concentrations of major element oxides were determined in glass disks formed by mixing 1 gm aliquots of sample powder with 6 gm Sigma Chemicals type 12-22 X-ray flux, 0.05 gm LiBr, and 0.05 gm NH_4NO_3; fusing in Pt, 5% Au, crucibles for 4 to 5 minutes; and forming in a heated Pt casting dish. Adsorbed moisture of each sample was determined by measuring weight loss during drying of a ~3 gm aliquot for at least two hours at 100°C. True loss on ignition, LOI, was then determined by measuring the weight loss during ignition at 1000°C for an additional two hours. The dry analyses reported in Appendix C have been corrected for the weight lost during the drying step; and the LOI reported is the weight lost during the ignition step.

Concentrations of V, Ni, Cu, Zn, Ga, Rb, Sr, Y, Zr, Nb, Mo, Ba, and Pb were measured using wavelength dispersive XRF on pressed powder pellets. Pellets were prepared by first mixing 6 gm aliquots of sample with 6 drops of 2% polyvinyl alcohol binder. The mixture was then poured into a 3.5 cm diameter die, boric acid powder was added to form a backing, and the assembly was pressed at 15 tonnes.

The trace elements Sc, Cr, As, Sb, Cs, La, Ce, Nd, Sm, Eu, Tb, Yb, Lu, Hf, Ta, Th, and U were measured by INAA at NMT. Approximately 100 mg samples were packed in ultrapure silica vials and irradiated at the University of Missouri Research Reactor for 24 hours at a neutron flux density of 2.5×10^{13} $n \cdot cm^{-2} \cdot s^{-1}$. Samples were counted using two high purity Ge detectors (with resolutions of 1.8 kev at 1332 kev and 25% efficiency) 7 to 10 and 30 to 40

days following irradiation. NIST standard SRM 1633a was used for calibration (Hallett and Kyle, 1993).

RESULTS

Petrography

Pyroclastic deposits, Tp

Bombs found in tephra deposits are microporphyritic and amygdaloidal (Table 1). A single thin section (27D in Appendix B) reveals an opaque groundmass that includes tabular to subequant microphenocrysts of augite (≤40 μm long) and abundant anhedral to euhedral Fe-Ti oxides (≤5 μm across) set in a glassy matrix. Some, but not all, oxide grains exhibit irregular exsolution blebs and lamellae.

Phenocrysts include fractured, altered, euhedral to subhedral augite crystals to 500 μm (23% of total phases as visually estimated in thin section); fractured, euhedral to subhedral olivine crystals to 300 μm (11%); and minor euhedral feldspar.

Early basanite, Tepb1

Tepb1 is fine grained to finely porphyritic and holocrystalline (Table 1). In a thin section of sample 19A (Appendix B), the groundmass consists primarily of ≤50 μm augite tablets (68% of total phases). These have slightly

Table 1: Generalized petrographic summary of El Porticito and adjacent Tejana Mesa volcanic units

Rock Type	Unit	Texture	Ol	Aug	TAug	FT	Hem	Ksp	Ano	Ne	Ap	Ana	Ser	Zeo	Cla	Ca	Gl
Bombs	Tp	ves, amg, mp (<5)	a	a		g, p		tr							p	p	g, a
Basanite lava	Tepb1	fg→fp, str→ves, str→fb (<5)	a		p	p		g, tr				g, tr			g, tr	g, tr	
Melano-cratic lava	Ttmb	ves, fb															g, a(?) g, p(?)
Basanite lava	Tepb2	mp→fp, str→ves, str→fb, (<5)	a		a	p→a		g, p→a		g, tr	tr	g, tr→p	g, tr		g, tr		
Tephrite veins	Tepv	fp→cp, str→fl (20 - 60)		tr	p→a	p→a	tr	g, a	tr	g, p	g, p	g, p→a	g, p→a	g, tr→a	g, tr→p	g, tr	

abbreviations: *minerals* Ol = olivine; Aug = augite; TAug = Titanaugite; FT = Fe-Ti oxides; Hem = hematite; Ksp = potassic feldspar; Ano = anorthoclase; Ne = nepheline; Ap = apatite; Ana = analcime; Ser = sericite; Zeo = zeolites; Cla = clay; Ca = calcite; Gl = glass
concentrations tr = trace (≤1%); p = present (>1%); a = abundant (>10%); g = groundmass only
textures amg = amygdaloidal; ves = vesicular; str = structureless; fb = flow brecciated; fl = flow lineations; cp = coarsely porphyritic (phenos >5 mm); fg = fine grained, fp = finely porphyritic (phenos >2 mm); mp = microporphyritic (<2 mm). Proportion of phenocrysts >2 mm is given to nearest 5% in parentheses.

lobate margins, which are probably growth features, and tend to be aligned around the sides of phenocrysts, as during flow. Other groundmass phases (12%) include irregular grains of exsolved Fe-Ti oxides and a few grains of interstitial feldspar and small clay masses.

Anhedral to subhedral, fractured olivine (16%) is the dominant phenocrystic phase, with grains ranging up to 3 mm across. Some margins are rimmed with Fe-Ti oxide grains, and fractures tend to be filled with chlorophaeite. Titanaugite phenocrysts to 3 mm are usually twinned and fractured, some with faint concentric zoning. Central and outermost zones sometimes include ≤10 μm Fe-Ti oxide and other inclusions. A single corroded, twinned plagioclase microphenocryst, with a composition of An_{60} (as determined by the angle between extinctions) was observed.

Late basanite, Tepb2

This unit is also fine grained to microporphyritic and holocrystalline (Table 1). Weak shape-preferred crystal orientation, interpreted to be due to flow, is visible in a thin section (8C1 in Appendix B) taken from the lower Tepb2 outcrop at Tejana Mesa. Euhedral to subhedral titanaugite (estimated at 56-78% of total phases) dominates the groundmass. Opaque inclusions are common in these groundmass augites. Exsolved Fe-Ti oxide grains with embayed margins altered to limonite constitute ~0 to 16% of the total rock. Interstitial phases include alkali feldspar, nepheline, biotite, sericite, analcime,

and clay. The last three are interpreted to be hydrothermal alteration products.

Anhedral to subhedral fractured olivine (≤12%) is usually the dominant phenocrystic phase; but within a few centimeters of vein-wall rock interfaces exsolved Fe-Ti oxide grains occasionally take this role. Most olivine phenocrysts exhibit considerable alteration, with complete replacement by alteration products (dominantly iddingsite, chlorophaeite and Fe-Ti oxides) in some crystals.

Titanaugite phenocrysts range in size up to 2 mm. Grains are fractured; and many have undergone alteration to Fe-Ti oxides, clay, and limonite. Some larger grains have Fe-Ti oxide and silicate inclusions that appear to be original, as opposed to alteration, phases.

Veins, Tepv

The veins (Tepv) are holocrystalline and finely to coarsely porphyritic (Table 1). The dominant groundmass phase is alkali feldspar (estimated at 20 to 40% of total phases). Grains range from fan-spherulitic to skeletal, similar to quench textures observed by Lofgren (1980); a few are tabular. Intergranular relationships suggest up to three episodes of nucleation and growth of groundmass feldspars. Some feldspar microphenocrysts are found as inclusions in titanaugite phenocrysts. Occasional anhedral anorthoclase grains, a few hundred micrometers in length, are found in veins. These

consistently exhibit rounded, resorbed margins, interpreted to be the result of disequilibrium with the surrounding magma.

Many groundmass titanaugites appear to have nucleated on wall rock minerals, having habits similar to phenocrysts still attached to wall rock. A sparse groundmass clinopyroxene species is distinctly green. These grains are interstitial to other groundmass phases, in particular feldspar. Their interstitial relationship and relatively high Fe content (see below) support the conclusion that they resulted from very late stage renewal of pyroxene saturation in the cooling vein melt (Dunbar *et al.*, 1995).

Groundmass Fe-Ti oxides appear as isolated euhedral crystals and as acicular to vermicular grains along vein margins, often heterogeneously nucleated (Lofgren, 1983) on wall rock phases and surrounded by masses of sericite and analcime. Some other microphenocrysts appear to have heterogeneously nucleated on titanaugite crystals.

Numerous other phases occur in the groundmass. Euhedral, acicular apatite grains (≤3%) are included in most other phases; most apatites extend through the margins of including grains. Nepheline tends to be tabular. Analcime and sericite are interstitial phases, most concentrated near vein margins and filling cracks along vein-wall rock contacts, where they occasionally become the dominant phase. Masses of phosphorous-rich minerals (apatite?) are sometimes observed filling micrometer-scale cracks within veins.

Occasionally, calcite fills cracks that cut across veins and host rock. Zeolite masses, a few millimeters across, are found throughout veins.

Millimeter to centimeter scale titanaugite phenocrysts (19 to 35% of total phases) exhibit two distinct nucleation and growth habits. Grains observed in the interiors of veins (Fig. 5) tend to be subequant, and comparatively large: occasionally a centimeter or so long. Their number density is $<10^{-5}$ that of pyroxenes found in Tepb1 and Tepb2. They are euhedral to subhedral, exhibit sector and concentric zoning (Leung, 1974), and often poikilitically enclose Fe-Ti oxide (Fig. 7) and alkali feldspar grains. Thin section observations suggest that some of the enclosed grains may have served as nucleation points for the enclosing pyroxene. Occasionally, highly altered acicular, radiating augite(?) grains ≥5 cm long are observed in veins, most commonly on the west side of the upper one-third of El Porticito. These are similar in habit to large augites found near the top of the pegmatitic syenite of the Shonkin Sag laccolith (Barksdale, 1937, Fig. 9; Hurlbut & Griggs, 1939, Pl. 5, Fig. 2). Also similar to Shonkin Sag laccolith morphologies (Barksdale, 1952, Plates 1 & 3) are rare intergrowths of titanaugites and groundmass phases. Abundant smaller, wedge-shaped titanaugites compose the second morphology and appear to have nucleated on, and usually remain attached to, wall rock phases (Fig. 5).

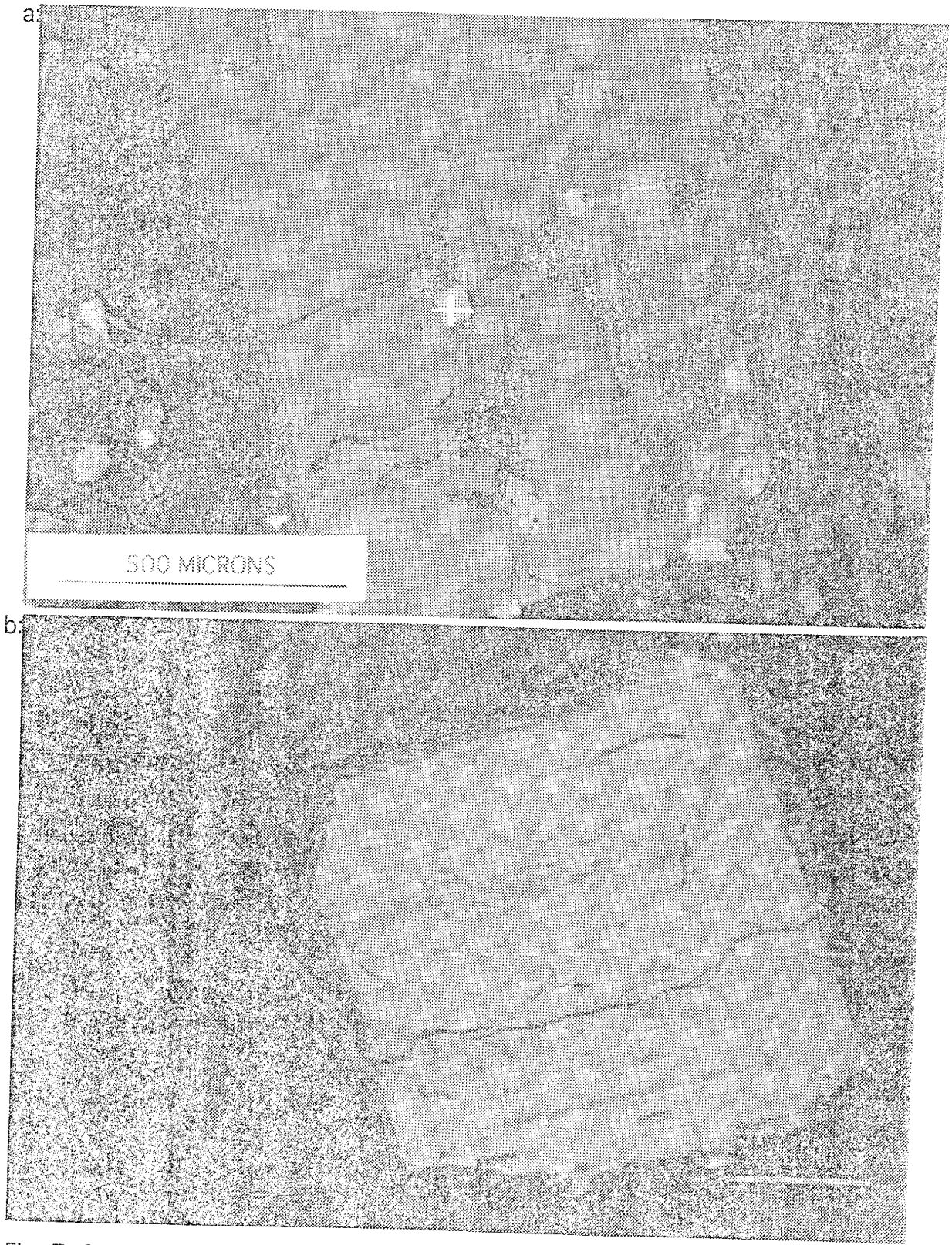

Fig. 7: Scanning electron micrograph of Fe-Ti oxide grain enclosed in titanaugite. a: Enclosing vein phenocryst. b: Microphenocryst exhibiting exsolution lamellae typical of all Fe-Ti oxide grains found in the study area.

Many titanaugite phenocrysts of both morphologies have abundant euhedral to subhedral exsolved Fe-Ti oxide microphenocrysts arranged necklace-like around their margins. Some titanaugites continued to grow around and a few micrometers beyond the microphenocrysts.

Iron-titanium oxide phenocrysts (5 to 15%) also range upward in size to nearly a centimeter. These occur as euhedral and hopper-texture grains. All are fractured. Pyroxene, feldspar, and apatite all appear as inclusions. Analcime usually fills voids within hopper-texture Fe-Ti oxide grains.

Anorthoclase also occurs as phenocrysts up to 3 mm. The rounded, embayed habit suggests disequilibrium with adjacent phases. These grains are interpreted to be xenocrystic, having crystallized at an early stage, while the magma was still at some depth and before final emplacement.

Veinlets in Tepb2 are seen in thin section to be concentrations of colorless Tepb2 and Tepv interstitial phases, primarily alkali feldspar and analcime, with minor nepheline and considerable apatite. Veinlets also contain sparse augite grains identical to those found in the Tepb2 groundmass. Feldspar concentration tends to increase, and analcime and apatite decrease, with distance into wall rock.

Mineral Chemistry

Olivines

Olivine crystals in Tp bombs show normal zoning, from Fo_{89} cores to Fo_{85} rims (Fig. 8). CaO content (which is near the detection limit in xenocryst and most microphenocryst cores) generally increases from cores to rims (Fig. 9), consistent with falling pressure and concurrent growth during eruption (Stormer, 1973; Köhler & Brey, 1990). MnO content is relatively constant, suggesting no change in the activity of Si (Watson, 1977) in the melt. The constant MnO content also suggests that crystal growth occurred below ~1050 °C, where the mineral-melt Mn partition coefficient might be expected to be relatively constant (Takahashi, 1978).

Olivine phenocrysts in Tepb1 basanite are normally zoned from ~Fo_{83} in cores to Fo_{78} in rims. Groundmass olivine is as low as Fo_{76} (Fig. 8). A 2 mm anhedral olivine grain is ~Fo_{90} to within ~75 μm of the rim, where composition drops to Fo_{80} (Fig. 8; in Fig 9, this grain is labeled "Tepb1 xenocryst"). The CaO content of the xenocryst remains ≤0.05% to within ~40 μm of the margin, then increases abruptly by about an order of magnitude, suggesting that the core grew under considerably higher pressure conditions than the rim (Köhler & Brey, 1990). A 250 μm microphenocryst (labeled "Tepb1 phenocryst" in Fig. 9), with forsterite content ranging from Fo_{83} to Fo_{78}, has a more CaO-rich core, but the CaO concentration in its rim is similar to that of the xenocryst and groundmass

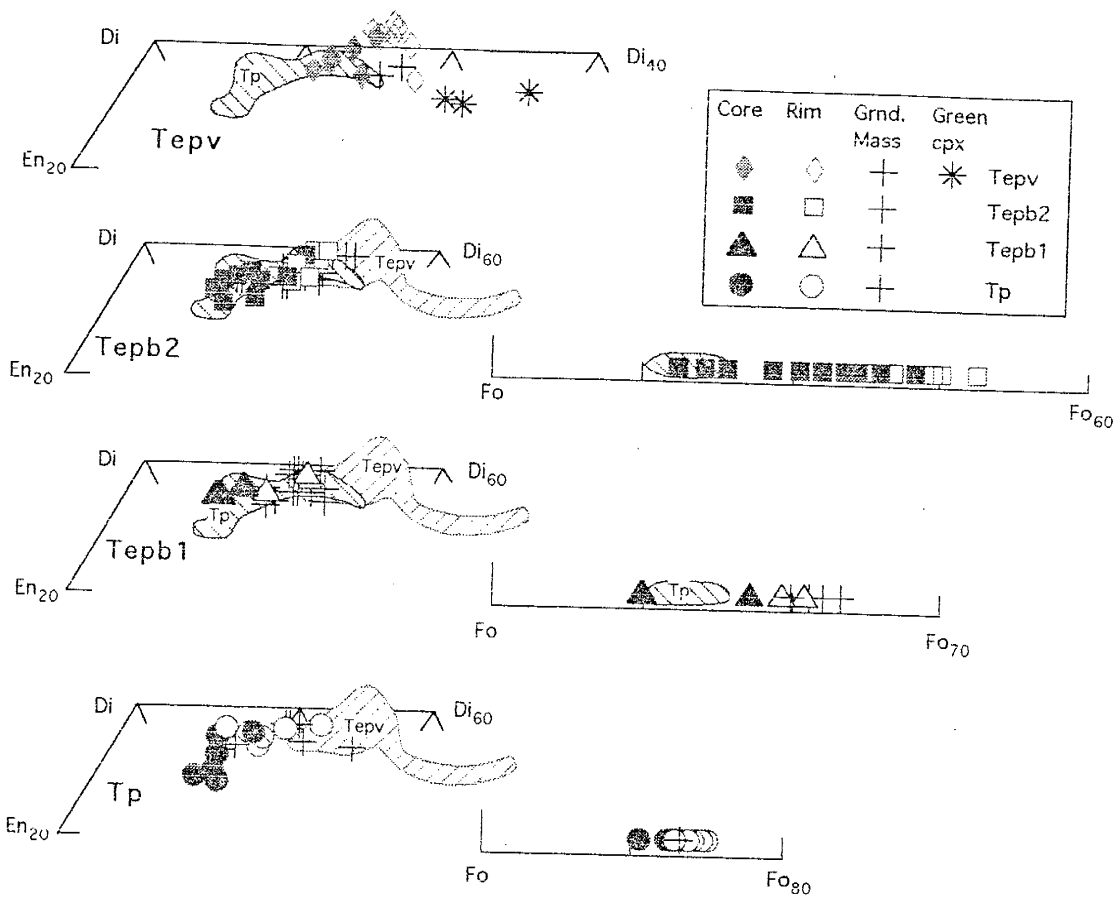

Fig. 8: Pyroxene and olivine compositions in order of magma eruption, from bottom to top. Olivine is absent from veins, and green, iron-rich clinopyroxene appears only in the groundmass of veins. Pyroxene end member concentrations were calculated according to the method of Klein and Hurlbut (1993), with iron partitioned by the method of Baldridge (1979). Ca, Mg, Fe, and Mn were not normalized to 1 prior to calculation of end members. This resulted in analyses plotting above the Di-Hd join (Morimoto, 1988). Olivine end member concentrations were calculated according to the method of Klein and Hurlbut (1993).

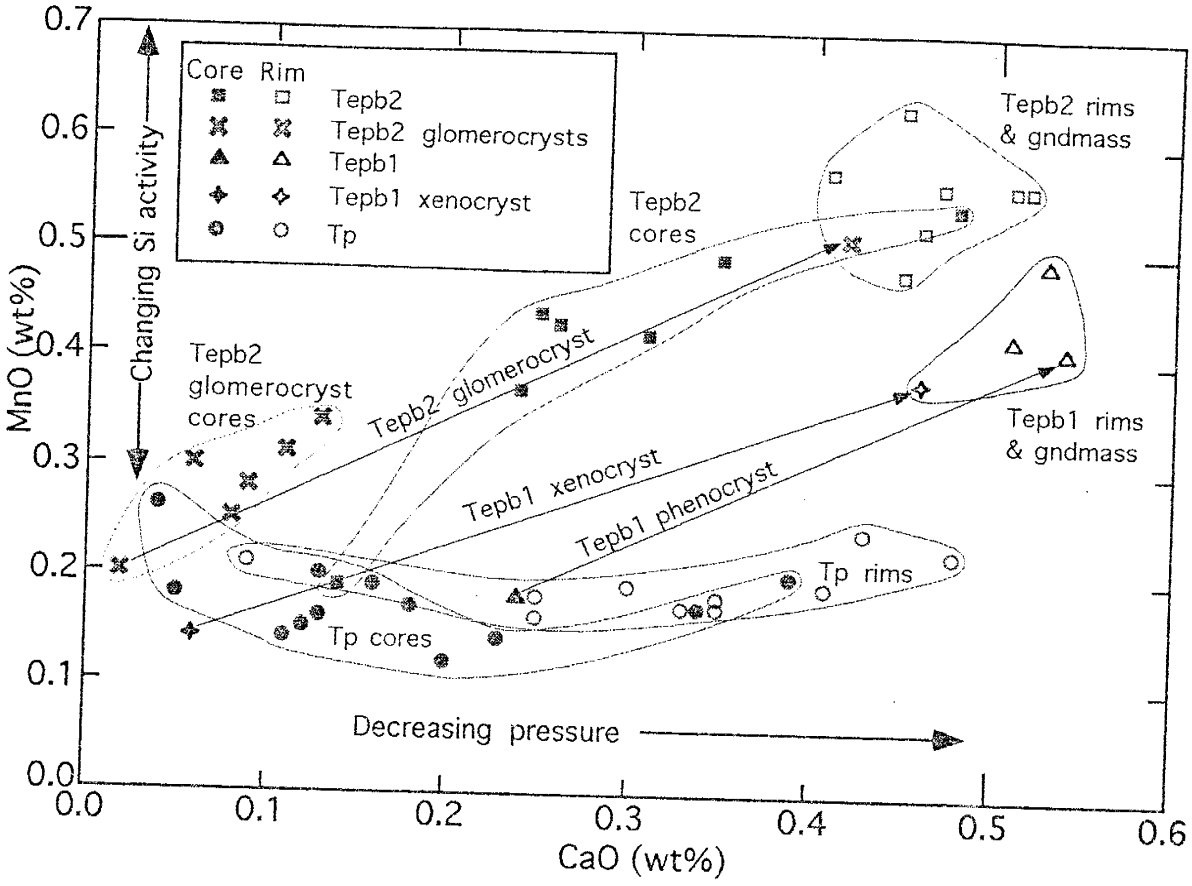

Fig. 9: MnO *vs.* CaO concentrations in olivines, illustrating the effects of changing Si activity in the melt and decreasing pressure. The effect of decreasing pressure during crystallization is evident in all units. The Tepb2 glomerocryst is interpreted to be xenocrystic, with crystallization conditions of the crystal cores similar to those of the Tepb1 xenocryst and some Tp phenocryst cores. Crystal rims generally experienced similar (surface) pressure, but magma chemistries differed among the units.

grains. The xenocryst core is interpreted as having grown at considerable depth; the phenocryst core in a shallow magma chamber; and the olivine rims and groundmass grains during (Marsh *et al.*, 1991) or after eruption of Tepb1 magma.

Tepb2 olivine phenocrysts range from cores of ~Fo_{78} to rims of Fo_{68} (Fig. 8). Individual crystals of a 0.5 cm diameter olivine glomerocryst have core compositions of ~$Fo_{85.5}$ to within ~40 μm of their margins, where forsterite concentration drops to ~Fo_{73}. Thus, the forsterite concentration in cores of these grains is intermediate between those of the xenocryst and phenocryst of Tepb1. Cores of individual crystals in the glomerocryst have CaO concentrations similar to the Tepb1 xenocryst core (Fig. 9). This glomerocryst is also interpreted as being xenocrystic, with the crystal cores having grown at considerable depth.

Although Tepb1 and Tepb2 olivine phenocryst cores and rims have similar CaO concentrations, MnO concentrations are higher in Tepb2 rims and groundmass grains, suggesting different Si (Watson, 1977) activity in the melt during narrow rim growth. (However, the SiO_2 whole rock concentrations are similar in Tepb1 and Tepb2, see below.)

Pyroxenes

All pyroxenes in the study area are clinopyroxenes (Appendix A). Pyroxenes become progressively more Fe-rich from Tp to Tepv, and from cores

to rims within each unit (Fig. 8). Some Tepv phenocrysts exhibit slight oscillatory zoning. Phenocryst rims and groundmass grains have similar compositions. The overall compositional trend is subparallel to the Di-Hd join (Fig. 8), similar to the Japanese alkaline basalt series (Aoki, 1964) and the main syenite of the Shonkin Sag laccolith (Nash and Wilkinson, 1970). Tp augite compositions are similar to those found in the lower chilled margin pseudoleucite shonkinites of the Shonkin Sag laccolith (Nash & Wilkinson, 1970), but with about twice the TiO_2; and exhibit a trend subparallel to the En-Di join, similar to high-Mg clinopyroxenes in basanites of the Hut Point Peninsula on Ross Island, Antarctica (Kyle, 1981).

Green interstitial clinopyroxenes in Tepv (Fig. 8) have Na_2O concentrations of ~1%, typical of augites (Deer *et al.*, 1992). These clinopyroxenes contain less Fe and Na and more Ca than most green groundmass pyroxenes found in the Shonkin Sag shonkinites (Nash and Wilkinson, 1970). Nevertheless, the Na_2O content is higher than in other pyroxenes in the study area, and along with the Fe, contributes to the green color.

Except in the green groundmass augites, the concentration of Al_2O_3 is ≥2 wt% in pyroxenes. The low Si activity of the undersaturated basanitic melt (see below) probably necessitated substitution of Al for Si (Carmichael *et al.*, 1970) to allow augite growth.

Aluminum and Ti concentrations increase from augite cores to rims and from Tp to Tepv (Fig. 10a), consistent with decreasing Si activity. The slope of the Al *vs.* Si curve in Fig. 10a is very nearly -1, consistent with coupled substitution of the form $Ti_y^{4+} + 2Al_z^{3+} \Rightarrow M_y^{2+} + 2Si_z^{4+}$ (where subscripts refer to clinopyroxene lattice sites and M refers to divalent cations) (Gibb, 1973). Ideally, this substitution would also result in a slope of -0.5 for Ti, but it is in fact about -0.4 (Fig. 10a), suggesting that Ti activity was insufficient to satisfy all the demands of the coupled substitution.

The ratio Ti/Al is plotted versus Mg, chosen to represent the degree of evolution of the melt (Stephenson, 1972), in Fig. 10b. There is overlap among pyroxene cores of the various lithologies, and rims and groundmass grains exhibit even more overlap. In Tepv phenocrysts Ti/Al ratios tend to increase from cores to high-Ti intermediate zones and then to decrease sharply toward grain boundaries. This pattern is consistent with the following interpretation.

While pyroxenes grew, Si activity continued to drop, and the activity of Fe increased in the immediate vicinity of growing Mg-rich pyroxene crystals. With sufficient Fe present, Fe oxide crystals nucleated and grew on pyroxene margins, incorporating Ti and reducing the Ti activity in the melt. Oxygen fugacity, fO_2, may have risen slightly during pyroxene growth, as indicated by the small increase in Na concentration from cores to rims (Kyle, 1981), causing Fe-Ti oxide compositions to become more Ti-rich (Carmichael *et al.*, 1974), and

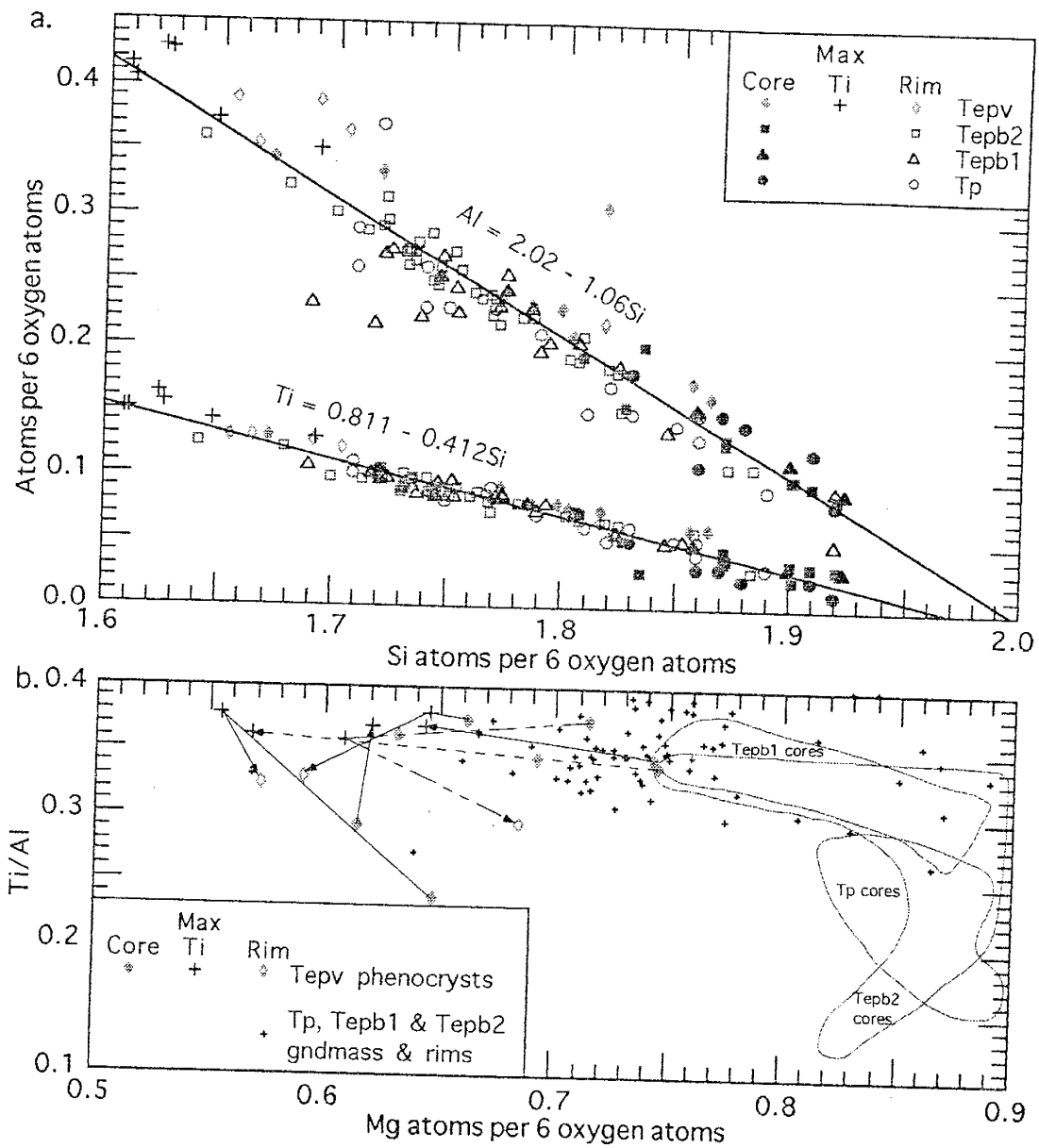

Fig. 10: Al and Ti *vs.* Si and Mg. a: Al slope suggests coupled substitution of Al and Ti for Si, but Ti slope (0.4) is lower than expected (0.5). This may indicate that Ti^{4+} activity in the melt was insufficient to provide all the atoms needed for charge balancing, requiring other elements also to perform this function. b: Vein phenocrysts exhibit increasing Ti/Al and decreasing Mg about 100 um from margins, where Fe-Ti oxide grains become common. From this zone to phenocryst margins, Ti/Al drops rapidly and Mg increases, suggesting that the Fe-Ti oxide grains locally depleted the melt of these elements and inhibited further phenocryst growth.

further depleting the melt of Ti. This resulted in phenocryst margins with sharply reduced Ti/Al ratios (and sometimes increased Mg concentrations). Thereafter, titanaugite growth soon ceased. With further cooling, other silicate phases, primarily alkali feldspar, grew forming the Tepv groundmass. Finally the melt again became supersaturated in Mg, allowing interstitial green augites to grow, and consuming the remaining Mg, Fe^{3+}, and Na.

Feldspars

Feldspars become more common, their compositions more varied, and Ca content tends to increase, from Tepb1 to Tepv (Fig. 11). Within Tepv, feldspar compositions range from $An_{12}Ab_{63}Or_{22}Cs_3$ (anorthoclase microphenocrysts) to $An_{1.5}Ab_{13}Or_{85}Cs_{0.5}$ (groundmass sanidine). This trend toward increasing Or content from microphenocrysts to groundmass grains is consistent with trends observed by Keil *et al.* (1972) in Hawaiian basaltic rocks. Anorthoclase grains in Tepv are Ba- and Sr-rich, as are sanidine grains located within a few millimeters of some healed cracks. Other groundmass feldspar grains, as well as inclusions in titanaugite, tend to be Ba- and Sr-poor.

Fe-Ti oxides

The exsolution of Fe- and Ti-rich lamellae in most Fe-Ti oxide grains large enough to be analyzed by electron microprobe precluded accurate analyses of

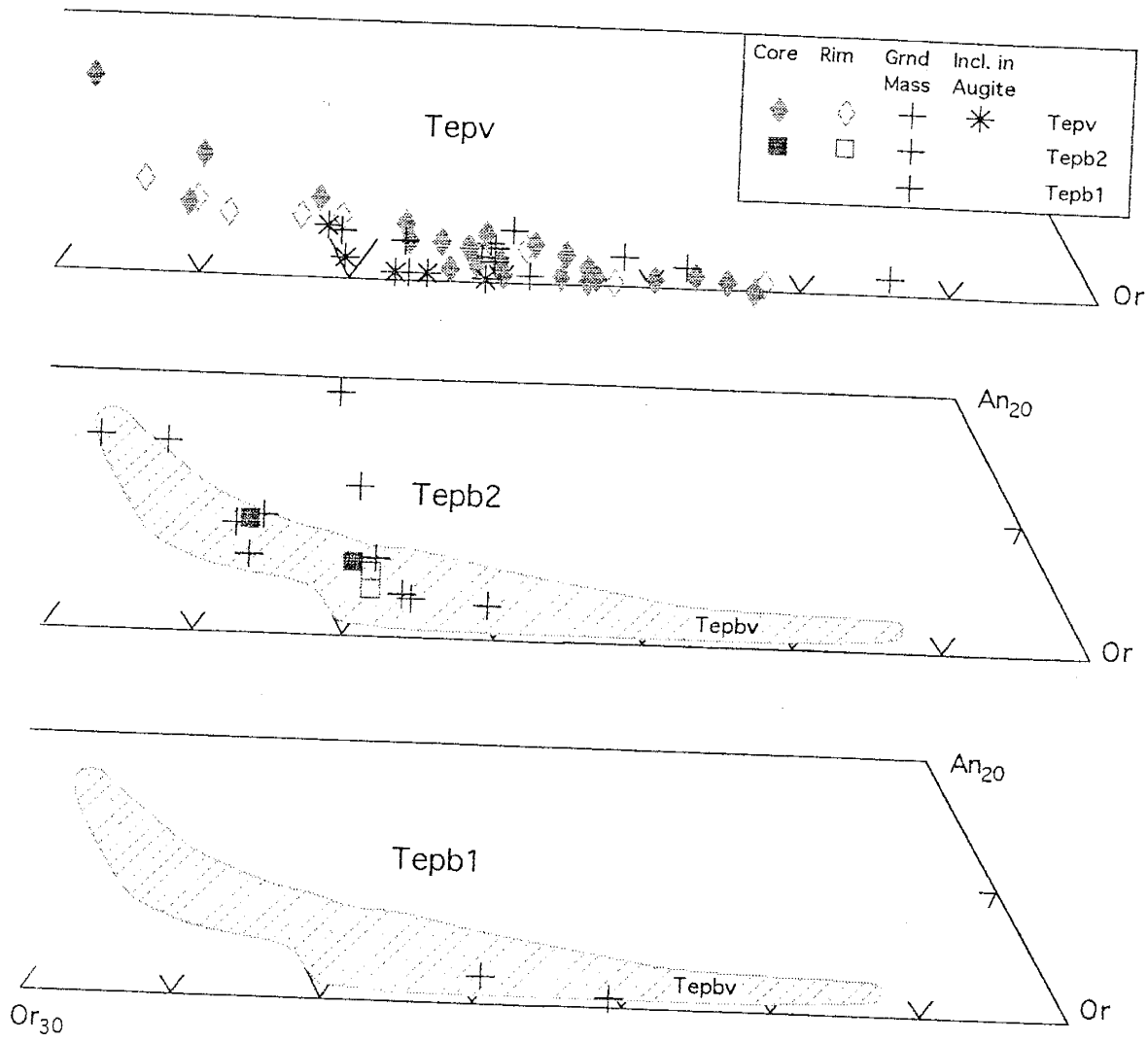

Fig. 11: Feldspar compositions in order of magma eruption from bottom to top. Feldspar is absent in Tp, and appears only as a rare interstitial phase in Tepb1. The most Ab-rich microphenocrysts in Tepv exhibit the cross-hatched twinning typical of anorthoclase (Deer *et al.*, 1992). End member compositions were calculated by the method of Klein and Hurlbut (1993).

this phase. The compositions listed in Appendix A must therefore be viewed with caution. Nevertheless, end member concentrations have been calculated using the method of Stormer (1983). Fe^{2+}-Fe^{3+} partitionings of iron for both the ilmenite-hematite and ulvöspinel-magnetite solid solution series were calculated, with the objective of determining to which series a grain belonged. Calculations for 13 of the 33 analyses resulted in ambiguous results, with mathematically reasonable partitioning of iron for both solid solution series. Only one grain, a low Ti magnetite, provided multiple, unambiguous results; but the total oxide concentration was low, casting doubt on the quality of the analyses.

No correlation between V_2O_3 and Fe or Ti oxides is evident (Appendix A), although V_2O_3 concentrations were near the detection limit (~0.1%) and were therefore subject to poor precisions.

Whole Rock Geochemistry

The major element compositions of rocks found at El Porticito and Tejana Mesa progressively changed during the eruptive sequence. Compositions became more evolved, beginning with the picrobasalts and foidites of Tp and ending with the tephrites and phonotephrites of Tepv (Fig. 12) (LeMaitre, 1989). The analyzed pyroclastic samples, Tp, have lower SiO_2, K_2O, and $Fe_2O_3^t$ (total iron expressed as ferric oxide) than the later lavas,

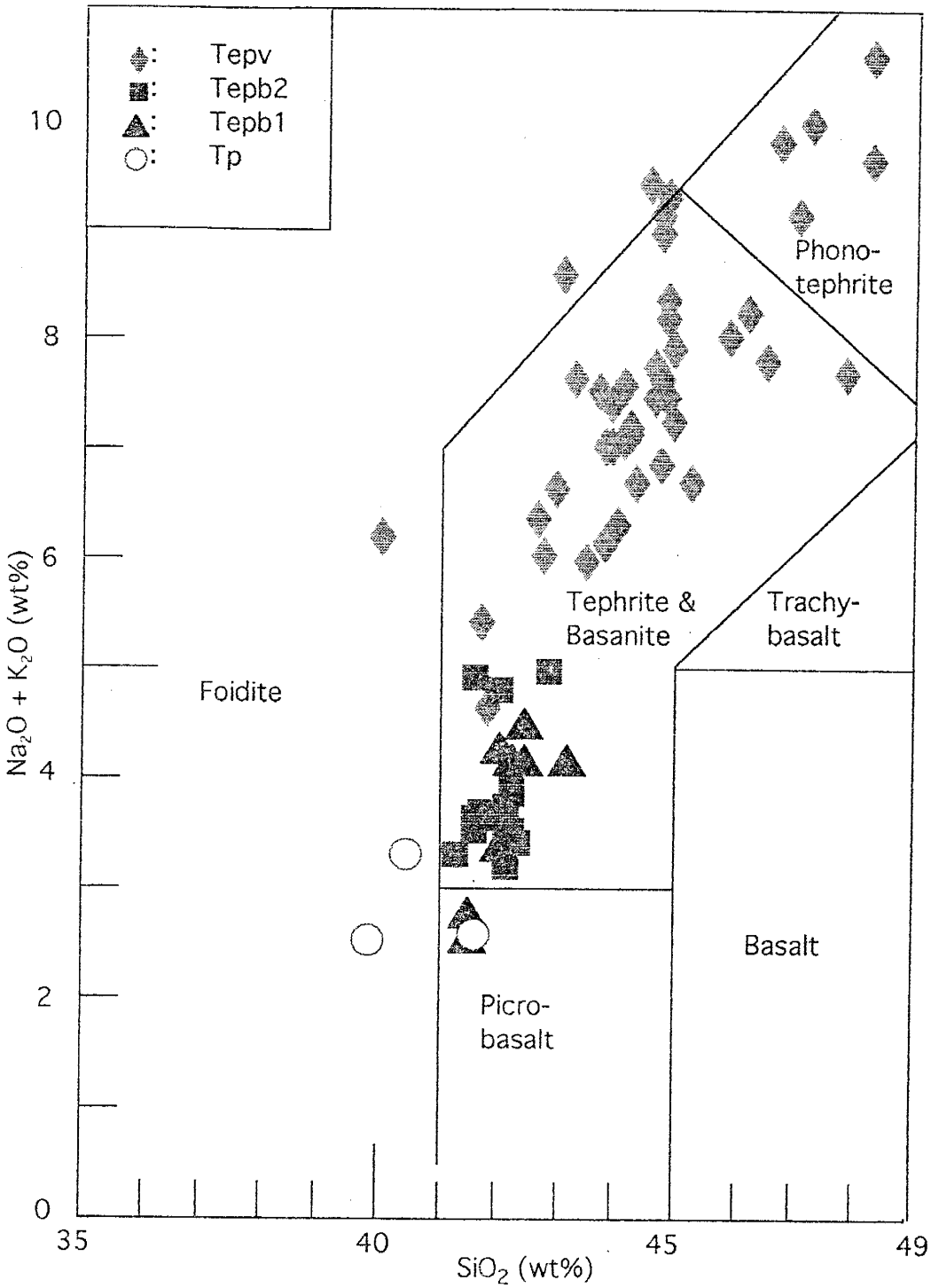

Fig. 12: Total alkalis *vs.* SiO_2 of samples from El Porticito and Tejana Mesa. Rock compositions followed a trend, ranging from picrobasalt to phonotephrite, as the eruptive sequence progressed. Classification from LeMaitre (1989).

Tepb1 and Tepb2 (Fig. 13). In terms of MgO, the two Tp samples from the southeast corner of Tejana Mesa (27C and 27D in Appendix C) are similar to the more mafic basanite, Tepb1; whereas the sample from the southwest corner of Tejana Mesa (49E in Appendix C) is more similar to Tepb2.

The compositions of lavas Tepb1 and Tepb2 overlap in SiO_2, alkalis, and $Fe_2O_3^t$ concentrations, but differ in MgO and Al_2O_3 (Figs. 12 & 13). The first of the lavas, Tepb1, is a basanite; but the lower MgO concentration in Tepb2 causes it to vary from tephrite (ol < 10%) to basanite (ol > 10%) (LeMaitre, 1989). Tepb2 is here referred to as basanite. The higher Al_2O_3 content in Tepb2 corresponds to its more abundant aluminum-rich interstitial and veinlet silicate phases, and suggests that it is more chemically evolved than Tepb1. The higher TiO_2 concentration in Tepb2 is reflected in its higher Fe-Ti oxide abundance; and the appearance of modal apatite corresponds to an increase in P_2O_5. Lavas exhibit considerable variability in Na_2O, and to a lesser extent K_2O, concentrations (Appendix C). Both oxides have weak negative correlations with CaO concentration, and are not correlated with sample location (Plate 1). The concentrations of Na_2O, but not K_2O, in each of the lavas exhibit weak negative correlations with LOI. The cause of the variability in alkali content is unknown.

The most magnesian vein samples, Tepv, tend to lie on major element compositional trends defined by Tepb1 and Tepb2. P_2O_5 and K_2O are notable exceptions (Fig. 13). The most magnesian veins have about twice as much K_2O

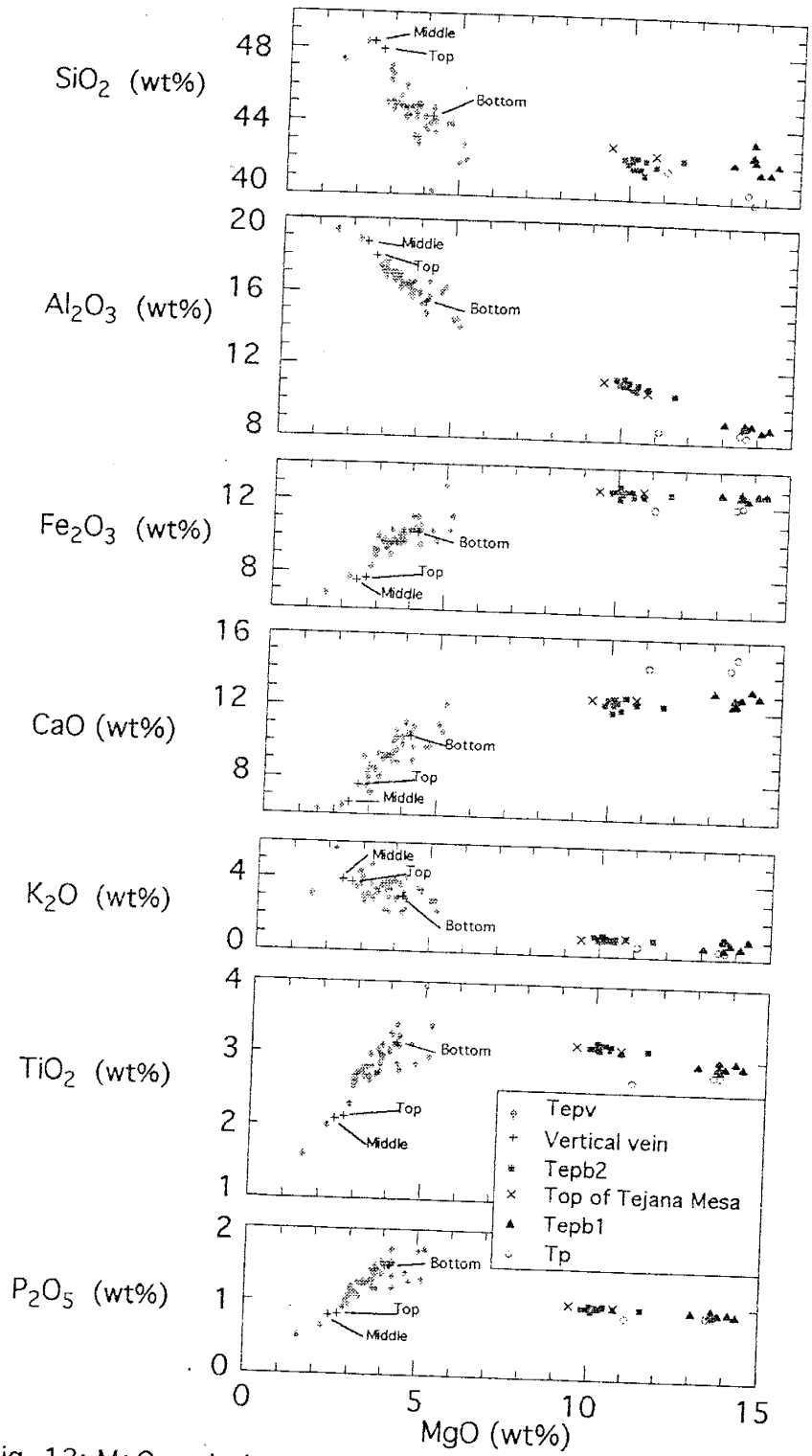

Fig. 13: MgO variation diagrams for major element oxides. Note the ×'s denoting Tepb2 samples recovered from near the top of the southeast and southwest corners of Tejana Mesa above Ttmb in Fig. 1 and the +'s denoting three samples taken ~2 m apart along a subvertical vein at El Porticito.

as that which might be expected from an extrapolation of lava compositions (~1%), and the range of P_2O_5 concentrations spans the extrapolated value of ~1%.

Although major element concentrations within veins are characterized by linear trends when plotted against MgO, it is significant that vein compositions do not vary systematically with the height at which samples were collected at El Porticito; and that vein compositions at El Porticito and Tejana Mesa have the same ranges. Three samples were taken from ~2 m intervals along a single El Porticito subvertical vein. Although one might assume that the flow was unidirectional along the vein, the compositional trends are not (plus symbols in Fig. 13). This is also true on the larger scale. Tepv samples taken from the bottom and top of El Porticito, and at Tejana Mesa, exhibit randomly varying compositions with elevation. As expected, compositions do, however, correspond well with the mafic phenocryst concentrations.

Among the compatible trace elements, Cr and Ni concentrations in all tephra, Tp, samples are similar to those found in Tepb1 (Fig. 14). Cr and Ni concentrations drop sharply with decreasing MgO in Tepb1 and Tepb2 and continue to decrease with decreasing MgO concentration in veins. In contrast, V content increases from Tepb1 through Tepb2 to the most mafic vein samples. Thereafter, V content drops with falling MgO concentration, similar to Ti and Fe (Fig. 13).

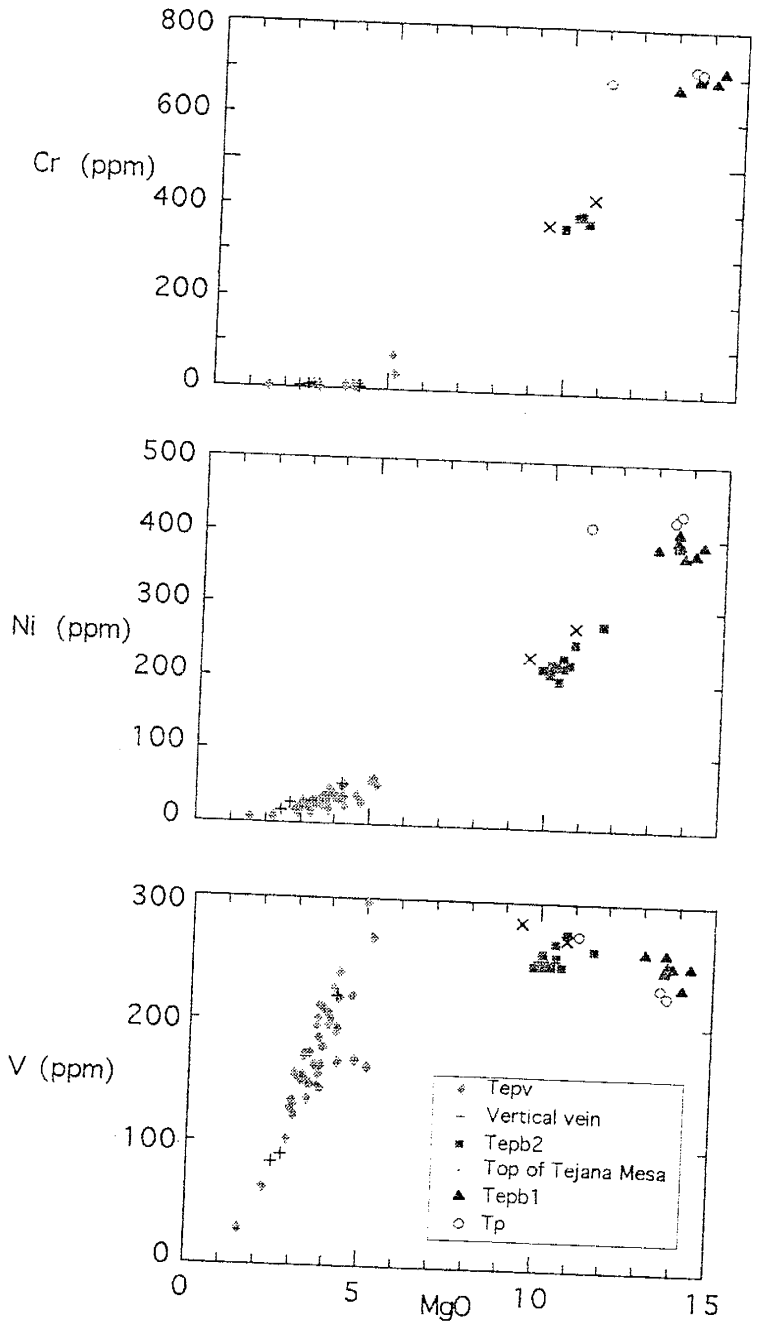

Fig. 14: Whole rock compatible trace element concentrations. Chrome and Ni behave compatibly from Tepb1 to the most mafic Tepv sample. The apparently incompatible behavior of V may be due to post-emplacement alteration of veins.

Pyroclastic, Tp, and lava, Tepb1 and Tepb2, samples have similar incompatible element patterns, with all elements except Cs being slightly more concentrated in lavas than in bombs (Fig. 15). Veins tend to contain two to three times higher concentrations of incompatible elements than lavas. All samples are strongly depleted in Rb and K, in sharp contrast to concentrations of these elements in alkali basalts of the Zuni-Bandera volcanic field, New Mexico (Menzies *et al.*, 1991).

The chondrite-normalized REE patterns (Fig. 16) decrease steeply from La to Lu, and contain no Eu anomalies. These features are similar to those found in the Geronimo volcanic field, Arizona (Menzies *et al.*, 1985). REE fractionation in early magmas is more extreme than for typical ocean island basalt (OIB), with La_N/Lu_N more than a factor of two greater than for typical OIB. LREE/HREE fractionation increases still further in veins.

Fire assay analyses (Bugbee, 1940) were conducted on selected samples to determine Au and Ag content (L. A. Brandvold, personal communication, 1996). Multiple specimens of Tepv were analyzed (Appendix C); neither of the precious metals was detected.

Neodymium isotopic data were acquired at the Academy of Finland, Helsinki (O. T. Ramo, personal communication, 1997). These data are included in Appendix C. The analyzed samples, one each from Tepb1 and Tepb2, have $^{143}Nd/^{144}Nd$ ratios that are identical within error: 0.512802, within the range of

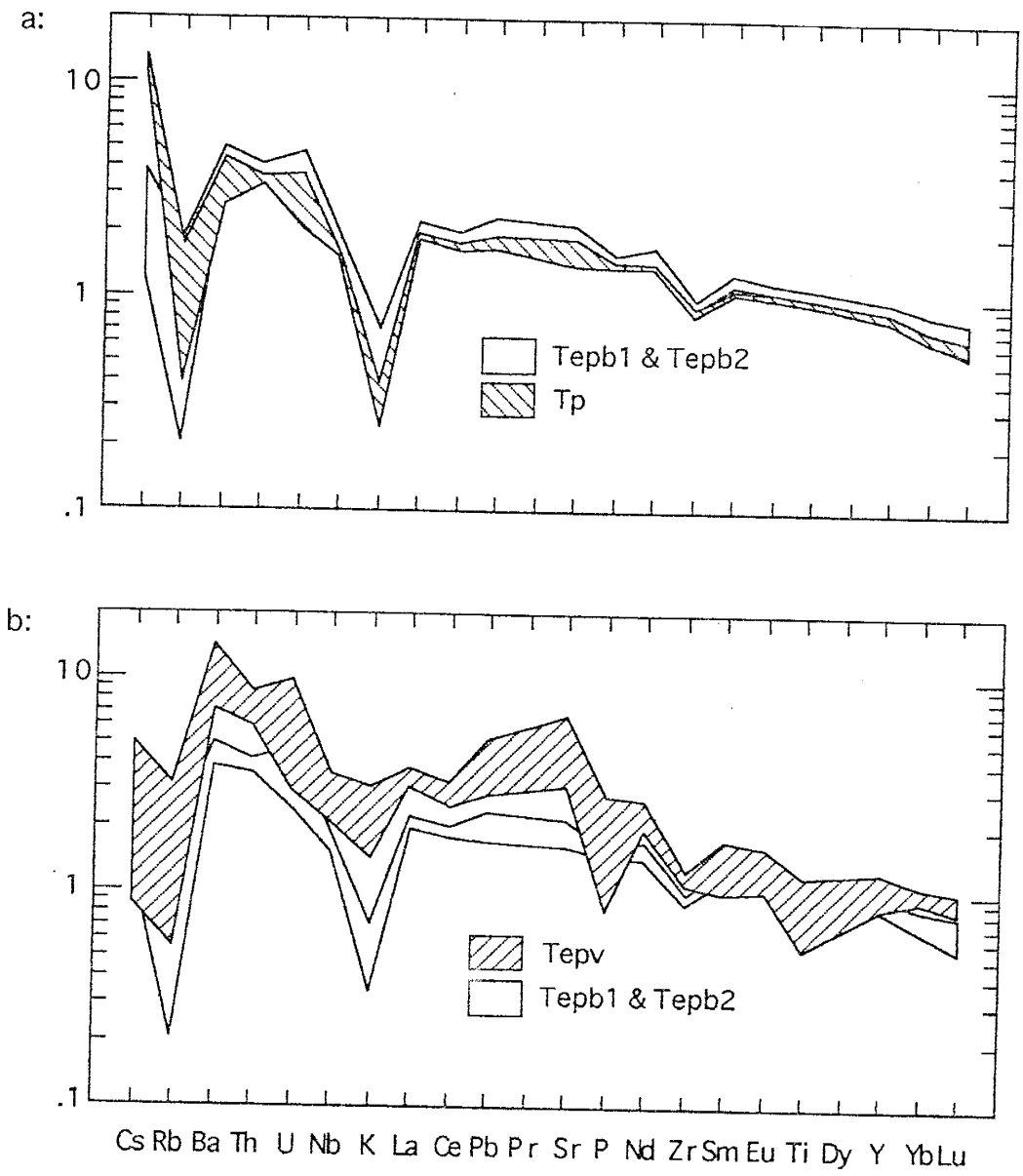

Fig. 15: Incompatible trace element concentrations normalized to ocean island basalts (OIB) (Sun & McDonough, 1989). a: Bombs (Tp) and lavas. Trace element concentrations in Tepb1 and Tepb2 overlap, and so have been grouped together. Note high concentration of Cs in bombs and strong depletions of Rb and K in bombs and lavas. b: Veins (Tepv) and lavas.

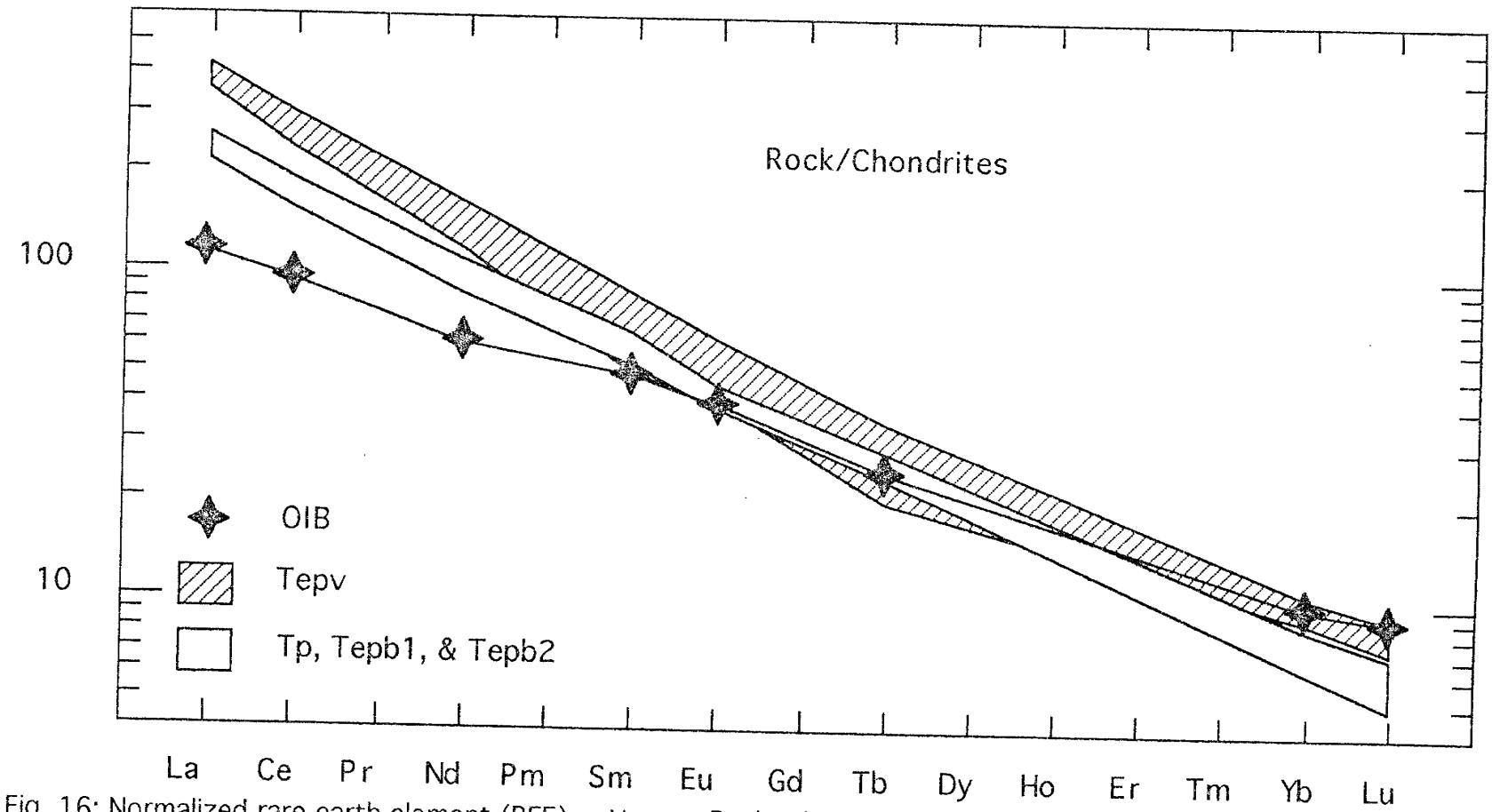

Fig. 16: Normalized rare earth element (REE) patterns. Rocks that preceded veins have overlapping patterns and have been grouped together. Note strong LREE/HREE fractionation, suggesting small degree partial melting of a mantle source, and absence of a Eu anomaly, suggesting the absence of plagioclase fractionation during magma genesis. (Normalization factors from Nakamura, 1974; OIB from Sun & McDonough, 1989.)

Zuni-Bandera lavas (Menzies *et al.*, 1991) and garnet lherzolite inclusions at The Thumb in the Navajo Volcanic Field (Roden *et al.*, 1990). The present day ε_{Nd} is +3.17, slightly below the range of Colorado Plateau-Basin and Range transition zone alkali basalts (≥ +3.3) (Perry *et al.* , 1987) and Zuni-Bandera Volcanic Field values (≥ 4.5) (Menzies *et al.*, 1991). Nd model ages (DePaolo, 1981) are 370 Ma for Tepb1 and 364 Ma for Tepb2.

Dating

Three whole rock $^{40}Ar/^{39}Ar$ ages have been obtained (W. C. McIntosh, personal communication, 1996): two on Tepb1 and one on Tepb2 (Fig. 1 and Table 2). The two Tepb1 ages (one isochron and one plateau) were obtained from samples taken from the SE corner of Tejana Mesa, above the pyroclastic deposit shown in Fig. 1; the single Tepb2 (isochron) age was measured on a sample taken from the N end of El Porticito, a few meters above the colluvium. The three ages obtained are, within error, identical, averaging 7.08 ± 0.25 Ma (2σ). In addition to these units, the age of a basanite dike that is aligned with the Mesa Tinaja fault ~500 m S of the study area was determined to be 7.08 ± 0.64 Ma (2σ) (Table 2).

Table 2: Summary of whole rock $^{40}Ar/^{39}Ar$ age determinations on basanite samples from El Porticito and adjacent Tejana Mesa

Sample	Location	Unit	Analysis	n	40/36	Err	Age	±2 sigma	Comments
28	Tejana Mesa	Tepb1	isochron	7	296.9	2.9	7.13	0.30	b-g steps
29	Tejana Mesa	Tepb1	step H	1			6.94	0.34	61.1% ^{39}Ar in H step
6B	El Porticito	Tepb2	isochron	9	300.4	1.2	7.17	0.70	all steps, low yields
mean age							7.08	0.25	
32	*	Dike	isochron	7	297.6	1.8	7.08	0.64	b-h steps

* This sample was taken from a basanite dike located ~500 m SSW of the study area.

$^{40}Ar/^{39}Ar$ dating (Dalrymple *et al.*, 1981, and McDougall & Harrison, 1988) of samples was performed at the New Mexico Geochronology Research Laboratory at NMT, using a MAP 215-50 mass spectrometer, operated in electron multiplier mode, to determine relative isotopic abundances.

DISCUSSION

Petrogenesis

The trends in whole rock composition evident in the data of Figs. 13 and 14 strongly suggest that vein magma evolved along a crystal fractionation trend, and that the most mafic vein samples evolved from Tepb2, which in turn evolved from Tepb1. However, geochemical modeling does not support this, but rather indicates a significantly different petrogenetic evolution.

Mass balance models

Veins: The major element data (Fig. 13) suggest that Tepv may have resulted from fractionation of Tepb2, either by removal of melt (Philpotts *et al.*, 1996) through veinlets now exposed in the study area, or fractional crystallization of Tepb2 magma in an underlying chamber. To investigate these possibilities, least squares mass balance numerical models (Bryan *et al.*, 1969) were used. Such calculations generate a model (or calculated) rock composition, equivalent to the parent fractionating magma, by adding minerals (with compositions found in Tepv and Tepb2 (Table 3)) to the assumed residual liquid (Appendix C). In these calculations, the differences between calculated and measured SiO_2 and Al_2O_3 concentrations were weighted <1 in order to reduce their strong effect on the models. Matches between measured rock compositions and those calculated for the parental magma were

Table 3: Representative Mineral Compositions

	Cpx (En_{46})	Cpx (En_{41})	Cpx (En_{39})	Cpx (En_{35})	Ol (Fo_{90})	Ol (Fo_{80})	Ol (Fo_{73})	Hem(Ilm_{45})	Mt (Usp_{58})	Hem(Ilm_{24})	Ne (Ne_{85})	Ne($Ne_{85.2}$)	Ksp (Or_{65})	Ana	Ap	Chab	Kaol
	19A1-29 Tepb1 pheno. core	19A1-109 Tepb1 gndmass.	1B-146 Tepb2 pheno. core	1B-142 Tepb2 pheno. rim	19A1-55 Tepb1 pheno. core	19A1-61 Tepb1 pheno. rim	6B-23 Tepb2 pheno. rim	21.1-36 Tp micropheno.	stoichiomet.	19A1-19 Tepb1 gndmass.	19A1-73 Tepb1 gndmass.	1B-111 Tepv gndmass.	15.1-24 Tepv gndmass.	15.1-40 Tepv gndmass.	6B-41 Tepv gndmass.	stoichiomet.	stoichiomet.
SiO_2	52.10	47.80	46.98	44.79	40.39	38.77	37.81	0.04	0.00	0.09	45.50	48.79	65.72	55.24	0.16	60.33	54.07
TiO_2	1.09	2.61	3.17	4.17	n.d.	n.d.	n.d.	22.85	21.00	15.85	n.a.	0.01	0.12	n.a.	n.a.	0.00	0.00
Al_2O_3	2.60	4.43	5.42	7.41	0.01	0.03	0.02	1.50	0.00	1.87	32.91	30.82	19.49	23.39	0.01	25.59	45.93
FeO	4.05	7.02	7.09	8.28	9.48	18.11	23.31	67.10	79.00	70.21	0.83	0.38	0.21	0.24	0.19	0.00	0.00
MnO	0.07	0.10	0.18	0.19	0.14	0.39	0.51	0.82	0.00	0.59	n.a.	n.a.	n.a.	n.a.	n.a.	0.00	0.00
MgO	16.03	13.88	12.70	11.02	49.78	42.69	37.75	0.65	0.00	3.66	n.a.	n.a.	n.a.	n.a.	0.15	0.00	0.00
CaO	23.18	22.51	22.54	22.19	0.06	0.45	0.42	n.d.	0.00	0.06	0.26	1.17	0.06	0.11	54.53	14.08	0.00
Na_2O	0.39	0.56	0.50	0.69	n.a.	n.a.	n.a.	n.a.	0.00	n.a.	16.86	16.01	4.05	11.22	n.d.	0.00	0.00
K_2O	n.a.	n.a.	n.a.	n.a.	n.a.	n.a.	n.a.	n.a.	0.00	n.a.	4.05	2.26	11.38	0.15	0.01	0.00	0.00
P_2O_5	n.a.	n.a.	n.a.	n.a.	n.a.	n.a.	n.a.	n.a.	0.00	n.a.	n.d.	0.07	n.d.	n.d.	41.59	0.00	0.00
V	n.a.	n.a.	n.a.	n.a.	n.a.	n.a.	n.a.	1930.5		1896.5	n.a.	n.a.	n.a.	n.a.	n.a.		
Cr	6616.2	205.9	n.a.	41.1	225.8	27.4	164.2	150.5		11946.2	n.a.	n.a.	n.a.	n.a.	n.a.		
Ni	251.5	n.a.	683.6	141.4	4094.0	1524.4	1807.3	133.6		1383.0	n.a.	n.a.	n.a.	n.a.	n.a.		
Zn	n.a.	n.a.	n.a.	n.a.	369.6	n.a.	474.0	562.4		1542.6	n.a.	n.a.	n.a.	n.a.	n.a.		
Sr	n.a.	n.a.	101.5	46.5	n.a.	n.a.	n.a.	n.a.		n.a.	n.a.	n.a.	845.6	n.a.	n.a.		

Major element concentrations in wt%

Trace element concentrations in parts per million (ppm)

Mt (Usp_{19}), Chab, and Kaol compositions are stoichiometric models.

n.a.: not analyzed

n.d.: below detection limit

considered satisfactory when weighted least squared differences of major element oxides totaled less than 0.02. Table 4 gives the best model calculations for the most mafic Tepb2 rock (sample 44F) from the most mafic vein analysis (25B). This model suggests that the vein sample represents a 44.1% residual. The sum of squared weighted residuals is 0.187, with K_2O contributing the greatest residual. Table 5 lists the measured concentrations of selected trace elements in sample 44F and those calculated, assuming 44.1% melt removal, mineral-melt partition coefficients taken from the literature (Table 6), and Rayleigh fractionation. The agreement between measured and calculated compatible trace elements is especially poor. Clearly, Tepb2 magma is a poor candidate to be a parent of Tepv.

Similar calculations were conducted to determine if magma with the composition of Tepb1 might have been the parent of Tepv. The model is given in Tables 4 and 5. The sum of major element oxide squared weighted residuals is 0.010, consistent with magma of composition Tepb1 having been the parent of Tepv. Corresponding calculated concentrations of compatible elements Cr and Ni (but not V) also agree well with measured values, as do most incompatible elements. Similar favorable results were obtained for less mafic vein compositions. I conclude that magma with the composition of Tepb1 was the more likely parent for vein rock, and that no Tepb2 contribution is required.

Table 4: Least-squares mass balance solutions for El Porticito tephrites and basanites

	SiO_2	TiO_2	Al_2O_3	FeO	MnO	MgO	CaO	Na_2O	K_2O	P_2O_5	ΣR^2
Fractionation											
Tepb2→Tepv											
44F → 25B											
44F = 0.441 (25B) + 0.319 Cpx(En_{39}) + 0.119 Ol(Fo_{73}) + 0.032 Hem(Ilm_{45}) + 0.005 Ap + 0.086 Ne($Ne_{85.2}$)											
meas	43.82	3.32	11.43	12.20	0.19	11.08	13.46	2.58	0.87	1.05	
calc	43.79	3.42	11.11	12.17	0.23	11.10	13.47	2.70	1.24	1.04	0.187
weight	0.4	1.0	0.5	1.0	1.0	1.0	1.0	1.0	1.0	1.0	
Tepb1→Tepv											
19A → 25B											
19A = 0.316 (25B) + 0.381 Cpx(En_{41}) + 0.181 Ol(Fo_{80}) + 0.033 Hem(Ilm_{45}) + 0.008 Ap + 0.081 Ne(Ne_{85})											
meas	43.43	3.00	9.09	11.79	0.18	14.83	13.29	2.42	1.03	0.94	
calc	43.33	2.96	9.18	11.80	0.19	14.84	13.32	2.41	1.07	0.91	0.010
weight	0.4	1.0	0.5	1.0	1.0	1.0	1.0	1.0	1.0	1.0	
Tepb1→Tepb2											
19A → 44F											
19A = 0.631 (44F) + 0.189 Cpx(En_{46}) + 0.096 Ol(Fo_{90}) + 0.032 Hem(Ilm_{45}) + 0.007 Ap + 0.044 Ne(Ne_{85})											
meas	43.43	3.00	9.09	11.79	0.18	14.83	13.29	2.42	1.03	0.94	
calc	43.42	3.10	9.20	11.76	0.17	14.84	13.29	2.44	0.73	0.95	0.107
weight	0.4	1.0	0.5	1.0	1.0	1.0	1.0	1.0	1.0	1.0	
Modes											
45A (Top)											
45A = 0.236 Cpx(En_{35}) + 0.069 Hem(Ilm_{24}) + 0.327 Ksp(Or_{65}) +0.051 Ana + 0.020 Ap + 0.128 Ne($Ne_{85.2}$) + 0.102 Chab + 0.066 Kaol											
meas	51.11	2.26	19.15	7.36	0.14	2.90	8.04	4.17	3.99	0.88	
calc	51.11	2.22	19.15	7.37	0.09	2.91	8.04	4.17	3.99	0.88	0.004
weight	1.0	1.0	1.0	1.0	1.0	1.0	1.0	1.0	1.0	1.0	
45B (Middle)											
45B = 0.207 Cpx(En_{35}) + 0.069 Hem(Ilm_{24}) + 0.314 Ksp(Or_{65}) + 0.069 Ana + 0.019 Ap + 0.232 Ne($Ne_{85.2}$) + 0.064 Chab + 0.026 Kaol											
meas	50.66	2.19	19.54	7.10	0.14	2.56	6.91	5.99	4.08	0.83	
calc	50.66	2.09	19.54	7.12	0.08	2.58	6.91	5.99	4.08	0.83	0.014
weight	1.0	1.0	1.0	1.0	1.0	1.0	1.0	1.0	1.0	1.0	
45C (Bottom)											
45C = 0.385 Cpx(En_{35}) + 0.080 Mt(Usp_{58}) + 0.240 Ksp(Or_{65}) + 0.033 Ana + 0.035 Ap + 0.173 Ne($Ne_{85.2}$) + 0.053 Kaol											
meas	46.43	3.30	16.16	9.66	0.16	4.39	10.80	4.43	3.11	1.57	
calc	46.43	3.33	16.16	9.65	0.07	4.30	10.85	4.42	3.10	1.52	0.021
weight	1.0	1.0	1.0	1.0	1.0	1.0	1.0	1.0	1.0	1.0	

Table 5: Trace element concentrations for FC models calculated using published partition coefficients

	Tepb2 → Tepv 44F → 0.441(25B)			Tepb1 → Tepv 19A → 0.316(25B)			Tepb1 → Tepb2 19A → 0.631(44F)		
Element	meas 44F	calc 44F	F=0.441 bulk D	meas 19A	calc 19A	F=0.316 bulk D	meas 19A	calc 19A	F=0.631 bulk D
V	283	813	2.27	258	928	2.02	258	711	3.00
Cr	414	313	3.71	733	731	3.66	733	1354	3.57
Ni	246	186	2.47	404	407	2.72	404	541	2.71
Sc	22	19	1.89	25	25	1.85	25	31	1.77
Rb	24	23	0.13	17	17	0.12	17	16	0.12
Sr	1459	1417	0.42	1163	1143	0.40	1163	1120	0.43
Ba	1762	1705	0.31	1343	1336	0.30	1343	1286	0.32
Y	29	24	0.46	26	20	0.46	26	23	0.47
Zr	275	244	0.53	256	204	0.51	256	225	0.56
Nb	77	61	0.04	75	44	0.04	75	50	0.06
Th	16	17	0.24	14	13	0.24	14	11	0.25
Hf	7	5	0.53	6	4	0.51	6	6	0.56
Ta	5	5	0.35	4	4	0.34	4	4	0.35
La	88	90	0.40	77	75	0.42	77	68	0.44
Ce	168	173	0.45	148	146	0.46	148	133	0.49
Nd	69	69	0.46	59	59	0.47	59	54	0.50
Sm	14	13	0.60	12	12	0.61	12	12	0.62
Eu	4	4	0.66	3	3	0.66	3	3	0.66
Tb	1	1	0.50	1	1	0.50	1	1	0.58
Yb	2	2	0.69	2	2	0.69	2	2	0.73

bulk D calculated using mineral-melt partition coefficients listed in Table 6 and mineral proportions listed in Table 4.

Table 6: Published mineral/melt partition coefficients

	Olivine		Clinopyroxene		Fe-Ti oxides		K-feldspar		Apatite		Nepheline	
V	0.060	Ro	1.350	Ro	26.00	Ro						
Cr	1.000	Le	5.730	Le	4.21	Le						
Ni	5.640	Le	2.000	Ca	2.39	Ca						
Sc	0.200	Ca	3.100	Ca	1.39	Ca			0.41	Ca		
Rb	0.004	Le	0.100	Le	0.08	Le	0.320	La	0.56	Ca	0.440	La
Sr	0.020	Le	0.550	Le	0.90	Le	2.300	La	1.67	Ca	0.240	La
Cs	0.043	La	0.026	La			0.044	La			0.413	La
Ba	0.050	Le	0.400	Le	0.80	Le	3.409	La	0.95	Ca	0.090	La
Y	0.010	Ro	0.700	Ca	0.19	Ca	0.017	La	5.08	Ca	0.010	La
Zr	0.100	Le	0.700	Le	2.00	Le	0.003	La			0.005	La
Nb	0.014	La	0.029	La	0.40	Ro	0.004	La			0.011	La
Th	0.040	Le	0.350	Le	0.45	Le	0.007	La	0.95	Ca	0.014	La
Hf	0.050	Le	0.700	Le	2.00	Le	2.000	La	0.64	Ca	0.008	La
Ta	0.030	Le	0.500	Le	1.00	Le			0.09	Ca		
La	0.2000	Le	0.510	Le	0.40	Le	0.052	La	5.16	Ca	0.010	La
Ce	0.2600	Le	0.550	Le	0.30	Le	0.039	La	6.34	Ca	0.011	La
Nd	0.1800	Le*	0.600	Le*	0.25	Le*	0.026	La	6.60	Ca	0.013	La
Sm	0.1000	Le	0.900	Le	0.20	Le	0.028	La	6.30	Ca	0.012	La
Eu	0.1000	Le	1.000	Le	0.52	Le	1.261	La	3.77	Ca	0.043	La
Tb	0.1800	Le	0.570	Le	1.50	Le	0.020	La	5.79	Ca	0.014	La
Yb	0.3000	Le	0.900	Le	1.50	Ro	0.028	La	3.24	Ca	0.016	La
Lu	0.0454	Ro	0.506	Ro	1.40	Ro	0.020	La#	3.40	Ca	0.015	La#

Sources of partition coefficient data:
- Ca: Caroff *et al.* (1993)
- La: Larsen (1979)
- Le: Lemarchand *et al.* (1987)
- Ro: Rollinson (1993)
- *: Interpolated
- #: Extrapolated

Significant major element variations occur within the veins (Fig. 13). This might have been due to fractional crystallization or accumulation as vein magma moved upward. However, a sample taken from the top (sample 21) and one from the bottom (6A2) of El Porticito have similar compositions. Samples taken from intermediate elevations around El Porticito have randomly varying compositions, often outside the range spanned by samples 21 and 6A2. Similarly, the absence of a systematic variation in composition along the subvertical vein (compositions shown by plus symbols in Fig. 13) suggests that mineral fractionation along this vein did not result in wholesale removal of elements as magma traveled upward. This is further substantiated by the failure of attempts to model less mafic samples as resulting from Rayleigh fractionation of more mafic samples.

Alternatively, as melt was extracted from Tepb1 mush, pyroxene and Fe-Ti oxide nuclei may have been removed, as in the Hartford Basin flood basalts (Philpotts *et al.*, 1996), resulting in random, small concentrations of these nuclei in the ascending magma. As phenocrysts grew on these randomly-concentrated nuclei, the phenocrysts extracted their component elements from surrounding volumes of magma comparable to the size of collected samples ($\sim 10^{-4}$ m^3). The net effect was the de-homogenization of magma components.

Observation of outcrops clearly indicates the variable concentration of pyroxene and Fe-Ti oxide phenocrysts within veins (Fig. 5). These variable concentrations of mafic minerals correspond well with the compositions of

individual vein samples. Calculated modes of the three samples whose compositions are plotted as plus signs in Figs. 13 and 14 are listed in the Modes section of Table 4. The sum of mafic phase (cpx and Fe-Ti oxide) concentrations decreases from 31% at the top of the vein to 28% in the middle, then increases to 47% at the bottom. Corresponding visual estimates of color indices observed in hand specimens are 30%, 30%, and 50%, respectively.

Late basanite: The major element data (Fig. 13) suggest that Tepb2 might also have resulted from fractionation of Tepb1. To investigate this possibility, least squares mass balance numerical experiments were conducted. All models resulted in poor residuals. In the best model the weighted sum of squared major element oxide residuals is 0.107 (Table 4), too large to indicate a satisfactory model. Calculated compatible trace element concentrations were too high, often by orders of magnitude (Table 5). It thus appears unlikely that Tepb2 derived from a magma with the composition of Tepb1.

However, identical ε_{Nd} and similar incompatible trace element concentrations in Tepb1 and Tepb2 suggest a common parent. The differences in Al_2O_3, MgO, TiO_2, Ba, Cr, and Ni concentrations suggest that the magmas underwent somewhat different evolutionary histories, creating distinct compositions. In particular, the higher concentrations of Al, Ba, and Ti, and

lower Mg, Ni, and Cr in Tepb2 suggest more olivine and associated magnetite fractionation prior to eruption of Tepb2 than Tepb1.

Mantle derivation models

Colorado Plateau transition zone alkali basalts originate in the upper mantle (Perry *et al.*, 1987), and must traverse continental crust en route to the surface, providing opportunities for contamination, with resultant enrichment in LIL and REE elements (Menzies *et al.*, 1991) and reduction of Mg-numbers. Basalts with Mg-numbers ($100 \times Mg/(Mg + Fe^{2+})$ and $Fe^{2+} = 0.85\ Fe^{t}$) ≥68 "probably represent primary mantle magmas that were in equilibrium with upper mantle olivine compositions and subsequently erupted at the surface without significant compositional modification" (Perry *et al.* , 1987, referencing Frey *et al.*, 1978). Within the study area, all tephra and lava samples yield Mg-numbers >74, suggesting no significant crustal contamination. The lava trace element pattern in Fig. 15a shows strong enrichment of most highly incompatible elements, but with depletion of K and Rb. (The apparent relative depletion in Zr disappears with some other widely-used sets of normalization factors, e.g., Thompson *et al.*, 1984.) Thus, the pattern takes on a "spiky" (Menzies *et al.*, 1991) appearance, typical of continental crustal contamination. But most continental crust in the southwestern USA is enriched in K and Rb (Reid *et al.*, 1989), and would not be expected to impart a signature of depletion in these elements. In fact, crustal contamination should strongly

enrich a melt in K (Menzies *et al.*, 1991). The high ε_{Nd} (+3.17) also indicates that crustal contamination, if any, was small. Thus while assimilation of continental crust cannot be completely discounted, I conclude that it cannot have made a major contribution to most element concentrations in lava and tephra samples. These samples must be reasonably representative of mantle melts that have undergone some crystal fractionation prior to eruption.

Barium, Th and U are enriched relative to OIB (Fig. 15a). Barium enrichment could be due to involvement of lithospheric mantle, enriched by fluids derived from a subducting slab (Tatsumi, 1989). Thorium enrichment could result from either crustal contamination or involvement of lithospheric mantle that had been enriched in Th during suprasubduction processes associated with Mazatzal arc accretion or during interaction with a mantle plume containing recycled crustal material (Menzies *et al.*, 1991). Uranium enrichment can occur during continental crustal contamination (Rudnick & Fountain, 1995) or upper mantle involvement (Meijer *et al.*, 1990). Inasmuch as crustal contamination was minor or absent, the enrichment in Ba, Th, and U is attributed to the lithospheric mantle.

The strong REE fractionation and lack of negative Eu anomaly (Fig. 16) are consistent with low degree partial melting of a LREE-enriched source, leaving a garnet-bearing, plagioclase-free residue (Wilson, 1989). For basalts of the Snake River Plain, garnet stability in the absence of plagioclase implies an equilibration pressure ≥2 Gpa (Thompson, 1972), corresponding to a depth of

~60 km. The large Zr/Y and low Zr/Nb ratios shown in Fig. 17 (Menzies *et al.*, 1991) are also consistent with low degree partial melting.

Menzies *et al.* (1991) used the ratios K_2O/Th and La/Ta to distinguish asthenospheric and lithospheric magmas. In Fig. 18 all El Porticito samples lie in, or below, the asthenosphere field. A significant lithospheric mantle component should result in Nb and Ta depletion (Menzies *et al.*, 1991), but these are instead enriched by about a factor of two relative to OIB (Fig. 15a).

Neodymium isotopic data for both Tepb1 and Tepb2 yield $\varepsilon_{Nd} = +3.17$, suggesting derivation from a time-integrated depleted (relative to chondrites) mantle source. This isotopic composition is intermediate between depleted (asthenospheric) and enriched (lithospheric) mantle values, which have been estimated by Perry *et al.* (1987) as ~+8 for depleted mantle (DM) and ~+1 for enriched mantle (EM) and by Menzies *et al.* (1991) as ~+5 for DM and ~-4 for EM. (These estimates were for the Colorado Plateau-Basin and Range transition zone, and are not to be confused with the DM and EM's of Zindler and Hart (1986).)

These isotopic and trace element data suggest a source with composition intermediate between EM and DM (Perry *et al.*, 1987). This source is enriched in LIL (except K and Rb) and LREE elements but has a time-integrated depleted isotopic signature. The LREE enrichment must have been sufficiently recent so as not to produce an enriched isotopic signature.

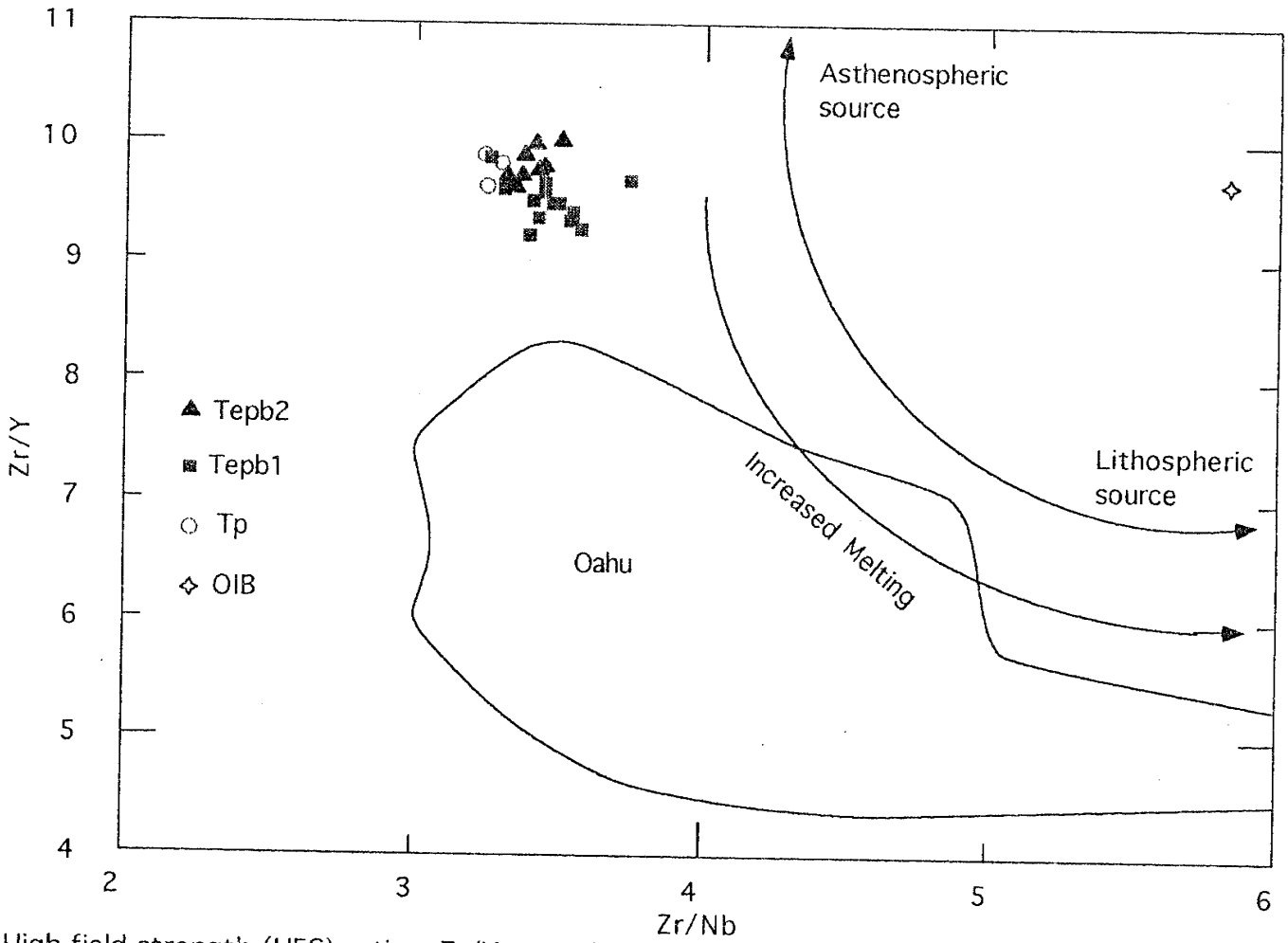

Fig. 17: High field strength (HFS) ratios, Zr/Y *vs.* Zr/Nb, indicating low degree partial melting of a mantle source (after Menzies *et al.*, 1991; OIB from Sun & McDonough, 1989.)

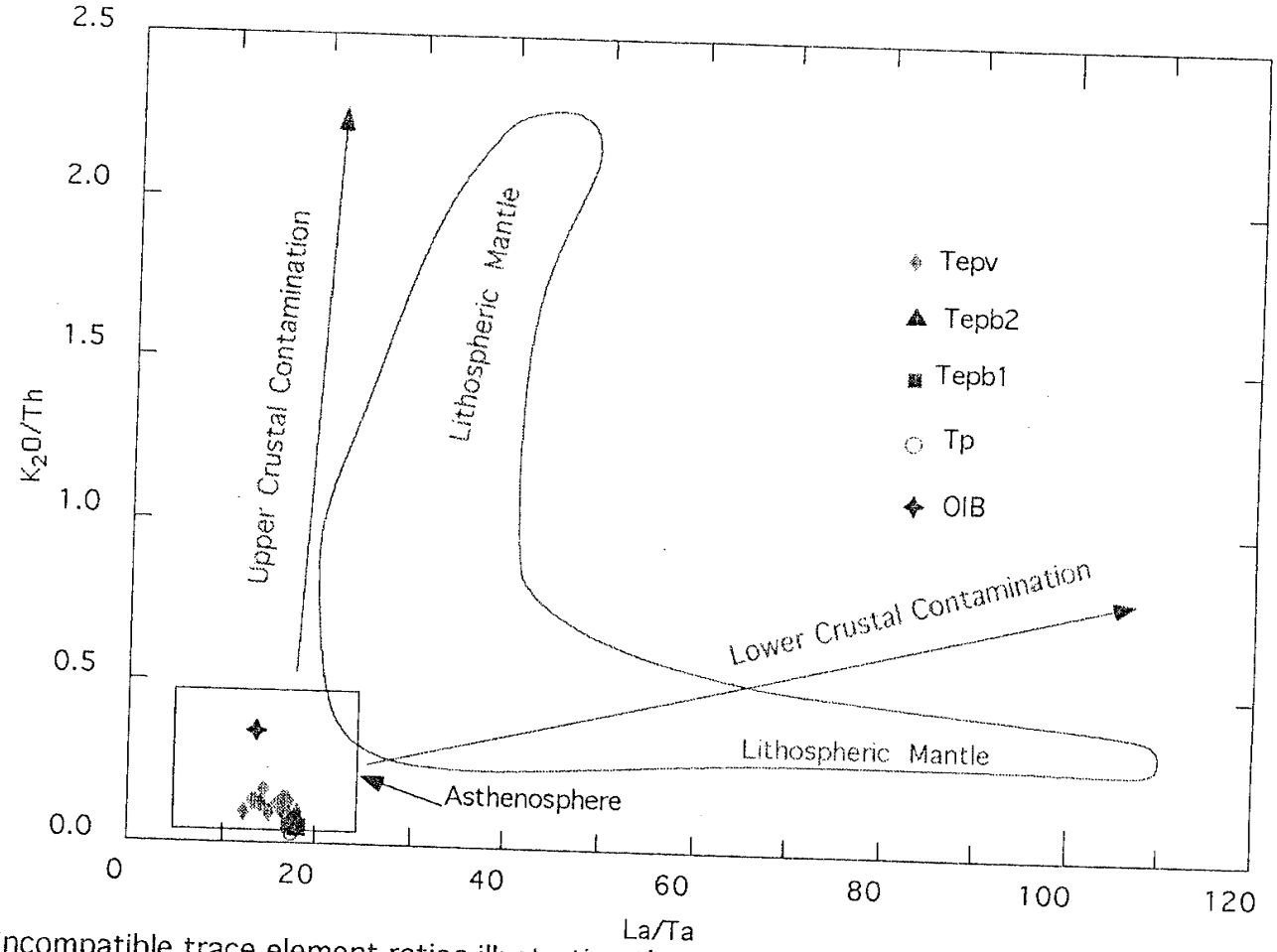

Fig. 18: Incompatible trace element ratios illustrating the similarity of pre-vein magmas with those derived from the asthenosphere, rather than the lithosphere, and suggesting little or no crustal contamination of the melt (after Menzies *et al.*, 1991; OIB from Sun & McDonough, 1989).

Vein Color

The single most eye-catching feature of El Porticito and adjacent Tejana Mesa is the coarse-grained, leucocratic veins set in melanocratic host rock. Why are the colors of these two rocks so different, whereas their chemical compositions are rather similar (Fig. 12)? The answer appears to lie in the details of chemical composition and resulting mineralogies.

The concentrations of those elements likely to impart dark color to a rock differ substantially in the two units. The MgO concentration in Tepv is less than or equal to about half that in Tepb2; and TiO_2 and total iron concentrations in Tepv average about three quarters those in Tepb2 (Fig. 13). Chrome and Ni are both important trace elements in Tepb2, but not in Tepv (Fig. 14).

Whole rock major element chemistry exerts primary control of mineralogy. The compositional distinctions between Tepb2 and Tepv led to major mineralogical differences (Appendix B). In Tepb2 the dominant minerals are titanaugite (~55-80%) and iron-titanium oxides (~10-25%). Leucocratic minerals comprise a minor portion of the groundmass, and are non-existent as phenocrysts. By contrast, veins are dominated by groundmass leucocratic phases: feldspar, analcime, leucite, zeolites, and sericite, which together comprise ~45 -90% of the rock. Titanaugite and Fe-Ti oxide phenocrysts, while notable in hand specimen and thin section, typically occupy considerably less than half the rock surface.

It has been suggested that texture may play a significant role in defining the leucocratic color of the veins (Dunbar, personal communication, 1996). The concentration of dark colored material into coarse phenocrysts might enhance the impression that veins are light in color. The Shonkin Sag laccolith, for which there are both published photos (Hurlbut & Griggs (1939), Barksdale (1937), and Barksdale (1952)) and modal analyses (Nash & Wilkinson (1970)) of rocks with wide ranges of mineral concentrations and textures available, appears to be a useful analog for exploring this possibility. Although there are obvious differences in color among the various lithologies, these more closely correspond to differences in the modal concentration of mafic minerals than to the very distinctive textures. I conclude that the relationship between texture and apparent color needs further investigation, but the correlation between mineralogy and color is certain.

Emplacement Model

Any emplacement model must account for the stratigraphic, textural, and geochemical relationships found among the volcanic units in the study area. Key points include the locations of Tepb2 outcrops relative to Tepb1 at Tejana Mesa, the indistinct contacts between Tepb1 and Tepb2, flow structures and inclusion of wall rock fragments in veins, and the chemical variability within veins.

The pyroclastic deposits, Tp, resulted from magmatic and phreatomagmatic eruptions. These are interpreted to have formed a maar-like

depression and tuff ring of unknown dimensions (Fig. 19). The alignment of other volcanic vents outside the study area suggests that the location of this tuff ring was controlled by the Mesa Tinaja Fault. The major and compatible trace element differences between bombs found at the SW and SE corners of Tejana Mesa (Appendix C and Figs. 13 and 14) may indicate different magma sources (and possibly different vents) for the two deposits. I have nevertheless grouped all tephras together stratigraphically. Their proximity to El Porticito suggests that it may have been the location of the vent for one or both of the deposits.

Lavas of Tepb1 overlie, and apparently bury, the tuff ring deposits, Tp. The major vent for Tepb1 may have been located at El Porticito; and the inferred subvertical foliation in Tepb1 now exposed at the S end of the E side of El Porticito may have developed in response to flow through the conduit during eruption. A separate, thinner flow with the composition of Tepb1 crops out at the SE corner of Tejana Mesa. The portion of this unit that has vertical contacts is interpreted to be a fissure through which a portion of Tepb1 erupted.

Ttmb lava, erupted from an unknown vent, flowed over most of the presently-exposed Tepb1 at Tejana Mesa. However no Ttmb has been observed overlying the Tepb1 flow unit at the SE corner of Tejana Mesa, and the latter may have formed a topographic high at that location. Whether

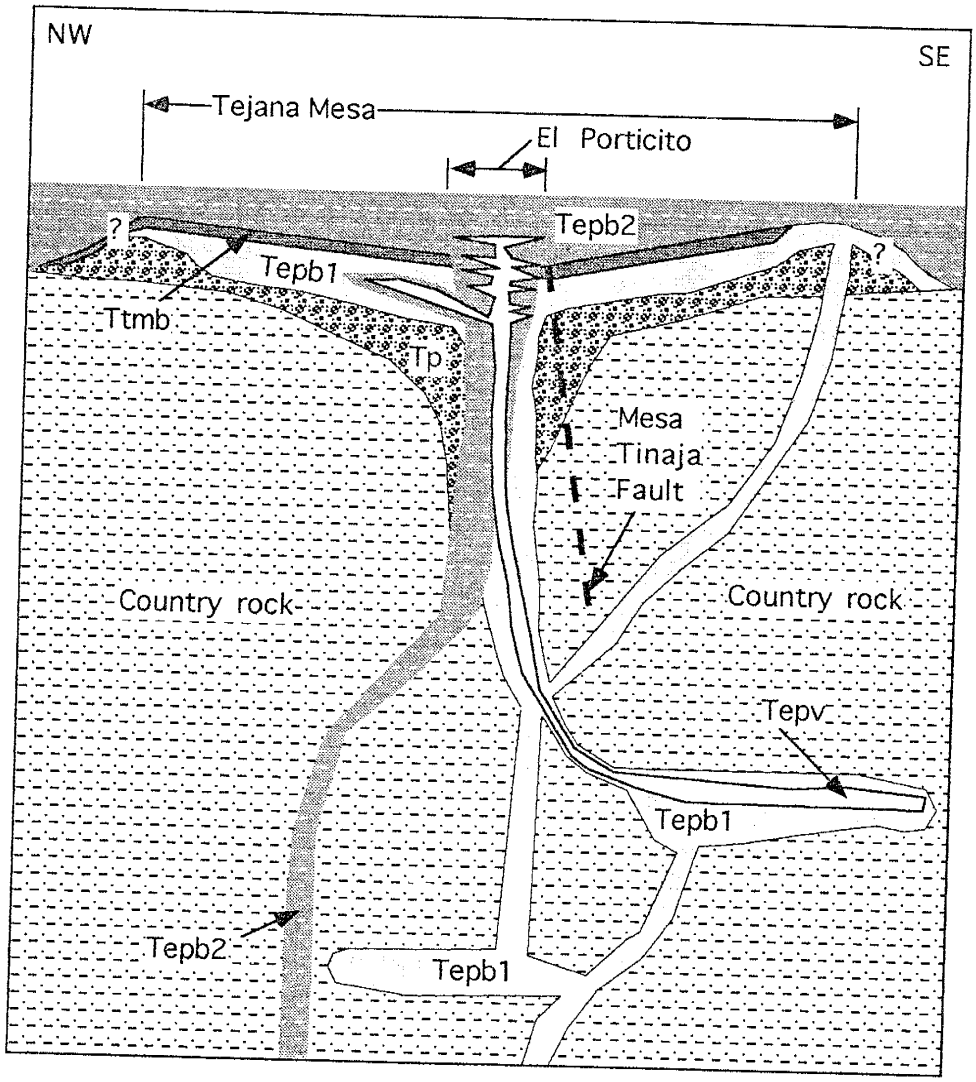

Fig. 19: Cartoon illustrating volcanic emplacement model. El Porticito has been projected into the plane of Tejana Mesa. Order of events was emplacement of Tp, Tepb1, and Ttmb; movement on Mesa Tinaja Fault to form a paleovalley; and finally emplacement of Tepb2 and Tepv (derived from a second Tepb1 chamber?). Near the surface, Tepb2 had crystallized less and was weaker than Tepb1, causing the locus of Tepv flow in the conduit to migrate from Tepb1 to Tepb2. The volcanic vent may have coincided with a strand of the Mesa Tinaja Fault. (No vertical or horizontal scales.)

Ttmb ever covered El Porticito is unknown. Movement along the preexisting Mesa Tinaja fault resulted in the formation of a paleovalley on the upper surface of Ttmb, and rotated the underlying beds, including those of Tp. This valley may have been the surface expression of a shallow magma chamber's foundering roof.

Into this paleovalley flowed Tepb2, representing a distinct magma pulse. The near-vertical contact, with no indication of faulting or erosion, between Tepb1 and Tepb2 at El Porticito is taken to indicate that Tepb2 erupted through, or beside, Tepb1 at that location; and I assume that El Porticito was the vent for the Tepb2 flow atop Tejana Mesa. Tepb2 also intruded beneath, or into, Tepb1 NW of the Mesa Tinaja fault at Tejana Mesa. The indistinct contact between the intruded Tepb2 and Tepb1 at both El Porticito and Tejana Mesa probably indicates that Tepb1 was still hot enough to be, or become, plastic near the contact during the intrusion. Such indistinct, plastic, contacts have been observed at the lower contact of the lowest and thickest intrusive sheet of the Holyoke flood basalt in the Hartford Basin, Connecticut (Philpotts *et al.*, 1996).

Since the lower contact of the Tepb2 intrusion at Tejana Mesa is everywhere covered, the precise nature of the intrusion is uncertain. Tepb2 may have intruded Tepb1; or possibly Tepb2 invaded poorly consolidated tephra underlying Tepb1. No basal flow breccia or lower vesicular zone (Aubele *et al.*, 1988) remains in Tepb1 at this location. Such structures would be

expected near the bottom of a flow, and are observed elsewhere in Tepb1 where its base is clearly exposed. Thus it appears more likely that Tepb2 intruded Tepb1 itself.

Tepv melt fractionated from Tepb1 in a shallow, upper crustal chamber. Melt segregation may have been accomplished by filter pressing. The low number density of coarse augite phenocrysts found in veins, compared to augite crystals in Tepb1, suggests that augite nuclei were removed from the Tepv magma by porous flow (Philpotts *et al.*, 1996) or fusion (Puffer & Horter, 1993) during ascent. This resulted in random concentrations of nuclei in the Tepv melt.

As Tepb2 cooled through the rheological critical melt percentage (Arzi, 1978), or critical melt fraction (van der Molen & Paterson, 1979), Tepv was injected into the solidifying magma mush. Tepb2 crystal mush shrinkage and/or foundering of solidifying upper crust may have aided the process by providing room for Tepv melt (Marsh *et al.*, 1991). Intrusion must have been forceful, as indicated by the fragments of wall rock found in veins, some apparently in the process of being detached when the veins solidified. The intrusive nature of veins implies that strong deviatoric stresses existed, forcing vein magma upward. The source of these stresses is unknown, but the Ttmb paleovalley into which Tepb2 flowed, and probably the Mesa Tinaja Fault, existed at Tepv time. Further collapse of a shallow magma chamber roof, similar to that which may have created the paleovalley, or movement along the

Mesa Tinaja Fault may have triggered Tepv emplacement and also ruptured or weakened the Tepb2 crystal mush, just as it was about to become brittle. Alternatively, differential stresses caused by crystal mush compaction in a shallow Tepb1 chamber, or buoyant rise of melt from below, may have forced Tepv magma upward. These possibilities are not mutually exclusive.

Tepb2 deformation in response to the intrusion was largely ductile; but the abrupt, angular changes in vein orientation at the NW corner of El Porticito (Fig. 4) suggest intrusion into some brittle fractures. Local vein intrusion into overlying Tepb1 at Tejana Mesa along relatively smoothly varying trajectories strengthens the conclusion that the interior of Tepb1 possessed, or developed, some ductility at the time of vein emplacement. Thus the elapsed time between emplacement of Tepb1 and Tepv must have been quite short.

The time required for the evolution and segregaton of Tepv was probably of the same order (or perhaps longer) than the time between the eruptions of Tepb1 and Tepv. This suggests that Tepv evolved in its own chamber from a separate batch of magma with the composition of Tepb1 or that the magma of the Tepb1 eruption came from the lower portion of a shared chamber and did not disturb the evolving Tepv magma.

The evolution of Tepv from Tepb1 indicates that Tepb2 magma did not mix with Tepb1 prior to Tepv extraction. But the distinct CaO contents of the least calcic Tepb2 olivine core (CaO =0.14 wt%) and the Tepb1 phenocryst core (CaO = 0.24 wt%) (Fig. 9) suggest that the Tepb1 chamber was

shallower than the Tepb2 source. A complex array of high level chambers and conduits must have existed beneath El Portico (Fig. 19), perhaps similar to that found beneath Kilauea, Hawaii (Decker, 1987; Philpotts, 1990, Fig. 4-5). Alternatively, viscosity and/or density contrasts may have prevented mixing of Tepb1 and Tepb2 magmas as Tepb2 erupted through an evolving Tepb1 chamber. Although this cannot be ruled out, it appears unlikely, in view of the similarities in their compositions and grain sizes, and the high temperatures that must have existed in Tepb1, which was still to fractionate Tepv, and Tepb2, which flowed out over Ttmb.

Once in place, vein magma cooled rapidly, as indicated by the skeletal and spherulitic groundmass feldspar morphologies, typical of strongly supercooled conditions (Lofgren, 1980). This rapid cooling produced relatively large pyroxene and Fe-Ti oxide phenocrysts. But the number density of these phenocrysts was low, and initially there were more than sufficient concentrations of necessary components for pyroxene growth. Therefore, abundant small phenocrysts also nucleated and grew on wall rock. That most small, wedge-shaped pyroxene phenocrysts remain attached to the wall rock on which they nucleated, and that phenocrysts, although broken, very seldom have fragments displaced from one another, indicates that phenocryst growth occurred after essentially all vein magma flow had ceased.

A satisfactory explanation for the formation of the submillimeter veinlets found throughout Tepb2 intrusions remains problematic. The consistent

horizontal orientation of veinlets indicates that the least principal stress was vertical, and possibly negative, at the time of their formation. Furthermore, the range of veinlet thickness, on the order of 50 to 200 μm, appears to be consistent throughout the intruded Tepb2 outcrops (except perhaps near the very top of El Porticito). It is not clear whether all veinlets formed simultaneously throughout intruded Tepb2 rock. However, the uniform veinlet thickness range suggests that mechanical properties in the volume of Tepb2 in which veinlets formed at any instant were consistent. At El Porticito itself, this uniformity extended vertically at least 60 m. Marsh *et al.* (1991), citing Moore & Evans (1967) and Wright & Okamura (1977), suggested that thermal contraction of solidifying magma may have been the mechanism that created space for segregation veins in Hawaiian lava lakes. This mechanism may have been operative in the formation of veinlets in Tepb2, but it remains unclear why veinlets are consistently horizontal. Evidently veinlet formation did depend upon the partially molten nature of Tepb2, since no veinlets have been observed in Tepb1, which was probably solid, although locally plastic, at Tepv time. That they merge smoothly into both vein and host groundmasses, mineralogically and texturally, supports the conclusion that veinlets formed while both veins and host rock contained liquid magmatic phases.

Post-emplacement Alteration

The presence of sericite, analcime, zeolites, and other low grade alteration products suggests that veins have undergone significant post-emplacement alteration, probably by hydrothermal fluids. Silicate alteration phases and subordinate vermicular Fe-Ti oxide grains commonly occur in thin zones along vein-wall rock contacts. I infer that these zones were originally composed of volcanic glass formed as magma chilled against wall rock; and that the present mineral assemblage formed during devitrification and hydrothermal alteration of this glass. Analcime in particular crystallizes in several circumstances (Tschernich, 1992), including the hydrothermal alteration of basic glasses (Höller & Wirsching, 1978; Lo, 1978). The hydrothermal fluids probably traveled along the vein-wall rock contact through cracks that formed as vein magma continued to cool and contract after glass formation.

Crystalline phases also have undergone post-emplacement alteration. Throughout veins, titanaugite and Fe-Ti oxide phenocrysts, although sometimes severely altered to uralite(?), chlorite, Fe-Ti oxides, and clay (titanaugite phenocrysts) and biotite(?) and hematite (Fe-Ti oxide phenocrysts), generally retain their euhedral habits, including substantially straight edges. This is interpreted to indicate that most alteration was the result of low grade chemical reactions with hydrous (hydrothermal?) fluids. This contrasts with anorthoclase microphenocrysts, which exhibit rounded, irregular margins, consistent with crystal resorption during reaction with surrounding magma.

An explanation for the relationships between V concentrations found in Tepb1, Tepb2, and Tepv, and within Tepv, remains problematic. Whole rock vanadium concentration is strongly correlated with both Fe and Ti (Figs. 13 & 14); the correlation with Ti being somewhat stronger. Of the phases most likely to contain significant V, its concentration is likely to be greatest in Fe-Ti oxide grains, since the partition coefficient of V is highest in this phase (Rollinson, 1993). Within the Fe-Ti oxide grains that have been analyzed (Appendix A), V exhibits no correlation with Fe or Ti. The product of V concentration (~2000 ppm) in the Fe-Ti oxide grains found in lavas and the estimated modal concentrations of this phase (~10%, Appendix B) is ~100% of the measured whole rock V concentration (~200 ppm). Therefore, other phases such as pyroxene, must contain little V.

Thin section visual modal estimates were not performed on sample 25B, the vein sample chosen for mass balance petrogenetic calculations, however all vein modal analyses that were performed yielded estimated concentrations of Fe-Ti oxides of 12±5% (Appendix B). Furthermore, sample 15, for which modal estimates were made (17% Fe-Ti oxides), and 25B have nearly identical concentrations of TiO_2 and Fe_2O_3. The V concentrations are 200 ppm and 268 ppm, respectively (Appendix C). On the assumption that the Fe-Ti oxide crystal concentration in sample 25B approximates that in sample 15, calculations, similar to those for the lavas, indicate that the entire whole rock V in sample 25B is probably concentrated in Fe-Ti oxide grains.

But calculations (Table 5) based upon published mineral-melt partition coefficients indicate that V found in the model mafic Tepv (sample 25B) is substantially in excess of that which could have been produced through fractionation of its parent, Tepb1. Assuming Rayleigh crystal fractionation of a parent with 250 ppm V, 31.6% melt, and a bulk D of 2.02, (Table 5) the daughter should contain only 80 ppm V, not 268 ppm (Appendix C). Thus, the V concentration in Fe-Ti oxide grains appears to be consistent with the whole rock V_2O_3 concentration in both veins and lavas, but fractionation calculations indicate that there is a large excess of V in veins relative to that in the parent. The source of this excess is unknown. It may be due to post-emplacement alteration of veins (or of both veins and lavas), in which V replaced Fe and/or Ti in Fe-Ti oxide grains that originally contained little V.

CONCLUSIONS

Two chemically distinct black basanite lavas and white tephrite-phonotephrite veins, all emplaced at 7.08 ± 0.25 Ma, form El Porticito and most of the adjacent Tejana Mesa. The two basanites were derived from a common mantle source. The eruptive sequence began with the formation of a tuff ring, whose vent is inferred to be El Porticito. Into this tuff ring flowed the first, less-evolved basanite. After emplacement of a lava of unknown origin atop the first basanite, movement along the Mesa Tinaja fault created a paleovalley into which erupted the second basanite. This second, less-evolved basanite erupted

through the first at El Porticito and also intruded the first basanite at Tejana Mesa.

The melt that formed the white veins fractionated at depth from magma of the first basanite. Vein melt carried pyroxene and Fe-Ti oxide crystal nuclei, now represented by coarse phenocrysts in the central portions of veins, through ruptures in the second basanite's crystallizing magma residing in the El Porticito conduit, stopping when it reached the upper rigid crust (Marsh *et al.*, 1991). Thus, unlike veins found in other mafic bodies (e.g. Shonkin Sag laccolith (Osborne & Roberts, 1931), Kilauea Iki lava lake (Helz *et al.*, 1989)), and flood basalts of the Hartford Basin (Philpotts *et al.*, 1996), the veins of El Porticito evolved from a parent of different composition from the host in which they were emplaced. There was little or no mixing of vein and host magmas during vein emplacement, probably because of the large viscosity contrast between the magmas.

The salient feature at El Porticito is the distinct origins of veins and their host rock; each derived from separate, identifiable, pulses of magma that evolved from the mantle. The color of the veins, controlled by mineralogy, and the occurrence of their intrusion just as their host reached critical crystallinity, created the unique appearance of El Porticito.

APPENDIX A: Microprobe Mineral Analysis

Standard 2.6 × 4.6 cm polished thin sections were prepared without cover slips. The sections were cleaned, then coated with a carbon film to provide an electrically conductive surface. Mineral grains in the thin sections were analyzed to determine compositions using a Caméca SX50 electron microprobe at the Los Alamos National Laboratory. Calibration standards were selected according to the mineral types to be analyzed. For the analysis of salic minerals, the probe was calibrated using orthoclase, sanidine, anorthite, labradorite, and glass. For mafic minerals, two augites, four olivines, two chromites, and a magnetite were used. Replicate analyses of standards generally resulted in agreement with accepted compositional values within 4 wt%. The detection limit for all oxides is estimated to be ~0.05 wt%.

In the following tables, mineral analyses are grouped according to phase, and for each phase according to the unit (Tp, Tepb1, etc.) from which the samples were taken. End member compositions of feldspars, feldspathoids, pyroxenes, and Fe-Ti oxides were determined by calculating the cation proportions per structural formula (Klein & Hurlbut, 1993). For pyroxenes, iron was partitioned into Fe^{2+} and Fe^{3+} using the charge balance method of Baldridge (1979), and for Fe-Ti oxides using the method of Stormer (1983).

Petrographic identification (Appendix B) of opaque phases was not accomplished for any of the grains analyzed with the microprobe. Microprobe data were used to calculate end member concentrations assuming both

ilmenite-hematite and ulvöspinel-magnetite solution series. Those computations that resulted in negative values for either iron oxidation state were discarded, and the alternative solid solution series was chosen in classifying the grain. But where computations for both solid solution series resulted in negative values, or where total oxide wt%, adjusted for iron oxidation state, was unsatisfactory, the probe analysis was considered bad. The most common cause for bad analyses was exsolution lamellae of width comparable to probe spot size. In most grains with very thin lamellae, calculations suggested that both solid solution series were present in the same grain. Probe analyses for these grains were also considered bad. The Stormer method produces mathematically reasonable values for both solid solution series if the concentrations of cations other than those of Fe and Ti are low enough. In these cases, that series for which the better total oxides or more consistent results were obtained was chosen for identification purposes. After rejection of bad or ambiguous results, analyses for only three grains are considered to be of sufficient quality for use in petrogenic modelling: 19a1-18 & -19, 21.1-33 through -36, and 21.1-38 through -41.

Appendix A: Microprobe Mineral Analyses
Olivines

	27d-46	27d-11	27d-47	27d-12	27d-48	27d-49	27d-17	27d-50	27d-51	27d-18	27d-55	27d-52	27d-53	27d-54	27d-24	27d-58	27d-59	27d-60
	Large groundmass microphenocryst					*Very small phenocryst*				Tp *Very small phenocryst*					*~1.5mm anhedral phenocryst*			
Oxide wt%	rim	rim	core	core	rim	rim	rim	core	rim	rim	rim	core	core	rim	rim	rim	core	rim
SiO_2	39.5	39.5	39.4	40.3	40.0	39.9	39.8	40.1	39.9	39.8	39.5	39.7	39.7	40.4	39.6	39.5	39.9	40.0
Al_2O_3	n.d.	0.1	n.d.	n.d.	n.d.	n.d.	n.d.	n.d.	n.d.	n.d.	n.d.	n.d.	n.d.	n.d.	0.1	n.d.	n.d.	n.d.
FeO	13.4	14.0	12.2	12.6	12.6	12.5	12.6	12.0	12.6	13.7	13.7	13.9	13.5	13.4	14.4	14.0	10.3	14.3
MnO	0.2	0.2	0.2	0.2	0.2	0.2	0.2	0.2	0.2	0.2	0.2	0.2	0.2	0.2	0.2	0.3	0.2	0.2
MgO	46.0	45.6	47.7	47.9	47.2	46.6	47.4	47.7	47.2	46.6	45.6	46.2	46.8	46.5	45.8	45.5	49.3	45.1
CaO	0.5	0.6	0.3	0.4	0.3	0.3	0.4	0.2	0.3	0.4	0.4	0.4	0.1	0.4	0.5	0.4	0.1	0.4
Cr_2O_3	n.d.	n.d.	n.d.	n.d.	0.1	n.d.	0.1	0.1	n.d.	n.d.	n.d.	n.d.	n.d.	n.d.	n.d.	n.d.	0.1	n.d.
NiO	0.2	n.a.	0.2	n.a.	0.2	0.2	n.a.	0.4	0.3	n.a.	0.2	0.3	0.3	0.3	n.a.	0.3	0.4	0.3
ZnO	n.d.	n.a.	n.d.	n.a.	n.d.	n.d.	n.a.	0.1	n.d.	n.a.	0.1	0.1	0.0	0.1	n.a.	n.d.	n.d.	n.d.
Sum	99.9	100.2	100.0	101.3	100.6	99.8	100.3	100.7	100.4	100.6	99.7	100.7	100.7	101.2	100.5	100.0	100.3	100.4
	Formula based upon 4 oxygens:																	
Si	0.991	0.990	0.981	0.988	0.991	0.995	0.987	0.992	0.990	0.989	0.994	0.990	0.988	0.999	0.989	0.993	0.985	1.001
Fe	0.281	0.294	0.255	0.259	0.261	0.261	0.262	0.247	0.261	0.284	0.289	0.289	0.281	0.276	0.300	0.294	0.212	0.299
Mn	0.005	0.005	0.003	0.004	0.005	0.003	0.003	0.004	0.004	0.004	0.004	0.005	0.003	0.004	0.004	0.006	0.004	0.005
Mg	1.718	1.705	1.771	1.752	1.743	1.736	1.751	1.760	1.746	1.725	1.710	1.716	1.737	1.712	1.705	1.704	1.813	1.683
Ca	0.014	0.016	0.008	0.010	0.009	0.009	0.009	0.005	0.009	0.010	0.010	0.011	0.003	0.011	0.013	0.011	0.001	0.011
Total	3.009	3.010	3.019	3.012	3.009	3.005	3.013	3.008	3.010	3.011	3.006	3.010	3.012	3.001	3.011	3.007	3.015	2.999
MO%	0.68	0.81	0.41	0.47	0.43	0.46	0.47	0.24	0.45	0.49	0.51	0.56	0.15	0.54	0.65	0.54	0.07	0.55
FO%	85.14	84.38	86.91	86.55	86.38	86.39	86.44	87.32	86.42	85.27	84.94	84.90	85.81	85.47	84.29	84.60	89.29	84.23
FA%	13.93	14.57	12.52	12.79	12.96	12.98	12.92	12.27	12.92	14.04	14.36	14.31	13.87	13.80	14.84	14.58	10.46	14.97
TE%	0.24	0.23	0.16	0.19	0.23	0.17	0.17	0.18	0.20	0.20	0.19	0.23	0.16	0.19	0.22	0.28	0.19	0.25
Mg*	85.94	85.27	87.41	87.13	86.96	86.93	87.00	87.68	86.99	85.87	85.54	85.57	86.08	86.10	85.03	85.30	89.51	84.91

MO: Monticellite (Ca-rich)
FA: Fayalite (Fe-rich)
FO: Forsterite (Mg-rich)
TE: Tephroite (Mn-rich)
Mg*: Mg/(Mg+Fe) with elements expressed as ionic proportions after normalization to 4 oxygens per formula unit
n.a.: not analyzed
n.d.: below detection limit

Appendix A: Microprobe Mineral Analyses
Olivines

	27d-61	27d-27	27d-62	27d-63	27d-28	27d-64	27d-65	27d-66	27d-67	27d-29	27d-68	27d-69	27d-70	27d-56	27d-71	27d-72	27d-73	27d-74
	Euhedral groundmass microphenocryst				*Euhedral ~1.5mm phenocryst*				Tp *Corroded subhedral phenocryst*					*Anhed gndmss mpheno*	*~1.5mm anhedral phenocryst*			
Oxide wt%	rim	rim	core	rim	rim	rim	core	rim	rim	rim	core	core	rim	core	rim	core	rim	rim
SiO_2	40.1	40.1	40.1	40.4	39.3	39.7	40.0	40.0	39.9	39.1	39.8	39.7	40.4	40.6	40.0	39.3	39.7	40.0
Al_2O_3	n.d.	n.d.	0.1	n.d.	0.2	n.d.	n.d.	n.d.	n.d.	n.d.	n.d.	n.d.	0.3	n.d.	n.d.	n.d.	n.d.	n.d.
FeO	12.2	12.7	12.5	12.1	13.8	14.0	13.1	13.3	13.3	13.2	12.9	12.8	13.1	12.7	13.6	14.1	14.4	13.8
MnO	0.1	0.2	0.1	0.2	0.2	0.2	0.1	0.2	0.2	0.2	0.2	0.2	0.2	0.2	0.2	0.3	0.2	0.2
MgO	47.2	47.5	47.2	48.2	46.0	45.6	47.1	46.5	46.9	46.7	47.0	47.3	45.9	46.9	46.5	45.7	46.3	46.3
CaO	0.3	0.3	0.2	0.2	0.5	0.4	0.1	0.2	0.2	0.2	0.2	0.1	0.3	0.4	0.1	n.d.	n.d.	0.1
Cr_2O_3	0.1	0.1	0.1	0.1	n.d.	n.d.	n.d.	n.d.	0.1	0.1	n.d.	0.1	n.d.	n.d.	n.d.	n.d.	n.d.	n.d.
NiO	0.3	n.a.	0.4	0.4	n.a.	0.3	0.4	0.4	0.3	n.a.	0.4	0.4	0.3	0.3	0.3	0.4	0.4	0.4
ZnO	n.d.	n.a.	n.d.	0.1	n.a.	n.d.	n.d.	n.d.	n.d.	n.a.	n.d.	n.d.	n.d.	0.0	0.0	0.1	n.d.	n.d.
Sum	100.3	100.8	100.9	101.5	99.9	100.3	100.8	100.6	100.9	99.5	100.5	100.5	100.5	101.2	100.8	99.8	101.0	100.7
Si	0.996	0.989	0.994	0.991	0.987	0.994	0.992	0.995	0.991	0.982	0.990	0.987	1.006	1.000	0.993	0.990	0.989	0.995
Fe	0.254	0.262	0.258	0.248	0.290	0.294	0.271	0.276	0.276	0.277	0.268	0.266	0.272	0.262	0.282	0.297	0.300	0.286
Mn	0.003	0.004	0.003	0.003	0.004	0.004	0.003	0.003	0.004	0.004	0.004	0.003	0.003	0.004	0.005	0.006	0.004	0.005
Mg	1.745	1.749	1.745	1.763	1.720	1.703	1.738	1.725	1.732	1.749	1.743	1.752	1.705	1.724	1.723	1.717	1.717	1.716
Ca	0.007	0.008	0.006	0.005	0.012	0.010	0.003	0.006	0.007	0.006	0.005	0.004	0.008	0.010	0.003	0.001	0.001	0.003
Total	3.004	3.011	3.006	3.009	3.013	3.006	3.008	3.005	3.009	3.018	3.010	3.013	2.994	3.000	3.007	3.010	3.011	3.005
MO%	0.36	0.39	0.30	0.25	0.61	0.52	0.15	0.29	0.33	0.28	0.23	0.18	0.39	0.52	0.15	0.06	0.06	0.16
FO%	86.86	86.47	86.72	87.33	84.90	84.66	86.25	85.81	85.80	85.95	86.30	86.50	85.76	86.19	85.60	84.97	84.93	85.37
FA%	12.63	12.95	12.84	12.26	14.30	14.61	13.46	13.73	13.68	13.59	13.26	13.14	13.69	13.09	14.00	14.69	14.82	14.24
TE%	0.15	0.18	0.15	0.16	0.20	0.21	0.14	0.17	0.20	0.18	0.22	0.17	0.16	0.21	0.25	0.28	0.19	0.23
Mg*	87.31	86.98	87.11	87.69	85.59	85.29	86.50	86.21	86.25	86.35	86.68	86.81	86.24	86.82	85.94	85.26	85.14	85.71

Appendix A: Microprobe Mineral Analyses
Olivines

	27d-75	27d-38	27d-76	27d-77	27d-39	27d-78	27d-79	27d-80	27d-81	27d-82	27d-83	27d-84	27d-85	27d-86
							Tp							
	Small phenocryst						*Large groundndmass microphenocryst*				*~0.5mm subhedral phenocryst*			
Oxide wt%	rim	rim	core	core	core	rim	rim	core	core	rim	rim	core	core	rim
SiO_2	39.8	40.3	40.3	40.3	40.2	40.5	40.1	40.2	40.0	40.4	39.8	40.1	40.3	40.2
Al_2O_3	0.2	0.4	n.d.	0.1	n.d.	n.d.	n.d.	n.d.	n.d.	n.d.	n.d.	n.d.	n.d.	n.d.
FeO	13.2	13.1	12.1	12.3	12.1	12.2	13.3	12.2	12.1	12.5	12.8	13.3	13.3	12.6
MnO	0.2	0.2	0.1	0.1	0.1	0.1	0.2	0.1	0.2	0.1	0.2	0.2	0.2	0.2
MgO	46.0	45.5	47.4	48.0	48.4	47.5	46.6	47.7	47.3	47.8	47.2	47.3	47.0	47.5
CaO	0.4	0.5	0.2	0.2	0.2	0.3	0.4	0.2	0.2	0.2	0.3	0.2	n.d.	0.3
Cr_2O_3	n.d.	n.d.	0.1	0.1	0.1	n.d.	0.1	0.1	0.1	0.1	0.1	n.d.	n.d.	n.d.
NiO	0.3	n.a.	0.5	0.4	n.a.	0.3	0.3	0.3	0.4	0.3	0.2	0.3	0.3	0.3
ZnO	0.1	n.a.	0.0	0.1	n.a.	n.d.	0.1	n.d.	n.d.	n.d.	n.d.	n.d.	0.1	n.d.
Sum	100.1	100.1	100.7	101.6	101.1	100.9	101.0	100.8	100.3	101.5	100.7	101.5	101.2	101.1
Si	0.996	1.006	0.998	0.991	0.987	0.998	0.994	0.993	0.994	0.992	0.988	0.989	0.994	0.991
Fe	0.276	0.274	0.250	0.252	0.249	0.252	0.276	0.251	0.251	0.258	0.266	0.274	0.275	0.260
Mn	0.004	0.005	0.003	0.002	0.002	0.002	0.004	0.003	0.003	0.003	0.004	0.004	0.004	0.004
Mg	1.717	1.694	1.747	1.758	1.770	1.743	1.721	1.755	1.752	1.750	1.744	1.739	1.731	1.746
Ca	0.012	0.014	0.005	0.005	0.006	0.007	0.011	0.006	0.006	0.006	0.009	0.006	0.001	0.007
Total	3.004	2.994	3.002	3.009	3.013	3.002	3.006	3.007	3.006	3.008	3.012	3.011	3.006	3.009
MO%	0.58	0.69	0.23	0.27	0.27	0.37	0.55	0.31	0.29	0.31	0.43	0.28	0.05	0.36
FO%	85.48	85.25	87.13	87.11	87.33	86.96	85.54	87.09	87.07	86.77	86.20	85.97	86.07	86.54
FA%	13.73	13.80	12.49	12.51	12.28	12.55	13.70	12.45	12.48	12.78	13.16	13.54	13.66	12.91
TE%	0.21	0.26	0.14	0.11	0.11	0.12	0.21	0.15	0.16	0.14	0.21	0.20	0.22	0.19
Mg*	86.16	86.07	87.46	87.44	87.67	87.39	86.19	87.49	87.47	87.16	86.75	86.39	86.30	87.02

Appendix A: Microprobe Mineral Analyses
Olivines

	19A1-47	19A1-48	19A1-49	19A1-50	19A1-51	19A1-52	19A1-53	19A1-54	19A1-55	19A1-56	19A1-57	19A1-58	19A1-59	19A1-60	19A1-61
	Tepb1														
	2 mm anhedral phenocryst														
Oxide wt%	rim	core	core	core	core	core	core	core	core	core	core	core	core	core	rim
SiO_2	38.8	40.0	40.4	40.6	40.8	40.4	40.4	40.6	40.4	40.4	40.3	40.2	40.7	40.1	38.8
Al_2O_3	n.d.	n.d.	n.d.	n.d.	n.d.	n.d.	n.d.	n.d.	n.d.	n.d.	n.d.	n.d.	n.d.	n.d.	n.d.
FeO	17.5	11.1	9.3	9.6	9.5	9.3	9.6	9.6	9.5	9.6	9.6	9.5	9.6	11.0	18.1
MnO	0.4	0.1	0.2	0.2	0.1	0.1	0.2	0.1	0.1	0.1	0.2	0.1	0.2	0.2	0.4
MgO	42.9	48.7	49.6	49.9	49.9	49.6	50.1	49.9	49.8	50.2	49.8	50.1	49.9	48.5	42.7
CaO	0.5	0.1	0.0	0.1	0.1	0.1	0.0	0.1	0.1	0.1	0.1	0.1	0.1	0.1	0.5
Cr_2O_3	n.d.	n.d.	n.d.	n.d.	n.d.	n.d.	n.d.	n.d.	n.d.	n.d.	n.d.	n.d.	n.d.	n.d.	n.d.
NiO	0.2	0.4	0.4	0.5	0.5	0.5	0.4	0.5	0.5	0.4	0.5	0.5	0.5	0.4	0.2
ZnO	0.1	n.d.	n.d.	n.d.	n.d.	n.d.	n.d.	n.d.	n.d.	n.d.	n.d.	n.d.	n.d.	n.d.	n.d.
Sum	100.4	100.4	100.0	100.8	100.8	100.0	100.7	100.7	100.4	100.7	100.4	100.5	100.9	100.2	100.6
Si	0.988	0.988	0.992	0.991	0.994	0.992	0.988	0.992	0.991	0.987	0.990	0.985	0.991	0.991	0.987
Fe	0.374	0.228	0.192	0.197	0.193	0.191	0.196	0.196	0.194	0.196	0.196	0.194	0.197	0.227	0.386
Mn	0.008	0.002	0.003	0.004	0.002	0.002	0.004	0.002	0.003	0.003	0.003	0.003	0.003	0.003	0.008
Mg	1.629	1.791	1.819	1.816	1.814	1.820	1.825	1.817	1.820	1.827	1.820	1.832	1.816	1.785	1.620
Ca	0.013	0.002	0.001	0.001	0.001	0.002	0.001	0.001	0.002	0.001	0.002	0.001	0.002	0.002	0.012
Total	3.012	3.012	3.008	3.009	3.006	3.008	3.012	3.008	3.009	3.013	3.010	3.015	3.009	3.009	3.013
MO%	0.64	0.08	0.06	0.07	0.07	0.09	0.03	0.07	0.08	0.07	0.08	0.07	0.08	0.12	0.61
FO%	80.49	88.53	90.26	90.00	90.21	90.31	90.12	90.11	90.15	90.15	90.06	90.24	90.00	88.45	79.95
FA%	18.46	11.27	9.52	9.76	9.60	9.50	9.67	9.70	9.63	9.65	9.70	9.55	9.75	11.26	19.03
TE%	0.41	0.12	0.17	0.17	0.12	0.11	0.18	0.12	0.14	0.12	0.17	0.15	0.16	0.17	0.41
Mg*	81.34	88.70	90.46	90.22	90.38	90.48	90.31	90.28	90.35	90.33	90.28	90.43	90.22	88.71	80.77

Appendix A: Microprobe Mineral Analyses
Olivines

	19a1-103	19a1-104	19a1-105	19a1-64 Tepb1	19a1-102	19a1-107	19a1-114
	.25 mm anhedral phenocryst			*Mpheno*	*Very small pheno*	*Micropheno*	*Small pheno*
Oxide wt%	rim	core	rim	core	core	core	core
SiO_2	38.0	38.4	38.2	38.3	38.3	38.0	38.3
Al_2O_3	n.d.	n.d.	n.d.	n.d.	n.d.	n.d.	n.d.
FeO	19.0	16.0	19.4	21.4	20.2	18.3	19.5
MnO	0.4	0.2	0.4	n.a.	0.5	0.4	n.a.
MgO	40.8	43.7	41.1	39.7	40.5	41.6	41.1
CaO	0.6	0.2	0.5	0.5	0.5	0.5	0.5
Cr_2O_3	n.d.	n.d.	n.d.	n.a.	n.d.	n.d.	n.d.
NiO	0.2	0.2	0.1	n.a.	0.1	0.2	n.a.
ZnO	n.d.	n.d.	n.d.	n.a.	n.d.	n.d.	n.a.
Sum	98.9	98.8	99.7	99.9	100.2	99.1	99.3
Si	0.989	0.986	0.987	0.993	0.990	0.986	0.990
Fe	0.413	0.343	0.420	0.464	0.437	0.397	0.422
Mn	0.009	0.004	0.009	0.000	0.011	0.009	0.000
Mg	1.582	1.674	1.582	1.536	1.558	1.608	1.584
Ca	0.017	0.007	0.013	0.014	0.015	0.014	0.014
Total	3.011	3.014	3.013	3.007	3.010	3.014	3.010
MO%	0.84	0.32	0.65	0.69	0.73	0.69	0.68
FO%	78.30	82.55	78.14	76.25	77.11	79.29	78.42
FA%	20.43	16.93	20.76	23.06	21.64	19.56	20.91
TE%	0.44	0.20	0.45	0.00	0.53	0.45	0.00
Mg*	79.31	82.98	79.01	76.78	78.09	80.21	78.95

Appendix A: Microprobe Mineral Analyses
Olivines

	5b-45	5b-46	5b-47	5b-48	5b-49	5b-50	5b-51	5b-52	5b-53	5b-55 Tepb2	5b-56	5b-57	5b-58	5b-59	5b-60	5b-61	5b-62	5b-63	5b-64
	Moderately corroded phenocryst				*Moderately corroded phenocryst*					*Severely corroded phenocryst*			*Severely corroded phenocryst*				*Severely corroded phenocryst*		
Oxide wt%	core	core	core	rim	rim	core	core	core	rim	rim	rim	rim	rim	core	rim	rim	rim	core	rim
SiO_2	39.1	40.2	39.3	37.0	37.1	37.3	38.0	37.9	37.3	36.6	36.9	37.1	37.1	38.1	37.3	37.6	37.1	38.3	37.2
Al_2O_3	0.1	n.d.	0.1	0.2	n.d.	n.d.	n.d.	n.d.	n.d.	0.2	n.d.	n.d.	0.1	n.d.	0.1	n.d.	n.d.	n.d.	n.d.
FeO	13.4	11.8	15.9	23.7	26.1	23.1	22.2	22.3	26.1	26.3	25.6	25.4	24.4	21.3	25.0	23.9	25.2	20.1	26.2
MnO	0.2	0.2	0.2	0.5	0.6	0.6	0.4	0.5	0.6	0.6	0.5	0.5	0.6	0.4	0.5	0.5	0.6	0.4	0.7
MgO	45.7	47.1	43.8	36.6	35.1	37.8	39.1	37.9	35.0	34.2	35.6	36.3	36.3	39.2	35.7	37.1	36.0	40.4	34.8
CaO	0.2	0.1	0.2	0.5	0.5	0.4	0.3	0.3	0.5	0.6	0.5	0.5	0.5	0.2	0.5	0.4	0.4	0.2	0.5
Cr_2O_3	n.d.	n.d.	0.1	n.d.	n.d.	n.d.	n.d.	n.d.	n.d.	n.d.	n.d.	n.d.	n.d.	n.d.	n.d.	n.d.	n.d.	n.d.	n.d.
NiO	0.4	0.3	0.3	0.2	0.2	0.2	0.2	0.2	0.1	0.1	0.2	0.1	0.2	0.3	0.2	0.3	0.2	0.2	0.1
ZnO	0.1	n.d.	n.d.	n.d.	n.d.	n.d.	n.d.	n.d.	n.d.	0.1	n.d.	n.d.	n.d.	n.d.	n.d.	n.d.	n.d.	n.d.	0.1
Sum	99.2	99.8	99.9	98.5	99.5	99.4	100.2	99.2	99.4	98.5	99.3	100.0	99.0	99.6	99.2	99.8	99.6	99.6	99.5
Si	0.990	1.000	0.998	0.992	0.994	0.987	0.991	0.999	0.998	0.994	0.989	0.985	0.992	0.995	0.996	0.993	0.990	0.993	0.997
Fe	0.284	0.246	0.338	0.531	0.585	0.510	0.483	0.492	0.584	0.597	0.574	0.565	0.545	0.466	0.559	0.527	0.563	0.437	0.587
Mn	0.004	0.004	0.005	0.011	0.013	0.013	0.009	0.011	0.012	0.013	0.012	0.012	0.013	0.010	0.011	0.012	0.014	0.008	0.015
Mg	1.728	1.747	1.658	1.462	1.401	1.492	1.517	1.489	1.395	1.386	1.421	1.439	1.445	1.527	1.423	1.462	1.431	1.562	1.390
Ca	0.004	0.003	0.004	0.013	0.013	0.011	0.009	0.010	0.014	0.016	0.014	0.014	0.014	0.007	0.014	0.012	0.013	0.007	0.013
Total	3.010	3.000	3.002	3.008	3.006	3.013	3.009	3.001	3.002	3.006	3.011	3.015	3.008	3.005	3.004	3.007	3.010	3.007	3.003
MO%	0.20	0.14	0.20	0.65	0.64	0.56	0.44	0.49	0.69	0.82	0.68	0.68	0.67	0.34	0.68	0.62	0.63	0.33	0.67
FO%	85.54	87.35	82.69	72.48	69.63	73.63	75.19	74.37	69.57	68.86	70.28	70.90	71.68	75.98	70.92	72.63	70.83	77.57	69.34
FA%	14.08	12.31	16.88	26.34	29.09	25.18	23.94	24.58	29.12	29.67	28.42	27.83	27.03	23.19	27.86	26.18	27.87	21.70	29.25
TE%	0.17	0.20	0.23	0.54	0.64	0.64	0.43	0.57	0.62	0.65	0.61	0.60	0.63	0.49	0.54	0.57	0.67	0.40	0.74
Mg*	85.86	87.65	83.04	73.35	70.53	74.51	75.85	75.16	70.49	69.89	71.20	71.81	72.62	76.62	71.80	73.50	71.76	78.14	70.33

Appendix A: Microprobe Mineral Analyses
Olivines

	5b-65	5b-66	5b-67	6b-36	6b-37	6b-38	6b-23	6b-24	6b-25	6b-26	6b-27	6b-28	6b-29	6b-30	6b-31	6b-32	6b-33	6b-34	6b-35
										Tepb2									
	Severely corroded phenocryst			*Fractured phenocryst*			*Subhedral phenocryst in glomerocryst*								*Pheno in glomero*	*Pheno in glomero*	*Pheno in glomero*	*Pheno in glomero*	*Pheno in glomero*
Oxide wt%	rim	core	rim	rim	core	rim	rim	rim	core	core	core	core	core	core	core	core	core	core	core
SiO_2	36.3	37.6	35.7	37.5	38.4	37.2	37.8	38.9	39.9	39.8	39.8	39.9	40.3	40.0	40.0	39.1	39.2	39.5	40.0
Al_2O_3	0.4	n.d.	0.9	n.d.	n.d.	n.d.	n.d.	n.d.	n.d.	n.d.	n.d.	n.d.	n.d.	n.d.	n.d.	n.d.	n.d.	n.d.	n.d.
FeO	25.6	22.2	27.8	25.2	23.9	25.9	23.3	20.1	14.0	13.7	13.2	13.4	13.7	14.0	13.5	18.9	17.3	17.6	14.8
MnO	0.5	0.4	0.6	0.6	0.4	0.6	0.5	0.4	0.2	0.2	0.2	0.3	0.2	0.2	0.3	0.3	0.3	0.3	0.3
MgO	34.7	38.5	32.5	35.8	38.3	36.7	37.7	40.8	46.4	46.5	46.5	47.1	46.8	46.4	46.6	41.7	42.8	42.8	45.0
CaO	0.5	0.3	0.6	0.4	0.3	0.4	0.4	0.2	n.d.	0.2	0.1	n.d.	n.d.	0.1	0.1	0.1	0.1	0.1	0.1
Cr_2O_3	n.d.	n.d.	n.d.	n.d.	n.d.	n.d.	n.d.	n.d.	n.d.	n.d.	n.d.	n.d.	n.d.	n.d.	n.d.	n.d.	n.d.	n.d.	n.d.
NiO	0.1	0.1	0.2	0.2	0.2	0.2	0.2	0.3	0.3	0.4	0.4	0.4	0.4	0.4	0.4	0.2	0.2	0.3	0.4
ZnO	n.d.	n.d.	n.d.	0.1	n.d.	0.1	0.1	n.d.	n.d.	n.d.	n.d.	0.1	n.d.	n.d.	n.d.	0.1	n.d.	n.d.	n.d.
Sum	98.0	99.1	98.3	99.8	101.4	101.1	100.1	100.6	100.8	100.8	100.2	101.1	101.4	101.1	100.8	100.5	100.0	100.5	100.6
Si	0.990	0.991	0.989	0.997	0.994	0.981	0.993	0.997	0.993	0.990	0.994	0.988	0.995	0.992	0.994	0.998	0.998	1.002	1.001
Fe	0.584	0.490	0.645	0.559	0.517	0.571	0.512	0.431	0.290	0.286	0.276	0.277	0.283	0.291	0.280	0.405	0.369	0.372	0.311
Mn	0.011	0.010	0.015	0.013	0.009	0.012	0.011	0.009	0.004	0.004	0.004	0.006	0.004	0.005	0.006	0.007	0.007	0.006	0.005
Mg	1.411	1.511	1.345	1.420	1.477	1.443	1.478	1.561	1.718	1.725	1.730	1.741	1.722	1.716	1.725	1.588	1.625	1.616	1.680
Ca	0.014	0.007	0.017	0.013	0.009	0.011	0.012	0.007	0.001	0.005	0.002	0.001	0.001	0.003	0.002	0.003	0.003	0.002	0.002
Total	3.010	3.009	3.011	3.003	3.006	3.019	3.007	3.003	3.007	3.010	3.006	3.012	3.005	3.008	3.006	3.002	3.002	2.998	2.999
MO%	0.67	0.36	0.82	0.63	0.43	0.53	0.58	0.33	0.06	0.24	0.11	0.05	0.03	0.15	0.11	0.17	0.15	0.08	0.10
FO%	69.85	74.89	66.53	70.81	73.43	70.82	73.42	77.78	85.32	85.38	85.98	86.00	85.67	85.16	85.70	79.25	81.11	80.95	84.09
FA%	28.92	24.27	31.93	27.89	25.68	28.04	25.43	21.46	14.41	14.17	13.70	13.67	14.08	14.43	13.89	20.20	18.41	18.65	15.55
TE%	0.56	0.48	0.72	0.67	0.46	0.61	0.56	0.43	0.21	0.22	0.21	0.28	0.21	0.26	0.30	0.37	0.33	0.32	0.27
Mg*	70.72	75.52	67.57	71.74	74.09	71.64	74.27	78.37	85.55	85.77	86.26	86.28	85.88	85.51	86.05	79.69	81.50	81.28	84.40

Appendix A: Microprobe Mineral Analyses
Pyroxenes

	27d-1	27d-2	27d-3	27d-4	27d-5	27d-6	27d-7	27d-8	27d-9	27d-14	27d-15	27d-16	27d-21	27d-22	27d-23	27d-40	27d-41	27d-42
									Tp									
	~1.5 cm euhedral, corroded phenocryst									~1mm long, euhedral, fractured phenocryst			~.5mm, euhedral phenocryst			~1mm long phenocryst		
Oxide Wt%	rim	core	core	core	core	core	core	core	rim	rim	core	rim	rim	core	rim	rim	core	rim
SiO_2	48.8	51.1	52.5	51.6	52.0	52.5	49.0	51.0	49.2	49.3	51.1	51.7	49.7	50.1	45.1	50.3	51.4	50.4
TiO_2	2.1	1.2	1.0	1.1	1.1	0.7	1.7	1.2	2.0	1.8	1.1	0.9	1.9	1.2	3.8	1.5	0.9	1.6
Al_2O_3	3.5	2.4	2.0	2.8	2.6	2.7	3.6	2.2	3.3	3.9	3.5	2.7	2.9	2.5	6.5	3.2	3.3	3.4
FeO^t	5.9	4.1	3.9	4.1	4.2	4.1	5.2	4.4	6.0	5.3	4.6	3.9	5.8	4.2	7.8	4.4	4.8	4.7
MnO	0.1	0.1	0.1	0.1	0.1	0.1	0.1	0.1	0.1	0.1	0.1	0.1	0.1	0.1	0.1	0.1	0.1	0.1
MgO	14.8	16.1	16.6	16.2	16.4	17.0	15.0	16.2	15.1	15.1	16.0	16.6	15.1	16.1	12.6	15.5	16.3	15.5
CaO	22.9	23.4	23.4	23.0	23.0	21.6	23.3	23.2	22.7	23.1	22.3	22.6	23.1	23.3	22.3	23.2	21.4	22.9
Na_2O	0.3	0.4	0.3	0.3	0.4	0.5	0.4	0.3	0.3	0.4	0.5	0.4	0.3	0.4	0.5	0.4	0.6	0.3
Cr_2O_3	0.1	0.9	0.7	0.8	0.7	1.0	0.4	0.6	0.2	0.7	0.9	0.8	0.1	0.8	n.d.	1.0	1.0	0.9
SrO	n.d.	n.d.	n.d.	n.d.	n.d.	n.d.	n.d.	n.d.	n.d.	n.d.	n.d.	n.d.	n.d.	n.d.	n.d.	n.d.	n.d.	n.d.
NiO	n.a.	n.a.	n.a.	n.a.	n.a.	n.a.	n.a.	n.a.	n.a.	n.a.	n.a.	n.a.	n.a.	n.a.	n.a.	n.a.	n.a.	n.a.
Sum	98.7	99.5	100.5	100.0	100.3	100.2	98.7	99.2	98.9	99.8	100.0	99.8	99.0	98.6	98.71	99.6	99.8	99.7
FeO	2.90	1.82	2.70	2.74	2.75	2.86	1.57	2.20	3.25	2.19	2.71	2.12	3.23	0.77	3.944	2.38	2.78	3.14
Fe_2O_3	3.38	2.59	1.29	1.47	1.64	1.32	3.98	2.44	3.03	3.51	2.06	2.03	2.91	3.79	4.317	2.25	2.23	1.67
Total	98.99	99.75	100.59	100.10	100.51	100.36	99.09	99.43	99.17	100.11	100.20	99.99	99.30	98.95	99.145	99.82	99.98	99.91
T-site:																		
Si	1.866	1.913	1.927	1.908	1.915	1.924	1.875	1.917	1.873	1.862	1.896	1.917	1.885	1.910	1.75	1.885	1.909	1.879
Al	0.134	0.087	0.073	0.092	0.085	0.076	0.125	0.083	0.127	0.138	0.104	0.083	0.115	0.090	0.25	0.115	0.091	0.121
Fe^{3+}	0.000	0.000	0.000	0.000	0.000	0.000	0.000	0.000	0.000	0.000	0.000	0.000	0.000	0.000	0.000	0.000	0.000	0.000
M1-site:																		
Al	0.024	0.020	0.015	0.030	0.028	0.041	0.036	0.013	0.020	0.035	0.047	0.036	0.015	0.021	0.048	0.026	0.052	0.027
Fe^{3+}	0.097	0.073	0.036	0.041	0.046	0.036	0.115	0.069	0.087	0.100	0.058	0.057	0.083	0.109	0.126	0.064	0.062	0.047
Ti	0.061	0.033	0.029	0.031	0.030	0.021	0.048	0.035	0.058	0.052	0.030	0.025	0.055	0.034	0.110	0.043	0.024	0.046
Cr	0.002	0.025	0.022	0.024	0.019	0.028	0.013	0.017	0.005	0.022	0.026	0.023	0.003	0.025	0.000	0.029	0.030	0.027
Mg	0.816	0.849	0.899	0.875	0.877	0.874	0.788	0.865	0.830	0.790	0.839	0.860	0.844	0.812	0.715	0.838	0.832	0.853
Fe^{2+}	0.000	0.000	0.000	0.000	0.000	0.000	0.000	0.000	0.000	0.000	0.000	0.000	0.000	0.000	0.000	0.000	0.000	0.000
Mn	0.000	0.000	0.000	0.000	0.000	0.000	0.000	0.000	0.000	0.000	0.000	0.000	0.000	0.000	0.000	0.000	0.000	0.000
M2-site:																		
Mg	0.028	0.047	0.007	0.017	0.022	0.053	0.067	0.040	0.025	0.059	0.047	0.059	0.009	0.100	0.014	0.026	0.070	0.009
Fe^{2+}	0.093	0.057	0.083	0.085	0.085	0.088	0.050	0.069	0.103	0.069	0.084	0.066	0.103	0.024	0.128	0.074	0.086	0.098
Mn	0.004	0.002	0.002	0.002	0.002	0.004	0.003	0.002	0.003	0.002	0.002	0.002	0.003	0.003	0.003	0.003	0.003	0.002
Ca	0.939	0.938	0.922	0.911	0.908	0.848	0.956	0.934	0.926	0.936	0.886	0.897	0.939	0.951	0.928	0.931	0.853	0.913
Na	0.024	0.026	0.021	0.024	0.026	0.039	0.029	0.020	0.022	0.028	0.034	0.029	0.021	0.027	0.037	0.028	0.044	0.025
Sum M2:	1.087	1.071	1.035	1.039	1.042	1.032	1.106	1.066	1.079	1.095	1.053	1.053	1.075	1.105	1.11	1.062	1.056	1.046
EN%	42.69	45.58	46.50	46.19	46.37	48.69	43.18	45.74	43.32	43.41	46.25	47.33	43.06	45.62	38.10	44.62	47.34	44.86
WO%	47.51	47.70	47.29	47.19	46.83	44.56	48.33	47.19	46.89	47.82	46.25	46.25	47.44	47.59	48.46	48.09	44.72	47.49
FS%	9.80	6.72	6.21	6.62	6.80	6.74	8.49	7.08	9.79	8.76	7.51	6.42	9.50	6.79	13.45	7.28	7.94	7.66
Mg^*	81.63	87.35	88.43	87.66	87.35	88.18	83.83	86.78	81.82	83.41	86.22	88.25	82.14	87.27	74.16	86.23	85.86	85.61

Appendix A: Microprobe Mineral Analyses
Pyroxenes

	27d-32	27d-33	27d-34	27d-19	27d-20	27d-35	27d-36	27d-37	27d-25	27d-26	27d-30	27d-31	27d-43	27d-44	27d-45	19a1-4	19a1-12	19a1-14
		Groundmass euhedral microphenocryst		Gnd-mass micro	Gnd-mass micro	Small phenocryst			Tp Gnd-mass micro	Gnd-mass micro	Groundmass anhedral microphenocryst		Gnd-mass micro	Gnd-mass micro	Gnd-mass micro	Gnd-mass micro	Gnd-mass micro	Gnd-mass micro
Oxide Wt%	rim	core	rim	core	core	rim	core	rim	core	core	rim	core	core	core	core	core	core	core
SiO_2	48.6	52.6	51.1	45.7	47.6	47.0	49.5	47.9	46.4	47.1	50.7	51.0	49.8	46.2	44.1	46.0	50.0	46.3
TiO_2	2.1	0.5	1.5	3.4	3.2	2.5	1.8	2.7	3.3	3.0	1.3	1.1	1.7	3.1	3.3	3.6	1.8	3.4
Al_2O_3	3.5	1.9	2.5	6.0	5.3	4.8	4.1	4.9	5.8	5.3	2.9	2.1	3.1	5.3	8.0	4.9	13.5	6.2
FeO[t]	6.1	5.2	4.7	6.8	7.6	6.2	5.4	6.6	6.6	6.8	4.4	4.8	5.1	6.4	8.4	8.3	3.9	6.6
MnO	0.1	0.1	0.1	0.1	0.1	0.1	0.1	n.d.	0.1	n.d.	0.1	0.1	0.1	0.1	0.2	n.a.	n.a.	n.a.
MgO	15.0	16.8	16.0	13.4	13.4	13.9	14.8	13.8	13.5	13.8	15.8	16.2	15.6	13.6	11.0	13.3	7.6	13.1
CaO	22.8	21.8	23.3	22.9	22.2	22.9	22.7	22.8	22.8	22.8	23.2	22.9	22.7	22.8	19.3	22.1	12.9	22.1
Na_2O	0.3	0.4	0.3	0.4	0.6	0.4	0.5	0.4	0.4	0.4	0.4	0.3	0.4	0.4	1.1	0.6	5.2	0.7
Cr_2O_3	0.2	0.5	0.4	0.4	0.1	0.1	0.6	0.0	0.4	0.5	0.9	0.5	0.9	0.5	0.1	n.a.	n.a.	n.a.
SrO	n.d.	n.d.	n.d.	n.d.	n.d.	n.d.	n.d.	n.d.	n.d.	n.d.	n.d.	n.d.	n.d.	n.d.	n.d.	0.1	0.1	n.d.
NiO	n.a.	n.a.	n.a.	n.a.	n.a.	n.a.	n.a.	n.a.	n.a.	n.a.	n.a.	n.a.	n.a.	n.a.	n.a.	n.a.	n.a.	n.a.
Sum	98.7	99.8	99.8	99.2	100.1	98.0	99.4	99.2	99.2	99.6	99.6	98.9	99.3	98.4	95.6	98.8	95.0	98.5
FeO	2.35	3.44	2.56	2.48	4.50	2.52	3.07	3.99	3.21	3.30	2.10	2.43	2.56	2.37	5.85	3.48	7.02	3.43
Fe_2O_3	4.15	1.99	2.35	4.85	3.41	4.13	2.62	2.95	3.79	3.90	2.60	2.59	2.84	4.52	2.85	5.40	0.00	3.51
Total	99.10	100.03	99.99	99.66	100.40	98.40	99.64	99.46	99.55	100.02	99.91	99.15	99.61	98.86	95.92	99.36	98.12	98.81
T-site:																		
Si	1.864	1.948	1.906	1.769	1.803	1.823	1.863	1.823	1.779	1.799	1.898	1.922	1.882	1.793	1.742	1.795	1.789	1.777
Al	0.136	0.052	0.094	0.231	0.197	0.177	0.137	0.177	0.221	0.201	0.102	0.078	0.118	0.207	0.258	0.205	0.211	0.223
Fe^{3+}	0.000	0.000	0.000	0.000	0.000	0.000	0.000	0.000	0.000	0.000	0.000	0.000	0.000	0.000	0.000	0.000	0.000	0.000
M1-site:																		
Al	0.023	0.031	0.018	0.041	0.039	0.043	0.045	0.041	0.041	0.038	0.027	0.016	0.021	0.034	0.115	0.022	0.359	0.059
Fe^{3+}	0.120	0.055	0.066	0.141	0.097	0.120	0.074	0.084	0.110	0.112	0.073	0.073	0.081	0.132	0.085	0.158	0.000	0.101
Ti	0.060	0.015	0.041	0.100	0.091	0.074	0.050	0.076	0.095	0.085	0.037	0.032	0.047	0.090	0.097	0.105	0.048	0.099
Cr	0.006	0.015	0.011	0.012	0.004	0.002	0.018	0.001	0.011	0.014	0.025	0.015	0.027	0.016	0.005	0.000	0.000	0.000
Mg	0.790	0.884	0.865	0.707	0.758	0.760	0.812	0.785	0.744	0.751	0.838	0.864	0.824	0.728	0.650	0.715	0.408	0.741
Fe^{2+}	0.000	0.000	0.000	0.000	0.011	0.000	0.000	0.012	0.000	0.000	0.000	0.000	0.000	0.000	0.049	0.000	0.186	0.000
Mn	0.000	0.000	0.000	0.000	0.000	0.000	0.000	0.000	0.000	0.000	0.000	0.000	0.000	0.000	0.000	0.000	0.000	0.000
M2-site:																		
Mg	0.071	0.043	0.027	0.068	0.000	0.042	0.016	0.000	0.027	0.034	0.045	0.046	0.053	0.059	0.000	0.056	0.000	0.006
Fe^{2+}	0.075	0.107	0.080	0.080	0.132	0.082	0.097	0.114	0.103	0.106	0.066	0.077	0.081	0.077	0.145	0.113	0.024	0.110
Mn	0.003	0.003	0.002	0.003	0.004	0.003	0.002	0.000	0.003	0.001	0.003	0.003	0.002	0.003	0.006	0.000	0.000	0.000
Ca	0.937	0.867	0.931	0.949	0.900	0.952	0.917	0.930	0.936	0.932	0.933	0.924	0.918	0.950	0.819	0.923	0.495	0.909
Na	0.024	0.030	0.021	0.031	0.045	0.029	0.035	0.029	0.030	0.030	0.026	0.020	0.026	0.033	0.086	0.046	0.363	0.055
Sum M2:	1.111	1.049	1.061	1.131	1.081	1.108	1.067	1.073	1.100	1.104	1.071	1.070	1.079	1.123	1.055	1.139	0.882	1.080
EN%	43.11	47.34	45.24	39.76	39.85	40.94	43.19	40.75	40.10	40.53	45.09	45.80	44.79	40.37	37.08	39.24	36.64	40.01
WO%	46.95	44.26	47.27	48.72	47.34	48.60	47.78	48.28	48.67	48.15	47.66	46.50	46.85	48.77	46.71	46.93	44.50	48.67
FS%	9.94	8.40	7.49	11.53	12.80	10.46	9.03	10.97	11.23	11.32	7.25	7.70	8.36	10.86	16.20	13.83	18.87	11.32
Mg*	81.51	85.13	85.94	77.78	75.97	79.86	82.89	78.78	78.39	78.27	86.38	85.85	84.44	79.01	70.04	73.94	66.01	77.95

Appendix A: Microprobe Mineral Analyses
Pyroxenes

	19a1-23	19a1-24	19a1-25	19a1-26	19a1-27	19a1-28	19a1-29	19a1-30	19a1-31	19a1-32	19a1-33	19a1-34	19a1-35	19a1-36	19a1-37	19a1-20	19a1-21	19a1-22
	Tepb1																	
	596 microns wide X 1.25 mm long tabular phenocryst															*Small pheno (97 microns wide)*		
Oxide Wt%	rim	core	core	core	core	core	core	core	core	core	core	core	core	core	rim	rim	core	rim
SiO_2	46.8	50.1	50.9	50.6	51.4	51.9	52.1	52.1	51.7	50.3	50.3	49.1	46.7	45.9	47.5	48.2	50.5	46.6
TiO_2	3.0	1.8	1.4	1.5	1.2	1.1	1.1	1.2	1.2	1.6	1.7	2.2	3.0	3.1	3.0	2.5	1.7	3.3
Al_2O_3	5.8	3.6	3.2	3.4	2.6	2.6	2.6	2.7	2.7	3.5	3.5	4.3	5.9	6.0	5.5	4.8	3.5	6.1
FeO^t	6.6	4.9	4.6	4.8	4.2	4.1	4.1	4.2	4.2	4.8	5.1	6.0	7.2	7.1	6.4	6.1	4.8	6.8
MnO	0.1	n.d.	0.1	0.1	0.1	0.1	0.1	0.1	n.d.	0.1	0.1	0.1	0.1	0.1	0.1	0.1	0.1	0.1
MgO	13.4	15.3	15.6	15.4	16.1	16.0	16.0	16.0	16.1	15.1	15.2	14.5	13.0	12.8	13.4	14.0	15.3	13.1
CaO	22.6	22.9	22.8	22.9	23.1	22.8	23.2	22.9	23.1	22.9	22.7	22.7	22.6	23.0	22.5	22.6	23.0	22.5
Na_2O	0.6	0.4	0.4	0.4	0.4	0.4	0.4	0.4	0.4	0.4	0.4	0.4	0.6	0.7	0.6	0.5	0.3	0.5
Cr_2O_3	0.1	0.7	0.8	0.8	0.9	0.9	1.0	0.9	0.9	0.8	0.6	0.4	0.1	n.d.	0.1	0.3	0.8	0.2
SrO	n.d.	n.d.	n.d.	n.d.	n.d.	n.d.	n.d.	n.d.	n.d.	n.d.	n.d.	n.d.	n.d.	n.d.	n.d.	n.d.	n.d.	n.d.
NiO	n.d.	n.d.	0.1	n.d.	0.1	n.d.	n.d.	0.1	0.1	0.1	n.d.	n.d.	0.1	n.d.	0.1	n.d.	n.d.	n.d.
Sum	98.9	99.6	99.8	99.8	99.8	99.8	100.5	100.4	100.3	99.6	99.5	99.7	99.2	98.8	99.0	99.1	99.9	99.1
FeO	3.17	3.27	3.07	3.28	2.56	3.44	3.13	3.59	2.85	3.25	3.62	3.86	3.59	2.20	3.95	3.56	3.57	4.16
Fe_2O_3	3.80	1.79	1.67	1.68	1.85	0.71	1.03	0.69	1.48	1.68	1.59	2.40	4.07	5.42	2.71	2.79	1.38	2.96
Total	99.32	99.79	100.02	100.01	99.98	99.84	100.59	100.47	100.45	99.76	99.65	99.93	99.64	99.30	99.32	99.37	100.02	99.41
T-site:																		
Si	1.792	1.873	1.892	1.884	1.909	1.914	1.913	1.911	1.907	1.879	1.879	1.847	1.792	1.784	1.803	1.829	1.877	1.778
Al	0.208	0.127	0.108	0.116	0.091	0.086	0.087	0.089	0.093	0.121	0.121	0.153	0.208	0.216	0.197	0.171	0.123	0.222
Fe^{3+}	0.000	0.000	0.000	0.000	0.000	0.000	0.000	0.000	0.000	0.000	0.000	0.000	0.000	0.000	0.000	0.000	0.000	0.000
M1-site:																		
Al	0.055	0.031	0.033	0.033	0.024	0.026	0.025	0.026	0.024	0.034	0.032	0.039	0.058	0.060	0.050	0.044	0.030	0.051
Fe^{3+}	0.110	0.050	0.047	0.047	0.052	0.020	0.028	0.019	0.041	0.047	0.045	0.068	0.117	0.159	0.077	0.080	0.038	0.085
Ti	0.088	0.049	0.038	0.043	0.033	0.031	0.030	0.032	0.034	0.045	0.048	0.063	0.087	0.092	0.087	0.071	0.047	0.095
Cr	0.003	0.021	0.025	0.023	0.026	0.025	0.028	0.025	0.026	0.023	0.017	0.010	0.003	0.000	0.003	0.010	0.022	0.005
Mg	0.745	0.849	0.857	0.853	0.866	0.880	0.877	0.875	0.875	0.843	0.847	0.814	0.735	0.689	0.758	0.794	0.847	0.743
Fe^{2+}	0.000	0.000	0.000	0.001	0.000	0.018	0.010	0.023	0.000	0.007	0.012	0.006	0.000	0.000	0.025	0.001	0.016	0.021
Mn	0.000	0.000	0.000	0.000	0.000	0.000	0.000	0.000	0.000	0.000	0.000	0.000	0.000	0.000	0.000	0.000	0.000	0.000
M2-site:																		
Mg	0.021	0.003	0.009	0.000	0.024	0.000	0.000	0.000	0.010	0.000	0.000	0.000	0.008	0.054	0.000	0.000	0.000	0.000
Fe^{2+}	0.102	0.102	0.095	0.101	0.080	0.088	0.086	0.087	0.088	0.094	0.101	0.115	0.115	0.072	0.100	0.112	0.095	0.112
Mn	0.004	0.001	0.002	0.002	0.002	0.003	0.002	0.002	0.001	0.003	0.002	0.003	0.003	0.004	0.002	0.003	0.003	0.003
Ca	0.926	0.915	0.908	0.911	0.919	0.899	0.912	0.901	0.914	0.917	0.909	0.913	0.931	0.958	0.914	0.918	0.914	0.921
Na	0.041	0.026	0.030	0.030	0.026	0.028	0.028	0.027	0.026	0.030	0.028	0.029	0.043	0.049	0.045	0.036	0.024	0.037
Sum M2:	1.094	1.047	1.044	1.043	1.050	1.018	1.028	1.018	1.040	1.044	1.040	1.060	1.101	1.138	1.061	1.068	1.037	1.072
EN96	40.15	44.36	45.16	44.53	45.82	46.14	45.79	45.89	45.88	44.09	44.19	42.44	38.91	38.40	40.40	41.63	44.25	39.43
WO96	48.57	47.63	47.33	47.59	47.31	47.12	47.60	47.22	47.37	47.99	47.44	47.56	48.75	49.50	48.70	48.14	47.77	48.87
FS96	11.28	8.01	7.51	7.88	6.87	6.73	6.61	6.89	6.75	7.92	8.36	10.00	12.34	12.11	10.90	10.23	7.98	11.69
Mg*	78.37	84.82	85.90	85.11	87.13	87.51	87.58	87.16	87.27	84.99	84.29	81.15	76.16	76.37	78.89	80.49	85.00	77.33

Appendix A: Microprobe Mineral Analyses
Pyroxenes

	19a1-38	19a1-39	19a1-40	19a1-41	19a1-42	19a1-43	19a1-44	19a1-45	19a1-46	19a1-17	19a1-62	19a1-63	19a1-65	19a1-67	19a1-100	19a1-101	19a1-108	19a1-109
	Subequant subhedral phenocryst, ~400 microns across, with inclusion (which was not analyzed) in core									Tepb1								
Oxide Wt%	rim	core	core	core	core	core	core	rim	rim	*Gnd-mass micro* core	*Gnd-mass micro* core	*Gnd-mass micro* core	*Gnd-mass micro* core	*Gnd-mass micro* core	*Gnd-mass micro* core	*Gnd-mass micro* core	*Gnd-mass micro* core	*Groundmass interstitial grain* core core
SiO_2	50.5	52.2	51.9	52.6	52.2	51.0	52.1	49.8	49.2	51.9	49.1	50.3	49.5	47.0	47.9	45.6	44.8	47.8
TiO_2	1.5	1.1	1.0	1.0	1.0	1.2	1.1	1.3	2.0	1.8	2.7	2.0	1.7	2.9	2.8	3.4	3.7	2.6
Al_2O_3	3.4	2.3	2.2	2.0	2.0	2.6	2.2	3.4	4.3	2.1	3.3	2.6	3.1	5.2	4.6	6.1	5.2	4.4
FeO^t	4.4	4.2	4.2	4.0	3.9	4.3	4.0	4.5	5.7	6.2	6.6	5.7	6.0	6.3	6.1	7.2	9.8	7.0
MnO	n.d.	n.d.	0.1	n.d.	0.1	0.1	0.1	0.1	0.1	0.2	n.a.	n.a.	n.a.	n.a.	0.1	0.1	0.1	0.1
MgO	15.4	16.2	16.2	16.3	16.3	15.7	16.3	15.3	14.6	14.7	13.7	14.7	14.7	13.4	13.6	12.7	13.0	13.9
CaO	22.7	23.1	22.6	23.1	23.0	23.1	22.8	22.5	22.7	22.2	22.1	23.0	21.8	23.1	22.8	22.7	21.2	22.5
Na_2O	0.4	0.3	0.3	0.3	0.3	0.4	0.3	0.4	0.4	0.7	0.8	0.7	0.9	0.6	0.5	0.6	0.9	0.6
Cr_2O_3	1.0	0.8	0.7	0.6	0.6	0.8	0.7	0.9	0.5	n.d.	n.a.	n.a.	n.a.	n.a.	0.6	n.d.	n.d.	n.d.
SrO	n.d.	n.d.	n.d.	n.d.	n.d.	n.d.	n.d.	n.d.	n.d.	0.1	0.1	0.1	0.2	0.1	n.a.	n.a.	n.a.	n.a.
NiO	n.d.	0.1	n.d.	n.d.	n.d.	n.d.	n.d.	n.d.	n.d.	0.1	n.a.	n.a.	n.a.	n.a.	n.d.	n.d.	n.d.	n.d.
Sum	99.3	100.2	99.2	100.2	99.5	98.9	99.6	98.1	99.4	99.8	98.4	99.0	97.8	98.6	98.9	98.5	98.8	98.9
FeO	3.29	3.57	3.65	3.51	3.29	2.79	3.56	2.79	3.57	5.51	4.60	2.95	2.53	2.48	3.77	2.72	2.36	3.23
Fe_2O_3	1.22	0.73	0.56	0.55	0.68	1.64	0.53	1.87	2.38	0.76	2.24	3.03	3.90	4.26	2.54	4.94	8.28	4.22
Total	99.46	100.27	99.22	100.21	99.56	99.11	99.65	98.27	99.63	99.87	98.64	99.31	98.20	99.01	99.20	98.99	99.63	99.35
T-site:																		
Si	1.884	1.919	1.924	1.930	1.929	1.909	1.921	1.887	1.853	1.922	1.867	1.903	1.901	1.812	1.823	1.776	1.784	1.836
Al	0.116	0.081	0.076	0.070	0.071	0.091	0.079	0.113	0.147	0.078	0.133	0.097	0.099	0.188	0.177	0.224	0.216	0.164
Fe^{3+}	0.000	0.000	0.000	0.000	0.000	0.000	0.000	0.000	0.000	0.000	0.000	0.000	0.000	0.000	0.000	0.000	0.000	0.000
M1-site:																		
Al	0.032	0.021	0.021	0.018	0.017	0.023	0.018	0.038	0.042	0.014	0.015	0.018	0.040	0.046	0.030	0.054	0.029	0.037
Fe^{3+}	0.034	0.020	0.016	0.015	0.019	0.046	0.015	0.053	0.068	0.021	0.064	0.086	0.113	0.123	0.073	0.145	0.248	0.122
Ti	0.042	0.029	0.029	0.028	0.028	0.034	0.030	0.038	0.057	0.049	0.078	0.056	0.050	0.085	0.079	0.099	0.112	0.075
Cr	0.029	0.022	0.019	0.019	0.017	0.022	0.020	0.026	0.014	0.000	0.000	0.000	0.000	0.000	0.018	0.001	0.002	0.001
Mg	0.855	0.885	0.892	0.892	0.900	0.874	0.896	0.845	0.819	0.808	0.777	0.829	0.797	0.746	0.773	0.701	0.609	0.765
Fe^{2+}	0.008	0.022	0.023	0.028	0.018	0.000	0.021	0.000	0.000	0.108	0.066	0.011	0.000	0.000	0.027	0.000	0.000	0.000
Mn	0.000	0.000	0.000	0.000	0.000	0.000	0.000	0.000	0.000	0.000	0.000	0.000	0.000	0.000	0.000	0.000	0.000	0.000
M2-site:																		
Mg	0.000	0.000	0.000	0.000	0.000	0.002	0.000	0.017	0.000	0.000	0.000	0.000	0.042	0.025	0.000	0.038	0.162	0.030
Fe^{2+}	0.095	0.087	0.090	0.080	0.084	0.088	0.089	0.089	0.112	0.063	0.080	0.082	0.081	0.080	0.093	0.088	0.079	0.104
Mn	0.001	0.001	0.002	0.001	0.002	0.002	0.002	0.002	0.003	0.005	0.000	0.000	0.000	0.000	0.002	0.003	0.005	0.003
Ca	0.909	0.910	0.899	0.908	0.909	0.926	0.901	0.916	0.914	0.882	0.900	0.931	0.898	0.953	0.932	0.946	0.905	0.927
Na	0.029	0.021	0.024	0.024	0.022	0.026	0.022	0.028	0.030	0.053	0.061	0.053	0.067	0.047	0.037	0.049	0.068	0.042
Sum M2:	1.033	1.020	1.014	1.013	1.017	1.044	1.014	1.051	1.060	1.003	1.042	1.066	1.087	1.104	1.064	1.125	1.219	1.105
EN%	44.97	45.94	46.45	46.36	46.58	45.22	46.58	44.88	42.72	42.83	41.15	42.74	43.47	39.99	40.67	38.47	38.41	40.76
WO%	47.77	47.24	46.77	47.19	47.05	47.78	46.82	47.65	47.71	46.74	47.71	48.01	46.49	49.46	49.05	49.25	45.06	47.51
FS%	7.26	6.82	6.79	6.45	6.37	7.00	6.60	7.47	9.56	10.43	11.14	9.25	10.04	10.55	10.28	12.28	16.53	11.73
Mg*	86.21	87.21	87.41	87.88	88.17	86.76	87.80	85.87	81.98	80.83	78.69	82.20	81.23	79.12	80.02	76.03	70.23	77.90

Appendix A: Microprobe Mineral Analyses
Pyroxenes

	19a1-110	19a1-111	19a1-112	19a1-113	19a1-116	19a1-117	19a1-118	1b-160	1b-161	1b-162	1b-163	1b-164	1b-165	5b-5	5b-6	5b-7	5b-10	5b-11
				Tepb1									Tepb2					
	Grd-mass micro	*Grd-mass micro*	*Grd-mass micro*	*Grd-mass micro*	*Grd-mass micro*	*Grd-mass micro*	*Grd-mass micro*	*600 X 1000 micron wall rock euhedral phenocryst, 11 mm from wall rock-vein contact*						*1000 X 350 wedge-shaped, euhedral, fractured phenocryst*			*Euhedral, fractured phenocryst*	
Oxide Wt%	core	core	core	core	core	core	core	rim	core	core	core	core	rim	rim	core	rim	core	core
SiO_2	47.3	46.0	46.8	45.6	46.5	47.6	46.8	46.8	51.0	51.6	52.1	49.7	45.8	46.2	48.1	46.2	47.3	48.6
TiO_2	2.5	2.9	3.4	3.0	2.9	2.8	2.9	2.7	1.2	1.3	1.1	1.9	3.7	3.3	2.5	3.4	2.8	1.8
Al_2O_3	4.5	5.7	5.5	5.0	5.1	5.2	5.7	5.1	2.5	2.3	2.2	3.3	7.1	6.3	4.4	6.4	5.0	3.5
FeO[t]	7.1	6.8	7.2	7.7	6.8	6.6	6.5	6.4	4.6	4.4	4.4	5.4	7.2	6.9	6.5	7.1	6.7	5.5
MnO	0.1	0.1	0.2	0.1	n.a.	n.a.	n.a.	0.1	n.d.	n.d.	n.d.	0.1	0.1	0.1	0.1	0.1	0.1	0.1
MgO	13.0	13.0	13.1	12.9	13.5	13.6	13.1	13.5	15.7	16.0	16.1	14.7	12.2	12.8	13.8	12.6	13.7	14.8
CaO	21.6	22.5	22.3	22.3	23.1	23.4	22.5	22.8	23.4	23.3	23.2	23.0	22.5	21.9	22.1	21.9	22.2	22.3
Na_2O	0.9	0.6	0.7	0.8	0.5	0.6	1.1	0.4	0.3	0.3	0.3	0.4	0.5	0.6	0.5	0.6	0.5	0.5
Cr_2O_3	n.d.	0.1	n.d.	n.d.	n.a.	n.a.	n.a.	0.6	0.5	0.5	0.6	0.6	n.d.	n.d.	0.6	0.1	0.1	0.9
SrO	n.a.	n.a.	n.a.	n.a.	n.d.	0.1	0.1	n.d.	n.d.	n.d.	n.d.	n.d.	n.d.	n.a.	n.a.	n.a.	n.a.	n.a.
NiO	n.d.	n.d.	n.d.	n.d.	n.a.	n.a.	n.a.	n.d.	n.d.	0.1	n.d.	n.d.	n.d.	0.1	n.d.	n.d.	n.d.	n.d.
Sum	96.9	97.6	99.3	97.4	98.5	99.7	98.6	98.3	99.3	99.6	100.1	99.0	99.2	98.2	98.6	96.5	98.3	98.0
FeO	3.82	2.79	3.73	1.99	2.09	2.34	1.40	3.27	2.39	3.19	3.44	3.80	5.12	4.48	4.44	4.73	3.80	2.33
Fe_2O_3	3.67	4.47	3.85	6.39	5.28	4.78	5.70	3.45	2.45	1.30	1.08	1.77	2.34	2.73	2.30	2.65	3.19	3.52
Total	97.30	98.09	99.66	98.02	98.99	100.18	99.21	98.61	99.50	99.77	100.17	99.19	99.46	98.52	98.83	98.78	98.65	98.33
T-site:																		
Si	1.844	1.795	1.792	1.811	1.810	1.818	1.810	1.808	1.914	1.916	1.923	1.876	1.745	1.775	1.834	1.769	1.817	1.871
Al	0.156	0.205	0.208	0.189	0.190	0.182	0.190	0.192	0.086	0.084	0.077	0.124	0.255	0.225	0.166	0.231	0.183	0.129
Fe^{3+}	0.000	0.000	0.000	0.000	0.000	0.000	0.000	0.000	0.000	0.000	0.000	0.000	0.000	0.000	0.000	0.000	0.000	0.000
M1-site:																		
Al	0.052	0.056	0.042	0.043	0.045	0.051	0.071	0.038	0.024	0.015	0.016	0.021	0.065	0.061	0.030	0.060	0.043	0.029
Fe^{3+}	0.108	0.131	0.111	0.191	0.155	0.137	0.166	0.100	0.069	0.036	0.030	0.050	0.067	0.079	0.066	0.076	0.092	0.102
Ti	0.072	0.086	0.098	0.089	0.084	0.079	0.085	0.079	0.033	0.036	0.032	0.054	0.106	0.095	0.073	0.099	0.080	0.051
Cr	0.001	0.004	0.001	0.001	0.000	0.000	0.000	0.019	0.016	0.014	0.017	0.018	0.001	0.001	0.018	0.003	0.002	0.027
Mg	0.756	0.723	0.748	0.676	0.716	0.732	0.679	0.763	0.858	0.884	0.886	0.826	0.691	0.733	0.785	0.721	0.782	0.790
Fe^{2+}	0.012	0.000	0.000	0.000	0.000	0.000	0.000	0.000	0.000	0.014	0.019	0.031	0.070	0.031	0.027	0.042	0.000	0.000
Mn	0.000	0.000	0.000	0.000	0.000	0.000	0.000	0.000	0.000	0.000	0.000	0.000	0.000	0.000	0.000	0.000	0.000	0.000
M2-site:																		
Mg	0.000	0.036	0.001	0.089	0.065	0.040	0.075	0.012	0.023	0.000	0.000	0.000	0.000	0.000	0.000	0.000	0.001	0.060
Fe^{2+}	0.113	0.091	0.119	0.066	0.068	0.075	0.045	0.106	0.075	0.085	0.087	0.089	0.093	0.113	0.114	0.110	0.122	0.075
Mn	0.004	0.003	0.005	0.004	0.000	0.000	0.000	0.002	0.001	0.001	0.001	0.002	0.004	0.004	0.003	0.004	0.003	0.005
Ca	0.901	0.940	0.914	0.949	0.963	0.956	0.931	0.942	0.942	0.925	0.917	0.929	0.917	0.901	0.903	0.901	0.915	0.921
Na	0.065	0.045	0.051	0.059	0.041	0.046	0.083	0.031	0.024	0.022	0.022	0.026	0.038	0.044	0.037	0.045	0.037	0.036
Sum M2:	1.083	1.114	1.091	1.166	1.137	1.118	1.134	1.094	1.065	1.033	1.027	1.046	1.053	1.062	1.058	1.060	1.078	1.096
EN%	39.93	39.43	39.48	38.73	39.74	39.80	39.75	40.25	44.75	45.43	45.68	42.86	37.50	39.38	41.35	38.89	40.91	43.55
WO%	47.58	48.85	48.13	48.05	48.95	49.27	49.12	48.93	47.88	47.56	47.25	48.20	49.78	48.43	47.56	48.59	47.75	47.14
FS%	12.49	11.72	12.39	13.22	11.31	10.93	11.13	10.82	7.37	7.01	7.06	8.95	12.72	12.18	11.09	12.52	11.34	9.31
Mg*	76.51	77.32	76.52	74.84	77.84	78.46	78.12	78.99	85.94	86.73	86.71	82.92	75.02	76.69	79.10	75.99	78.53	82.75

Appendix A: Microprobe Mineral Analyses
Pyroxenes

	5b-14	5b-15	5b-16	5b-18	5b-19	5b-20	5b-21	6b-2	6b-3	6b-4	6b-5	6b-6	6b-7	6b-11	6b-12	1b-156	1b-157	1b-158
	700 X 300 euhedral, slightly corroded phenocryst			*550 X 330 micron, diamond-shaped, subhedral, slightly corroded phenocryst*				*Subequant, corroded, fractured, euhedral microphenocryst*		Tepb2	*42 X 90 micron euhedral, corroded, fractured phenocryst*			*Subhedral, corroded, twinned micro*		*Gnd-mass micro*	*Gnd-mass micro*	*Gnd-mass micro*
Oxide Wt%	rim	core	core	rim	core	core	rim	core	core	rim	rim	core	rim	rim	core	core	core	core
SiO_2	46.9	50.3	51.4	45.6	51.6	51.4	45.9	48.0	49.3	45.0	45.5	50.6	45.4	46.6	47.2	50.6	46.0	50.7
TiO_2	2.5	1.5	1.4	3.5	1.3	1.2	3.4	2.0	0.9	3.4	3.4	1.2	3.3	3.0	3.0	1.3	3.0	1.0
Al_2O_3	5.3	3.0	2.4	6.3	2.3	2.3	6.1	4.7	4.6	6.8	6.7	2.9	6.4	5.7	6.2	2.5	5.5	2.5
FeO^t	6.7	5.9	7.1	7.2	4.7	4.4	7.4	6.2	5.2	7.1	6.8	4.7	6.9	6.8	6.8	5.1	7.2	4.9
MnO	0.1	0.1	0.2	n.d.	0.1	n.d.	0.1	0.1	0.1	0.1	0.1	0.1	0.1	0.1	0.1	0.1	0.1	0.1
MgO	13.8	15.4	13.9	12.5	16.0	16.1	12.8	14.4	14.9	12.6	12.5	15.5	12.8	13.3	13.1	15.7	12.9	15.6
CaO	22.0	22.0	21.9	22.3	22.2	22.5	22.2	22.4	22.8	22.8	22.4	22.9	22.8	23.0	23.0	23.0	22.7	22.9
Na_2O	0.5	0.4	0.8	0.6	0.4	0.4	0.5	0.4	0.4	0.5	0.7	0.4	0.6	0.5	0.5	0.4	0.5	0.4
Cr_2O_3	0.2	0.1	n.d.	n.d.	0.4	0.7	n.d.	0.5	0.2	n.d.	n.d.	0.8	n.d.	0.1	0.1	0.4	n.d.	0.7
SrO	n.a.	n.a.	n.a.	n.a.	n.a.	n.a.	n.a.	n.d.	n.d.	n.d.	n.d.	n.d.	n.d.	n.d.	n.d.	n.d.	n.d.	n.d.
NiO	0.1	0.1	n.d.	n.d.	n.d.	n.d.	n.d.	n.a.	n.a.	n.a.	n.a.	n.a.	n.a.	n.a.	n.a.	0.1	0.1	n.d.
Sum	98.1	98.8	99.0	98.1	99.0	99.0	98.5	98.7	98.5	98.4	98.2	99.2	98.3	99.0	100.0	99.0	97.9	98.8
FeO	3.18	3.88	6.33	3.97	3.93	3.02	4.28	2.74	1.96	2.56	3.18	2.44	2.51	2.97	3.86	2.46	3.42	2.53
Fe_2O_3	3.91	2.25	0.88	3.54	0.84	1.53	3.51	3.81	3.55	4.99	4.05	2.46	4.88	4.29	3.31	2.90	4.23	2.62
Total	98.47	99.02	99.11	98.41	99.11	99.15	98.85	99.11	98.81	98.86	98.56	99.41	98.75	99.43	100.37	99.32	98.32	99.09
T-site:																		
Si	1.815	1.898	1.926	1.768	1.920	1.920	1.773	1.839	1.877	1.755	1.765	1.902	1.770	1.793	1.787	1.910	1.794	1.917
Al	0.185	0.102	0.074	0.232	0.080	0.080	0.227	0.161	0.123	0.245	0.235	0.098	0.230	0.207	0.213	0.090	0.206	0.083
Fe^{3+}	0.000	0.000	0.000	0.000	0.000	0.000	0.000	0.000	0.000	0.000	0.000	0.000	0.000	0.000	0.000	0.000	0.000	0.000
M1-site:																		
Al	0.058	0.030	0.030	0.055	0.019	0.020	0.052	0.053	0.084	0.068	0.068	0.031	0.063	0.052	0.064	0.020	0.048	0.027
Fe^{3+}	0.114	0.064	0.025	0.103	0.023	0.043	0.102	0.110	0.102	0.147	0.118	0.070	0.143	0.124	0.094	0.082	0.124	0.075
Ti	0.072	0.044	0.040	0.102	0.035	0.032	0.098	0.058	0.026	0.100	0.099	0.035	0.096	0.086	0.085	0.038	0.088	0.029
Cr	0.006	0.004	0.001	0.001	0.013	0.020	0.001	0.014	0.007	0.001	0.000	0.025	0.000	0.002	0.002	0.013	0.001	0.021
Mg	0.750	0.859	0.774	0.724	0.890	0.885	0.736	0.765	0.781	0.685	0.714	0.839	0.697	0.735	0.740	0.847	0.738	0.848
Fe^{2+}	0.000	0.000	0.131	0.015	0.020	0.000	0.010	0.000	0.000	0.000	0.000	0.000	0.000	0.000	0.014	0.000	0.000	0.000
Mn	0.000	0.000	0.000	0.000	0.000	0.000	0.000	0.000	0.000	0.000	0.000	0.000	0.000	0.000	0.000	0.000	0.000	0.000
M2-site:																		
Mg	0.045	0.007	0.000	0.000	0.000	0.013	0.000	0.057	0.064	0.049	0.008	0.029	0.047	0.030	0.000	0.039	0.013	0.032
Fe^{2+}	0.103	0.122	0.068	0.114	0.102	0.094	0.128	0.088	0.062	0.084	0.103	0.077	0.082	0.096	0.109	0.078	0.112	0.080
Mn	0.004	0.003	0.005	0.001	0.005	0.001	0.004	0.003	0.004	0.004	0.003	0.003	0.002	0.002	0.002	0.002	0.004	0.003
Ca	0.911	0.891	0.878	0.924	0.884	0.902	0.917	0.921	0.928	0.952	0.930	0.925	0.950	0.948	0.930	0.931	0.947	0.928
Na	0.037	0.030	0.055	0.046	0.027	0.029	0.038	0.032	0.031	0.041	0.053	0.032	0.044	0.034	0.039	0.026	0.034	0.027
Sum M2:	1.100	1.053	1.006	1.085	1.018	1.039	1.087	1.101	1.091	1.129	1.097	1.065	1.124	1.110	1.079	1.076	1.110	1.071
EN%	41.27	44.48	41.16	38.49	46.23	46.33	38.80	42.28	43.53	38.24	38.50	44.72	38.73	39.55	39.19	44.74	38.79	44.78
WO%	47.29	45.79	46.69	49.11	45.96	46.53	48.34	47.40	47.80	49.58	49.54	47.61	49.45	48.99	49.26	47.06	48.86	47.22
FS%	11.44	9.74	12.15	12.39	7.81	7.15	12.87	10.32	8.67	12.18	11.96	7.67	11.82	11.47	11.55	8.21	12.35	8.00
Mg*	78.61	82.29	77.63	75.74	85.92	86.72	75.39	80.60	83.74	76.14	76.55	85.58	76.80	77.68	77.37	84.70	76.13	85.06

Appendix A: Microprobe Mineral Analyses
Pyroxenes

	6b-14	6b-15	6b-16	6b-17	6b-18	8c1-2	8c1-3	8c1-4	1b-159	1b-166	1b-167	1b-168	1b-169	1b-170	1b-171	1b-172	1b-173	1b-174
	150 X 100 micron, tabular, formerly euhedral, severely corroded with row of opaques across grain, phenocryst					*525 micron wide phenocryst*			Tepb2									
Oxide Wt%	rim	core	core	core	rim	rim	core	rim	*Gnd-mass micro* core	*Gnd-mass micro* core	*Gnd-mass micro* core	*Gnd-mass micro* core	*Gnd-mass micro* core	*Gnd-mass micro* core	*Gnd-mass micro* core	*Gnd-mass micro* core	*Gnd-mass micro* core	*Gnd-mass micro* core
SiO_2	48.6	51.6	49.8	50.4	47.9	50.2	52.2	46.8	48.1	46.9	45.9	46.0	47.2	45.5	47.7	48.0	43.0	46.1
TiO_2	2.3	0.8	1.7	1.3	2.3	1.8	1.1	3.0	2.3	2.8	3.6	3.4	3.0	3.2	2.4	2.6	4.3	3.2
Al_2O_3	4.2	2.3	3.8	3.1	4.7	2.8	2.0	5.4	4.7	5.0	6.2	6.0	5.5	6.1	4.3	4.3	8.0	5.8
FeO^t	7.3	4.8	5.8	4.7	6.9	5.1	4.1	6.6	6.8	7.8	7.5	7.4	7.1	7.6	6.6	6.9	8.5	7.2
MnO	0.1	0.1	0.1	n.d.	0.2	0.1	0.1	0.1	0.1	0.1	0.1	0.1	0.1	0.1	0.1	0.1	0.1	0.1
MgO	13.4	16.1	14.5	15.6	14.3	15.2	16.4	13.3	13.3	13.2	12.5	12.7	13.3	12.3	13.7	13.5	11.6	12.7
CaO	22.2	22.0	22.9	22.5	21.6	22.4	22.6	22.4	22.5	22.4	22.5	22.7	22.7	22.6	22.7	22.8	22.1	22.8
Na_2O	0.8	0.6	0.6	0.4	0.6	0.4	0.4	0.5	0.5	0.5	0.5	0.5	0.5	0.4	0.4	0.4	0.5	0.4
Cr_2O_3	0.1	0.9	0.6	1.0	n.d.	0.3	0.7	0.1	0.6	n.d.	n.d.	n.d.	0.2	0.1	n.d.	n.d.	0.1	n.d.
SrO	n.d.	n.d.	n.d.	n.d.	n.d.	n.a.	n.a.	n.a.	n.d.	n.d.	n.d.	n.d.	n.d.	n.a.	n.a.	n.a.	n.a.	n.a.
NiO	n.a.	n.a.	n.a.	n.a.	n.a.	0.1	n.d.	0.1	n.d.	n.d.	n.d.	n.d.	n.d.	n.d.	n.d.	n.d.	n.d.	n.d.
Sum	99.0	99.2	99.7	99.1	98.5	98.4	99.4	98.2	98.9	98.8	98.7	98.8	99.6	97.9	98.1	98.6	98.0	98.4
FeO	3.93	2.57	3.29	2.72	2.97	3.74	3.40	3.92	4.97	4.28	4.44	4.14	4.00	4.18	3.56	4.29	3.97	4.10
Fe_2O_3	3.77	2.51	2.77	2.23	4.36	1.55	0.77	2.94	2.04	3.95	3.45	3.66	3.42	3.81	3.39	2.90	4.98	3.44
Total	99.38	99.44	99.93	99.29	98.95	98.51	99.52	98.47	99.10	99.19	99.09	99.22	99.96	98.25	98.46	98.89	98.49	98.71
T-site:																		
Si	1.859	1.932	1.874	1.894	1.841	1.894	1.930	1.801	1.833	1.813	1.768	1.775	1.799	1.775	1.841	1.838	1.697	1.784
Al	0.141	0.068	0.126	0.106	0.159	0.106	0.070	0.199	0.167	0.187	0.232	0.225	0.201	0.225	0.159	0.162	0.303	0.216
Fe^{3+}	0.000	0.000	0.000	0.000	0.000	0.000	0.000	0.000	0.000	0.000	0.000	0.000	0.000	0.000	0.000	0.000	0.000	0.000
M1-site:																		
Al	0.046	0.033	0.042	0.032	0.054	0.020	0.015	0.045	0.044	0.043	0.049	0.047	0.045	0.056	0.037	0.032	0.068	0.049
Fe^{3+}	0.108	0.071	0.078	0.063	0.126	0.044	0.021	0.085	0.058	0.115	0.100	0.106	0.098	0.112	0.098	0.084	0.148	0.100
Ti	0.066	0.021	0.049	0.037	0.066	0.050	0.030	0.087	0.066	0.082	0.103	0.098	0.086	0.093	0.070	0.074	0.127	0.092
Cr	0.002	0.027	0.018	0.029	0.001	0.010	0.020	0.004	0.018	0.000	0.001	0.001	0.007	0.003	0.001	0.001	0.003	0.001
Mg	0.764	0.848	0.812	0.839	0.752	0.855	0.905	0.762	0.752	0.757	0.716	0.730	0.756	0.718	0.789	0.771	0.654	0.731
Fe^{2+}	0.014	0.000	0.002	0.000	0.000	0.021	0.010	0.017	0.062	0.003	0.032	0.018	0.008	0.019	0.004	0.039	0.000	0.026
Mn	0.000	0.000	0.000	0.000	0.000	0.000	0.000	0.000	0.000	0.000	0.000	0.000	0.000	0.000	0.000	0.000	0.000	0.000
M2-site:																		
Mg	0.000	0.054	0.000	0.037	0.067	0.000	0.000	0.000	0.000	0.000	0.000	0.000	0.000	0.000	0.000	0.000	0.027	0.000
Fe^{2+}	0.112	0.081	0.102	0.085	0.096	0.097	0.095	0.109	0.097	0.135	0.111	0.116	0.120	0.117	0.111	0.099	0.131	0.106
Mn	0.004	0.003	0.003	0.001	0.006	0.003	0.002	0.003	0.003	0.003	0.003	0.004	0.004	0.005	0.004	0.004	0.003	0.003
Ca	0.910	0.885	0.923	0.906	0.889	0.904	0.895	0.923	0.918	0.928	0.929	0.938	0.927	0.945	0.938	0.936	0.934	0.946
Na	0.060	0.041	0.041	0.031	0.048	0.032	0.026	0.037	0.034	0.034	0.041	0.034	0.035	0.032	0.032	0.032	0.037	0.032
Sum M2:	1.086	1.064	1.069	1.061	1.107	1.036	1.019	1.072	1.052	1.100	1.084	1.092	1.086	1.099	1.085	1.071	1.133	1.087
EN%	39.96	46.47	42.27	45.33	42.31	44.46	46.91	40.13	39.79	38.99	37.86	38.16	39.53	37.45	40.60	39.90	35.91	38.23
WO%	47.59	45.59	48.07	46.92	45.91	46.98	46.42	48.61	48.59	47.80	49.12	49.09	48.48	49.33	48.25	48.46	49.21	49.45
FS%	12.45	7.95	9.66	7.75	11.78	8.56	6.67	11.27	11.62	13.21	13.02	12.76	11.99	13.22	11.15	11.64	14.88	12.32
Mg*	76.55	85.64	81.68	85.50	78.71	84.08	87.73	78.30	77.62	74.94	74.65	75.26	77.04	74.27	78.73	77.71	70.95	75.87

Appendix A: Microprobe Mineral Analyses
Pyroxenes

	1b-175	5b-2	5b-3	5b-8	5b-13	5b-22	5b-54	6b-8	6b-10	6b-19	6b-20	6b-21	6b-22	8c1-5	8c1-6	8c1-7	1b-150	1b-151
									Tepb2								Tepbv	
Oxide Wt%	*Gnd-mass micro* core	*Gnd-mass micro* core	*Gnd-mass micro* core	*Gnd-mass micro* core	*Gnd-mass micro* core	*Gnd-mass micro* core	*Gnd-mass micro* core	*Gnd-mass micro* core	*Gnd-mass micro* core	*Gnd-mass micro* core	*Gnd-mass micro* core	*Gnd-mass micro* core	*Gnd-mass micro* core	*Gnd-mass micro* core	*Gnd-mass micro* core	*Gnd-mass micro* core	*140 micron phens* core	*Skele-tal micro* core
SiO_2	45.9	48.5	45.2	47.1	47.2	46.5	46.3	45.7	45.9	49.9	46.5	46.0	49.3	44.2	46.8	45.6	47.4	49.7
TiO_2	3.3	2.2	3.6	2.9	2.7	3.2	n.a.	3.4	3.1	2.1	3.1	3.1	2.1	4.2	3.1	3.4	2.6	2.1
Al_2O_3	6.2	3.4	6.5	4.9	5.0	5.8	5.6	6.5	5.9	3.4	5.7	6.2	4.2	7.2	5.3	6.2	4.7	3.6
FeO^t	7.6	6.6	7.4	7.8	7.1	7.1	7.4	7.4	6.7	6.7	7.3	7.3	6.2	8.0	7.4	7.0	9.9	9.4
MnO	0.1	0.1	0.1	0.2	0.1	0.1	0.1	0.1	0.1	0.1	0.2	0.1	0.1	0.1	0.1	0.1	0.2	0.3
MgO	12.6	14.5	12.1	13.3	13.3	12.7	12.4	12.8	13.1	14.0	13.0	12.8	14.2	11.9	13.0	12.5	11.2	11.9
CaO	22.5	22.3	22.1	22.0	22.0	22.4	22.1	22.7	22.9	22.0	22.8	22.7	23.0	22.1	22.4	22.1	21.9	21.9
Na_2O	0.5	0.5	0.7	0.6	0.6	0.6	n.a.	0.6	0.6	0.9	0.6	0.6	0.5	0.6	0.5	0.6	0.9	0.9
Cr_2O_3	n.d.	0.1	n.d.	n.d.	0.1	0.1	n.d.	n.d.	0.2	n.d.	0.1	0.1	0.5	n.d.	n.d.	n.d.	n.d.	n.d.
SrO	n.a.	n.a.	n.a.	n.a.	n.a.	n.a.	n.a.	n.d.	n.d.	n.d.	n.d.	n.d.	n.d.	n.a.	n.a.	n.a.	n.d.	n.d.
NiO	n.d.	n.d.	n.d.	0.1	n.d.	n.d.	n.d.	n.a.	n.a.	n.a.	n.a.	n.a.	n.a.	n.d.	n.d.	0.1	n.d.	n.d.
Sum	98.7	98.3	97.8	98.7	98.0	98.4	93.9	99.2	98.2	99.1	99.2	98.8	100.0	98.3	98.7	97.6	98.8	99.7
FeO	4.28	3.27	3.91	4.22	4.30	4.22	4.78	3.11	2.42	4.18	3.16	3.08	3.66	4.22	4.23	4.02	6.91	7.67
Fe_2O_3	3.74	3.74	3.86	4.01	3.07	3.19	2.89	4.75	4.72	2.81	4.58	4.66	2.79	4.24	3.47	3.33	3.37	1.87
Total	99.07	98.63	98.17	99.11	98.30	98.72	94.23	99.64	98.72	99.43	99.65	99.27	100.29	98.74	99.00	97.96	99.16	99.89
T-site:																		
Si	1.774	1.868	1.761	1.817	1.819	1.789	1.866	1.766	1.784	1.885	1.793	1.782	1.855	1.724	1.802	1.772	1.837	1.880
Al	0.226	0.132	0.239	0.183	0.181	0.211	0.134	0.234	0.216	0.115	0.207	0.218	0.145	0.276	0.198	0.228	0.163	0.120
Fe^{3+}	0.000	0.000	0.000	0.000	0.000	0.000	0.000	0.000	0.000	0.000	0.000	0.000	0.000	0.000	0.000	0.000	0.000	0.000
M1-site:																		
Al	0.055	0.022	0.059	0.039	0.046	0.053	0.131	0.063	0.055	0.038	0.051	0.063	0.039	0.055	0.043	0.057	0.050	0.042
Fe^{3+}	0.109	0.108	0.113	0.117	0.089	0.092	0.088	0.138	0.138	0.080	0.133	0.136	0.079	0.125	0.100	0.097	0.098	0.053
Ti	0.095	0.064	0.105	0.084	0.080	0.091	0.000	0.098	0.091	0.059	0.090	0.090	0.059	0.124	0.089	0.099	0.076	0.059
Cr	0.001	0.003	0.001	0.001	0.002	0.003	0.001	0.001	0.005	0.001	0.002	0.003	0.016	0.001	0.001	0.001	0.000	0.001
Mg	0.723	0.803	0.705	0.759	0.763	0.731	0.745	0.700	0.711	0.788	0.724	0.709	0.794	0.691	0.747	0.723	0.644	0.672
Fe^{2+}	0.016	0.000	0.016	0.000	0.021	0.030	0.035	0.000	0.000	0.035	0.000	0.000	0.013	0.005	0.020	0.022	0.131	0.173
Mn	0.000	0.000	0.000	0.000	0.000	0.000	0.000	0.000	0.000	0.000	0.000	0.000	0.000	0.000	0.000	0.000	0.000	0.000
M2-site:																		
Mg	0.000	0.029	0.000	0.006	0.000	0.000	0.000	0.035	0.046	0.000	0.022	0.028	0.000	0.000	0.000	0.000	0.000	0.000
Fe^{2+}	0.122	0.105	0.112	0.136	0.118	0.106	0.126	0.100	0.079	0.097	0.102	0.100	0.102	0.133	0.117	0.108	0.093	0.070
Mn	0.004	0.004	0.005	0.005	0.004	0.003	0.005	0.003	0.002	0.004	0.005	0.003	0.002	0.003	0.004	0.005	0.008	0.010
Ca	0.932	0.921	0.924	0.910	0.908	0.924	0.955	0.938	0.954	0.892	0.943	0.941	0.928	0.926	0.926	0.921	0.910	0.888
Na	0.036	0.035	0.053	0.042	0.043	0.043	0.000	0.043	0.042	0.064	0.043	0.046	0.037	0.045	0.039	0.046	0.064	0.063
Sum M2:	1.094	1.094	1.093	1.099	1.073	1.076	1.085	1.120	1.122	1.057	1.115	1.118	1.070	1.106	1.085	1.080	1.074	1.031
EN%	37.94	42.21	37.64	39.57	40.08	38.74	38.16	38.38	39.25	41.56	38.70	38.43	41.39	36.72	39.04	38.53	34.20	36.02
WO%	48.90	46.75	49.27	47.07	47.73	48.98	48.87	49.00	49.42	47.04	48.88	49.10	48.38	49.20	48.40	49.06	48.28	47.57
FS%	13.17	11.04	13.09	13.36	12.20	12.28	12.97	12.62	11.33	11.40	12.42	12.47	10.24	14.08	12.56	12.40	17.51	16.41
Mg*	74.53	79.57	74.58	75.16	77.01	76.20	74.98	75.52	77.74	78.82	76.10	75.76	80.37	72.49	75.94	76.03	66.67	69.40

Appendix A: Microprobe Mineral Analyses
Pyroxenes

	1b-141	1b-142	1b-143	1b-144	1b-145	1b-109	1b-146	1b-147	1b-148	1b-149	1b-153	1b-154	1b-155	5b-23	5b-24	5b-25	5b-26	5b-31
	2 X 2.5 mm euhedral, corroded, sector-zoned phenocryst with multiphase core consisting of cpx, K-spar, & nepheline									Tephv	*3.8 (including whiskers) X 1.2 mm skeletal phenocryst growing from wall*			*2.5 X 1.4 mm tabular, moderately corroded, fractured phenocryst*				*Cor-roded micro*
Oxide Wt%	spur	rim	core	core	core	core	core	core	core	rim	spur	spur	core	rim	core	core	core	core
SiO_2	48.5	45.9	43.6	42.0	45.5	44.9	47.0	44.4	42.6	43.7	45.4	44.2	42.5	43.2	43.5	44.3	43.4	43.7
TiO_2	2.3	3.6	4.4	5.2	3.5	3.4	3.2	4.0	5.0	4.7	3.4	4.6	5.2	4.4	4.9	4.5	4.9	4.5
Al_2O_3	5.0	6.6	8.3	9.2	7.0	6.8	5.4	7.5	8.3	8.2	7.5	8.4	9.1	8.6	8.3	7.7	8.3	7.9
FeO^t	7.9	8.7	7.8	7.9	7.2	7.2	7.1	7.5	7.9	7.8	8.4	8.2	8.0	7.4	7.4	7.4	7.4	7.3
MnO	0.2	0.2	0.2	0.1	0.1	n.a.	0.2	0.1	0.2	0.2	0.2	0.2	0.1	0.2	0.1	0.1	0.1	0.1
MgO	12.2	11.0	11.0	10.7	12.1	12.2	12.7	11.6	11.0	11.0	10.9	10.8	11.0	10.4	11.1	11.8	11.4	11.8
CaO	22.7	22.0	22.3	22.1	22.4	22.7	22.5	22.8	22.4	22.3	22.2	22.2	22.3	21.7	21.9	22.2	22.0	22.1
Na_2O	0.7	0.7	0.7	0.7	0.6	0.6	0.5	0.6	0.6	0.7	0.7	0.8	0.7	0.9	0.8	0.8	0.7	0.7
Cr_2O_3	n.d.	n.d.	n.d.	n.d.	n.d.	n.d.	n.d.	n.d.	n.d.	n.d.	n.d.	n.d.	n.d.	n.e.	n.d.	n.d.	n.d.	n.d.
SrO	n.d.	n.d.	n.d.	n.d.	n.d.	n.d.	n.d.	n.d.	n.d.	n.d.	n.d.	n.d.	n.d.	n.a.	n.a.	n.a.	n.a.	n.a.
NiO	n.d.	n.d.	n.d.	n.d.	n.d.	n.a.	0.1	n.d.	n.d.	n.d.	0.1	n.d.	n.d.	0.1	n.d.	n.d.	n.d.	n.d.
Sum	99.4	98.8	98.1	97.9	98.5	97.8	98.6	98.6	98.2	98.7	98.8	99.3	99.0	96.8	98.0	98.7	98.3	98.0
FeO	5.76	6.80	4.70	4.23	4.35	3.27	5.04	3.73	3.91	4.92	5.79	5.55	4.13	5.05	5.02	4.12	4.36	3.86
Fe_2O_3	2.40	2.14	3.48	4.11	3.16	4.37	2.27	4.24	4.42	3.24	2.94	2.94	4.32	2.59	2.63	3.62	3.35	3.78
Total	99.66	99.02	98.49	98.30	98.78	98.27	98.80	99.04	98.62	99.00	99.06	99.60	99.42	97.07	98.28	99.11	98.60	98.36
T-site:																		
Si	1.840	1.761	1.697	1.650	1.755	1.756	1.798	1.723	1.674	1.692	1.749	1.696	1.654	1.693	1.685	1.710	1.682	1.703
Al	0.160	0.239	0.303	0.350	0.245	0.244	0.202	0.277	0.326	0.308	0.251	0.304	0.346	0.307	0.315	0.290	0.318	0.297
Fe^{3+}	0.000	0.000	0.000	0.000	0.000	0.000	0.000	0.000	0.000	0.000	0.000	0.000	0.000	0.000	0.000	0.000	0.000	0.000
M1-site:																		
Al	0.062	0.060	0.077	0.076	0.071	0.069	0.043	0.069	0.060	0.067	0.087	0.075	0.069	0.090	0.065	0.061	0.063	0.065
Fe^{3+}	0.069	0.062	0.102	0.122	0.092	0.129	0.066	0.124	0.131	0.094	0.085	0.085	0.126	0.076	0.077	0.105	0.098	0.111
Ti	0.065	0.105	0.128	0.152	0.100	0.100	0.091	0.118	0.148	0.137	0.099	0.132	0.153	0.131	0.143	0.131	0.144	0.131
Cr	0.000	0.000	0.000	0.001	0.000	0.000	0.000	0.000	0.000	0.000	0.000	0.001	0.000	0.000	0.000	0.000	0.001	0.001
Mg	0.693	0.632	0.639	0.625	0.697	0.702	0.724	0.674	0.645	0.634	0.626	0.616	0.638	0.605	0.640	0.677	0.659	0.682
Fe^{2+}	0.112	0.140	0.054	0.025	0.039	0.000	0.077	0.016	0.017	0.068	0.103	0.091	0.013	0.099	0.075	0.025	0.036	0.011
Mn	0.000	0.000	0.000	0.000	0.000	0.000	0.000	0.000	0.000	0.000	0.000	0.000	0.000	0.000	0.000	0.000	0.000	0.000
M2-site:																		
Mg	0.000	0.000	0.000	0.000	0.000	0.010	0.000	0.000	0.000	0.000	0.000	0.000	0.000	0.000	0.000	0.000	0.000	0.000
Fe^{2+}	0.071	0.078	0.099	0.114	0.101	0.107	0.085	0.105	0.112	0.091	0.084	0.087	0.121	0.067	0.087	0.108	0.106	0.115
Mn	0.007	0.007	0.006	0.004	0.004	0.000	0.006	0.003	0.006	0.006	0.008	0.007	0.004	0.006	0.004	0.003	0.003	0.004
Ca	0.922	0.907	0.929	0.931	0.926	0.952	0.924	0.949	0.943	0.926	0.918	0.912	0.931	0.910	0.906	0.916	0.914	0.921
Na	0.050	0.051	0.050	0.052	0.044	0.042	0.037	0.047	0.049	0.052	0.055	0.058	0.049	0.069	0.057	0.056	0.055	0.051
Sum M2:	1.050	1.043	1.083	1.101	1.074	1.111	1.051	1.105	1.110	1.074	1.065	1.064	1.106	1.051	1.055	1.083	1.077	1.091
EN%	37.00	34.63	34.94	34.32	37.51	37.49	38.51	36.01	34.81	34.85	34.31	34.27	34.78	34.31	35.77	36.89	36.30	37.01
WO%	49.22	49.66	50.80	51.16	49.80	50.12	49.13	50.73	50.91	50.91	50.35	50.73	50.76	51.61	50.65	49.96	50.36	49.93
FS%	13.79	15.71	14.27	14.52	12.69	12.39	12.36	13.25	14.28	14.24	15.34	15.00	14.46	14.08	13.58	13.15	13.35	13.06
Mg*	73.37	69.29	71.46	70.57	75.04	75.16	76.15	73.33	71.35	71.44	69.71	70.10	70.98	71.45	72.83	73.97	73.35	74.27

Appendix A: Microprobe Mineral Analyses
Pyroxenes

	5b-33	5b-34	5b-36	21.1-4	21.1-5	21.1-6	21.1-7	21.1-8	21.1-9	21.1-10	21.1-11	21.1-13	21.1-14	21.1-15	21.1-17	21.1-18	21.1-19	21.1-21
	750 micron wide subhedral microphenocryst with heavily corroded margins			Tepbv *600 micron wide, boot-shaped, sector-zoned phenoryst growing from wall rock*														
Oxide Wt%	rim	core	rim	rim	rim	core	core	core	core	core	core	core	core	core	rim	rim	rim	core
SiO_2	44.3	47.6	43.0	42.7	42.1	48.6	48.5	47.8	48.2	48.4	48.4	48.3	48.4	47.9	43.0	44.4	42.8	47.2
TiO_2	4.5	2.8	4.3	5.3	5.5	2.7	2.8	2.8	2.8	2.6	2.8	2.8	2.9	2.9	5.7	4.4	5.4	2.7
Al_2O_3	7.8	5.1	7.7	10.3	9.5	4.8	5.0	5.2	5.2	6.9	5.3	5.2	5.3	5.3	9.7	8.6	9.5	5.2
FeO^t	7.3	6.8	10.6	7.9	8.2	7.3	7.4	7.6	7.5	7.0	7.4	7.1	7.7	7.9	8.7	8.7	8.4	6.9
MnO	0.2	0.1	0.2	0.2	0.2	0.2	0.2	0.1	0.2	0.2	0.2	0.2	0.2	0.2	0.2	0.2	0.2	0.1
MgO	11.3	13.2	10.6	9.7	10.2	12.9	12.7	12.9	12.8	11.6	12.5	12.8	12.5	12.4	9.9	10.1	10.0	13.2
CaO	21.7	21.8	20.7	21.3	22.0	22.1	22.1	22.4	22.2	20.3	22.1	22.4	22.2	22.2	22.1	21.5	21.9	22.1
Na_2O	0.7	0.6	0.8	0.8	0.7	0.5	0.6	0.6	0.6	1.5	0.6	0.6	0.6	0.6	0.8	0.8	0.7	0.5
Cr_2O_3	n.d.	n.d.	n.d.	n.d.	n.d.	n.d.	n.d.	n.d.	n.d.	n.d.	n.d.	n.d.	n.d.	n.d.	n.d.	n.d.	n.d.	n.d.
SrO	n.a.	n.a.	n.a.	n.d.	n.d.	n.d.	n.d.	n.d.	n.d.	n.d.	n.d.	n.d.	n.d.	n.d.	n.d.	n.d.	n.d.	n.d.
NiO	n.d.	n.d.	n.d.	0.1	n.d.	n.d.	n.d.	n.d.	n.d.	n.d.	n.d.	n.d.	n.d.	0.1	n.d.	n.d.	n.d.	0.1
Sum	97.9	98.2	97.9	98.1	98.5	99.2	99.3	99.3	99.6	98.6	99.3	99.5	99.9	99.5	100.0	98.7	99.0	98.1
FeO	5.46	4.97	5.78	7.60	5.41	6.58	6.60	5.34	6.01	6.29	6.93	5.85	6.63	6.20	6.81	7.61	6.39	4.56
Fe_2O_3	2.10	2.08	5.37	0.32	3.11	0.76	0.87	2.47	1.66	0.82	0.48	1.44	1.21	1.85	2.07	1.18	2.25	2.65
Total	98.07	98.37	98.43	98.11	98.81	99.30	99.39	99.58	99.74	98.67	99.35	99.59	100.05	99.64	100.19	98.77	99.26	98.35
T-site:																		
Si	1.710	1.818	1.709	1.634	1.638	1.828	1.823	1.816	1.818	1.811	1.817	1.818	1.816	1.814	1.639	1.698	1.646	1.815
Al	0.290	0.182	0.291	0.366	0.362	0.172	0.177	0.184	0.182	0.189	0.183	0.182	0.184	0.186	0.361	0.302	0.354	0.185
Fe^{3+}	0.000	0.000	0.000	0.000	0.000	0.000	0.000	0.000	0.000	0.000	0.000	0.000	0.000	0.000	0.000	0.000	0.000	0.000
M1-site:																		
Al	0.064	0.050	0.071	0.098	0.072	0.043	0.046	0.047	0.050	0.117	0.053	0.051	0.051	0.051	0.072	0.087	0.077	0.049
Fe^{3+}	0.061	0.060	0.161	0.009	0.091	0.021	0.025	0.071	0.047	0.023	0.014	0.041	0.034	0.053	0.059	0.034	0.065	0.077
Ti	0.130	0.080	0.129	0.152	0.162	0.077	0.079	0.081	0.080	0.072	0.079	0.079	0.081	0.082	0.163	0.126	0.156	0.079
Cr	0.000	0.001	0.000	0.000	0.001	0.001	0.000	0.001	0.000	0.000	0.000	0.000	0.000	0.000	0.000	0.001	0.000	0.001
Mg	0.651	0.751	0.629	0.552	0.591	0.723	0.712	0.728	0.719	0.646	0.697	0.719	0.700	0.699	0.560	0.575	0.575	0.757
Fe^{2+}	0.094	0.058	0.010	0.188	0.083	0.135	0.138	0.073	0.104	0.142	0.157	0.110	0.134	0.116	0.145	0.177	0.126	0.037
Mn	0.000	0.000	0.000	0.000	0.000	0.000	0.000	0.000	0.000	0.000	0.000	0.000	0.000	0.000	0.000	0.000	0.000	0.000
M2-site:																		
Mg	0.000	0.000	0.000	0.000	0.000	0.000	0.000	0.000	0.000	0.000	0.000	0.000	0.000	0.000	0.000	0.000	0.000	0.000
Fe^{2+}	0.082	0.101	0.182	0.055	0.092	0.072	0.070	0.097	0.085	0.055	0.061	0.074	0.074	0.081	0.072	0.066	0.080	0.110
Mn	0.005	0.005	0.006	0.006	0.005	0.006	0.007	0.005	0.006	0.006	0.006	0.005	0.006	0.008	0.006	0.006	0.006	0.005
Ca	0.897	0.893	0.883	0.874	0.916	0.890	0.892	0.913	0.897	0.815	0.890	0.903	0.893	0.901	0.900	0.884	0.903	0.909
Na	0.056	0.045	0.064	0.056	0.056	0.040	0.042	0.041	0.043	0.109	0.043	0.043	0.045	0.046	0.060	0.058	0.056	0.039
Sum M2:	1.041	1.043	1.135	0.990	1.070	1.008	1.010	1.055	1.031	0.986	0.999	1.025	1.018	1.036	1.038	1.014	1.045	1.062
EN%	36.34	40.24	33.62	32.77	33.21	39.12	38.65	38.60	38.69	38.29	38.24	38.82	38.01	37.63	32.13	32.98	32.78	39.98
WO%	50.11	47.81	47.18	51.90	51.49	48.18	48.38	48.42	48.27	48.33	48.79	48.76	48.49	48.54	51.68	50.71	51.44	47.99
FS%	13.55	11.95	19.20	15.34	15.30	12.70	12.96	12.98	13.03	13.38	12.97	12.42	13.49	13.83	16.19	16.30	15.77	12.03
Mg*	73.28	77.46	64.04	68.61	68.89	75.99	75.40	75.20	75.26	74.63	75.12	76.17	74.31	73.72	66.97	67.43	68.01	77.23

Appendix A: Microprobe Mineral Analyses
Pyroxenes

	21.1-22	21.1-24	21.1-25	21.1-26	21.1-27	5b-28	5b-29	5b-30	5b-39	5b-40	5b-41	8c1-8	8c1-9	8c1-10	21.1-28	21.1-29	21.1-30
			500 X 950 subhedral phenoryst			120 micron long micropheno			Tepbv Green, interstitial, 150 X 50 microns microphenocryst			Green, subhedral, tabular groundmass pheno, 270 X 135 microns			Green, anhedral, L-shaped groundmass micropheno		
Oxide Wt%	core	core	core	rim	rim	rim	core	rim	rim	core	rim	rim	core	rim	limb	center	limb
SiO_2	47.2	44.6	43.2	42.8	43.2	43.9	49.2	47.1	51.3	50.3	50.0	51.0	50.6	50.9	49.2	50.3	49.5
TiO_2	2.8	3.9	4.8	5.1	5.0	4.1	2.1	2.6	1.5	1.6	1.7	0.9	1.1	0.7	1.2	1.2	1.5
Al_2O_3	5.4	7.1	8.5	9.2	9.2	8.0	3.9	5.6	1.7	1.9	2.0	1.4	1.4	1.4	1.6	1.6	2.1
FeO^t	6.8	7.6	7.5	8.1	8.5	7.4	7.4	7.4	12.4	12.4	12.3	12.8	12.0	13.1	15.3	15.2	15.2
MnO	0.2	0.2	0.1	0.1	0.2	0.3	0.3	0.3	0.4	0.4	0.4	0.5	0.6	0.6	0.4	0.4	0.4
MgO	13.3	12.0	11.2	10.5	10.1	9.8	12.3	11.3	10.5	10.3	10.3	10.0	10.7	9.5	8.3	8.4	8.4
CaO	22.1	22.0	22.3	22.0	21.9	20.7	21.7	21.2	20.8	20.7	20.7	20.2	20.2	20.0	21.7	20.8	20.6
Na_2O	0.5	0.6	0.6	0.7	0.8	1.0	0.8	0.9	1.2	1.1	1.2	1.7	1.6	1.8	0.8	0.8	1.0
Cr_2O_3	n.d.	n.d.	n.d.	n.d.	n.d.	n.d.	n.d.	n.d.	n.d.	n.d.	n.d.	n.d.	n.d.	n.d.	n.d.	n.d.	n.d.
SrO	n.d.	n.d.	n.d.	n.d.	n.d.	n.a.	n.a.	n.a.	n.a.	n.a.	n.a.	n.a.	n.a.	n.a.	n.d.	n.d.	n.d.
NiO	n.d.	n.d.	n.d.	n.d.	n.d.	n.d.	n.d.	0.1	n.d.	n.d.	n.d.	n.d.	n.d.	0.1	0.1	n.d.	n.d.
Sum	98.3	98.1	98.4	98.4	99.0	95.3	97.6	96.4	99.8	98.8	98.7	98.4	98.2	98.2	98.4	98.8	98.6
FeO	4.24	4.47	4.37	5.47	6.35	7.19	7.12	6.73	11.38	11.24	10.35	9.87	8.60	9.79	12.90	15.33	14.35
Fe_2O_3	2.89	3.52	3.50	2.90	2.44	0.21	0.29	0.72	1.17	1.29	2.17	3.22	3.77	3.72	2.62	0.00	0.91
Total	98.64	98.48	98.71	98.73	99.20	95.28	97.66	96.43	99.93	98.89	98.91	98.77	98.57	98.54	98.70	98.87	98.72
T-site:																	
Si	1.809	1.735	1.680	1.658	1.662	1.720	1.871	1.820	1.949	1.937	1.934	1.982	1.974	1.992	1.949	1.950	1.932
Al	0.191	0.265	0.320	0.342	0.338	0.280	0.129	0.180	0.051	0.063	0.066	0.018	0.026	0.008	0.051	0.050	0.068
Fe^{3+}	0.000	0.000	0.000	0.000	0.000	0.000	0.000	0.000	0.000	0.000	0.000	0.000	0.000	0.000	0.000	0.000	0.000
M1-site:																	
Al	0.055	0.062	0.070	0.079	0.082	0.088	0.046	0.073	0.025	0.023	0.025	0.047	0.039	0.055	0.022	0.023	0.028
Fe^{3+}	0.084	0.103	0.102	0.084	0.071	0.006	0.008	0.021	0.033	0.037	0.063	0.094	0.111	0.110	0.078	0.000	0.027
Ti	0.080	0.114	0.139	0.148	0.146	0.122	0.060	0.076	0.042	0.047	0.050	0.026	0.032	0.021	0.035	0.034	0.044
Cr	0.001	0.001	0.001	0.000	0.000	0.000	0.000	0.000	0.000	0.000	0.001	0.000	0.000	0.000	0.000	0.000	0.000
Mg	0.759	0.697	0.650	0.605	0.582	0.573	0.698	0.651	0.597	0.593	0.594	0.578	0.622	0.557	0.491	0.486	0.489
Fe^{2+}	0.022	0.024	0.038	0.083	0.120	0.211	0.188	0.179	0.304	0.300	0.267	0.255	0.196	0.258	0.374	0.457	0.413
Mn	0.000	0.000	0.000	0.000	0.000	0.000	0.000	0.000	0.000	0.000	0.000	0.000	0.000	0.000	0.000	0.000	0.000
M2-site:																	
Mg	0.000	0.000	0.000	0.000	0.000	0.000	0.000	0.000	0.000	0.000	0.000	0.000	0.000	0.000	0.000	0.000	0.000
Fe^{2+}	0.114	0.122	0.104	0.094	0.085	0.024	0.039	0.039	0.057	0.062	0.068	0.066	0.084	0.063	0.053	0.040	0.056
Mn	0.005	0.006	0.004	0.004	0.006	0.009	0.009	0.010	0.013	0.013	0.012	0.016	0.018	0.020	0.014	0.013	0.013
Ca	0.908	0.917	0.927	0.913	0.903	0.870	0.885	0.880	0.846	0.853	0.859	0.840	0.845	0.840	0.922	0.864	0.860
Na	0.040	0.042	0.048	0.053	0.056	0.077	0.056	0.069	0.087	0.082	0.092	0.127	0.120	0.138	0.065	0.062	0.073
Sum M2:	1.068	1.086	1.084	1.064	1.050	0.981	0.989	0.998	1.003	1.009	1.031	1.049	1.068	1.060	1.054	0.979	1.002
EN%	40.12	37.31	35.60	33.93	32.94	33.83	38.20	36.58	32.25	31.91	31.87	31.26	33.17	30.15	25.40	26.12	26.33
WO%	48.02	49.10	50.79	51.15	51.12	51.38	48.45	49.44	45.72	45.92	46.14	45.44	45.01	45.49	47.70	46.47	46.32
FS%	11.86	13.59	13.61	14.92	15.94	14.79	13.35	13.98	22.03	22.17	22.00	23.30	21.82	24.35	26.90	27.41	27.36
Mg*	77.57	73.75	72.69	69.80	67.88	70.33	74.82	73.17	60.18	59.77	59.87	58.21	61.42	56.43	49.24	49.44	49.70

Appendix A: Microprobe Mineral Analyses
Feldspars

	19a1-119	19a1-120	19a1-121	1b-120	1b-129	1b-130	1b-131		1b-132	1b-133	1b-134	1b-135	1b-136	1b-137	1b-138	1b-139	6b-39	6b-40
		Tepb1									Tepb2							
Oxide wt%	*Kspar in salic segregat.*	*Inter-stitial mass*	*Inter-stitial grain*	*Ground-mass micro*	*Ground-mass micro*	*~13 micron across*	*Tiny interstitial pheno, no tartan twinning*		*Ground-mass micro*	*Ground-mass micro*	*Interstitial microphenocryst*		*Ground-mass micro*	*Ground-mass micro*	*Ground-mass micro*	*Ground-mass micro*	*Ground-mass micro*	*Ground-mass micro*
	core	core	core	core	core	core	rim	core	core	core	rim	core	core	core	core	core	core	core
SiO_2	64.2	58.7	64.5	62.7	51.7	56.1	60.2	57.1	56.1	58.9	57.4		58.4	55.6	57.9	58.7	63.8	65.8
TiO_2	0.2	0.1	0.1	0.2	0.3	0.2	0.2	0.2	0.2	0.1	0.2		0.3	0.3	0.1	0.2	0.3	0.1
Al_2O_3	18.7	22.2	18.4	19.5	22.1	21.4	20.4	21.4	22.8	20.5	21.4		21.2	22.1	22.3	20.8	19.1	19.4
FeO	0.4	0.4	0.3	0.4	0.5	0.5	0.2	0.3	0.5	0.3	0.3		0.4	0.4	0.3	0.3	0.4	0.3
MgO	0.1	0.2	n.d.	0.1	0.2	0.1	n.d.	n.d.	n.d.	n.d.	n.d.		n.d.	n.d.	0.1	n.d.	0.2	n.d.
CaO	0.3	0.9	0.1	0.6	2.9	1.4	0.7	0.9	2.4	0.9	1.4		1.5	1.4	2.7	1.1	2.5	0.5
Na_2O	4.3	6.4	3.4	4.8	3.5	4.0	4.6	4.2	5.0	4.5	4.9		5.1	4.5	5.9	4.3	5.2	4.4
K_2O	10.2	8.3	11.9	8.9	5.2	6.3	7.6	6.6	4.3	7.4	5.6		5.7	5.4	4.0	7.2	8.2	10.0
P_2O_5	n.d.	n.d.	n.d.	n.d.	0.9	0.1	n.d.	n.d.	n.d.	0.2	n.d.		n.d.	0.1	0.1	0.1	1.3	n.d.
SrO	0.6	0.4	0.4	0.8	2.6	1.8	1.0	1.6	2.6	1.2	1.9		1.6	2.6	1.9	1.3	0.3	0.3
BaO	0.1	0.0	0.1	1.0	7.7	6.3	4.0	6.4	5.2	4.5	5.1		4.3	6.4	3.1	4.5	0.2	0.2
Total	99.1	97.5	99.2	99.0	97.6	98.3	99.0	98.6	99.0	98.4	98.3		98.7	98.7	98.5	98.5	101.6	100.8
AB%	38.50	51.79	30.39	43.17	34.62	39.35	42.91	40.78	49.05	41.73	46.76		48.47	44.29	55.44	40.97	43.22	38.85
OR%	59.70	44.18	68.94	52.32	33.98	40.54	46.25	41.91	27.61	45.28	35.59		35.59	35.05	24.64	44.82	45.05	58.45
AN%	1.66	3.99	0.50	2.74	15.87	7.59	3.37	4.86	13.06	4.59	7.67		7.70	7.82	14.08	5.55	11.37	2.33
CS%	0.14	0.04	0.17	1.77	15.53	12.52	7.47	12.44	10.28	8.41	9.98		8.23	12.84	5.84	8.66	0.37	0.37

AB: Albite (Na-rich)
OR: Orthoclase (K-rich)
AN: Anorthite (Ca-rich)
CS: Celsian (Ba-rich)
n.a.: not analyzed
n.d.: below detection limit

Appendix A: Microprobe Mineral Analyses
Feldspars

	6b-42	6b-43	1b-103	1b-104	1b-106	1b-105	1b-107	1b-112	1b-113	1b-114	1b-117	1b-119	5b-69	5b-73	5b-75	5b-70	5b-72	5b-71	5b-76
	Tepb2									Tepv									
Oxide	*Ground-mass micro*	*Ground-mass micro*	*Ground-mass micro*	*Ground-mass micro*	*Anhedral groundmass interstitial micropheno*			*Cpx inclu-sion*	*Ground-mass micro*	*Ground-mass micro*	*Tiny pheno nucleated on wall rock*		*Grain in spherulitic mass*			*Fractured blade*		*Tabular grain, might be twin with 70 &72*	
wt%	core	core	core	core	rim	core	rim	Core	core	core	core	core	core	core	core	core	core	core	core
SiO_2	65.1	63.4	64.2	63.5	64.7	64.2	64.7	64.1	63.2	63.6	63.6	62.8	64.4	64.5	64.5	64.7	64.4	64.3	65.1
TiO_2	0.1	0.2	0.2	0.1	0.2	0.2	0.2	0.3	0.1	0.0	0.2	0.1	0.1	0.1	0.1	0.1	0.1	0.1	0.1
Al_2O_3	19.5	20.1	18.9	18.4	19.0	18.9	18.7	19.4	19.4	19.2	19.5	20.0	18.7	18.8	18.3	18.2	19.3	18.9	18.7
FeO	0.6	0.4	0.2	0.2	0.2	0.3	0.3	0.5	0.1	0.2	0.4	0.4	0.2	0.2	0.4	0.2	0.2	0.2	0.3
MgO	1.1	0.4	n.d.	n.d.	n.d.	n.d.	n.d.	n.d.	n.d.	n.d.	n.d.	0.1	n.d.	n.d.	n.d.	n.d.	n.d.	n.d.	n.d.
CaO	0.6	1.2	0.6	0.5	0.5	0.4	0.3	0.9	0.4	0.6	0.9	1.0	0.4	0.5	0.1	0.2	0.8	0.6	0.3
Na_2O	4.8	5.8	4.4	3.4	6.3	4.5	4.0	5.7	4.3	4.3	4.1	4.8	4.6	4.0	3.4	3.9	4.5	4.8	3.8
K_2O	8.6	6.8	10.0	11.6	7.9	9.9	10.8	8.2	9.7	9.9	10.0	8.5	10.6	11.4	12.3	11.8	10.1	10.2	11.6
P_2O_5	n.d.	0.1	n.d.	0.1	n.d.	n.d.	n.d.	n.d.	n.d.	n.d.	0.1	n.d.	n.d.	n.d.	n.d.	n.d.	n.d.	n.d.	n.d.
SrO	0.3	0.6	0.1	0.1	0.1	n.d.	0.1	0.1	0.3	0.2	0.3	0.3	0.1	0.1	0.1	0.1	0.2	0.1	0.1
BaO	0.4	1.4	n.d.	n.d.	n.d.	n.d.	n.d.	n.d.	1.4	0.7	0.4	1.0	n.d.	n.d.	n.d.	n.d.	n.d.	0.1	n.d.
Total	101.2	100.5	98.7	98.0	98.9	98.4	99.0	99.1	98.9	98.9	99.4	99.0	99.2	99.6	99.2	99.1	99.7	99.1	100.0
AB%	44.06	51.70	38.92	30.28	53.32	40.07	35.70	49.19	38.08	38.33	36.67	42.88	39.06	34.14	29.11	33.05	38.89	40.75	33.06
OR%	52.01	39.91	58.20	67.45	44.13	57.77	62.96	46.61	57.27	57.29	58.31	50.25	59.11	63.28	70.32	66.17	57.14	56.40	65.40
AN%	3.20	5.90	2.88	2.26	2.47	2.16	1.34	4.20	2.09	3.06	4.23	5.03	1.83	2.51	0.55	0.72	3.98	2.76	1.54
CS%	0.73	2.49	0.00	0.00	0.08	0.00	0.00	0.00	2.56	1.32	0.80	1.84	0.00	0.06	0.03	0.07	0.00	0.09	0.00

Appendix A: Microprobe Mineral Analyses
Feldspars

	5b-74	5b-78	5b-79	8c1-19	8c1-20	8c1-21	8c1-22	8c1-23	8c1-24	8c1-25	8c1-26	8c1-27	8c1-28	8c1-29	8c1-30	8c1-32	8c1-33	8c1-34
										Tepv								
Oxide wt%	*Inter-stitial frag* core	*Frag-ment* core	*Skele-tal blade* core	*altered cpx inclus.* core	*altered cpx inclus.* core	*altered cpx inclus.* core	*altered cpx inclus.* core	*Inter-stitial grain* core	*Inter-stitial grain* core	*Inter-stitial grain* core	*Inter-stitial grain* core	*380 X >600 anhedral, corroded, albite-twinned grain* rim	core	core	rim	*675 X ~225 anhedral, tartan-twinned anorthoclase* core	core	rim
SiO_2	65.2	64.6	64.2	65.6	65.8	64.8	66.0	66.1	65.2	65.3	65.7	62.8	62.3	63.4	63.5	60.5	56.7	62.6
TiO_2	n.d.	0.2	n.d.	n.d.	n.d.	n.d.	n.d.	0.1	0.1	0.1	0.1	0.2	0.2	0.1	0.1	0.2	0.1	0.1
Al_2O_3	18.4	19.2	18.5	18.9	18.7	18.6	18.6	18.8	18.8	18.8	18.9	19.7	20.4	20.0	19.9	21.9	23.0	20.2
FeO	0.2	0.2	0.2	0.2	0.2	0.1	0.3	0.2	0.2	0.2	0.2	0.2	0.1	0.1	0.2	0.2	0.2	0.2
MgO	n.d.	0.0	0.0	0.0	n.d.	n.d.	n.d.	n.d.	n.d.	n.d.	n.d.	n.d.	n.d.	n.d.	n.d.	n.d.	n.d.	n.d.
CaO	0.2	0.7	0.2	0.3	0.1	0.2	0.1	0.1	0.2	0.2	0.3	1.0	1.2	1.1	0.9	2.3	2.7	1.2
Na_2O	3.0	5.2	2.8	6.0	4.8	5.3	5.6	5.4	4.6	5.0	4.8	6.6	6.8	6.6	6.8	7.3	5.9	6.6
K_2O	12.8	9.4	13.2	9.0	10.6	10.0	9.8	9.7	10.7	10.1	10.3	7.2	6.1	6.4	6.6	4.0	3.8	6.5
P_2O_5	n.d.	n.d.	n.d.	n.d.	n.d.	n.d.	n.d.	n.d.	n.d.	n.d.	n.d.	n.d.	n.d.	n.d.	n.d.	n.d.	n.d.	n.d.
SrO	0.1	0.1	0.1	0.1	n.d.	0.1	0.1	0.1	0.1	0.2	0.3	0.6	1.1	0.9	0.6	1.7	2.8	0.9
BaO	0.1	n.d.	n.d.	n.d.	0.1	n.d.	n.d.	0.1	n.d.	n.d.	0.2	0.5	1.6	1.1	0.7	1.6	4.3	0.9
Total	100.0	99.6	99.1	100.2	100.2	99.1	100.4	100.6	99.9	99.9	100.7	98.8	99.8	99.8	99.3	99.6	99.4	99.1
AB%	26.18	44.19	24.25	49.43	40.52	44.35	46.53	45.48	39.27	42.57	40.70	55.07	57.58	56.73	57.44	63.60	54.86	56.19
OR%	72.62	52.52	74.90	48.94	58.87	54.89	52.88	53.79	60.01	56.33	57.49	39.24	33.90	36.07	36.96	22.79	23.04	36.46
AN%	1.04	3.29	0.85	1.58	0.48	0.76	0.59	0.63	0.73	1.04	1.54	4.79	5.70	5.32	4.38	10.89	13.96	5.86
CS%	0.16	0.00	0.00	0.05	0.14	0.00	0.00	0.10	0.00	0.07	0.27	0.89	2.82	1.88	1.21	2.72	8.15	1.49

Appendix A: Microprobe Mineral Analyses
Feldspars

	8c1-35	15.1-1	15.1-2	15.1-3	15.1-4	15.1-5	15.1-6	15.1-7	15.1-8	15.1-9	15.1-10	15.1-11	15.1-12	15.1-13	15.1-14	15.1-15
									Tepv							
	Anorth-oclase	*215 micron wide tabular grain*				*Tabulr micro-pheno*	*440 micron wide, skeletal grain*									
Oxide wt%	core	rim	core	core	rim	rim	rim	core	core	core	core	core	core	core	rim	rim
SiO_2	61.6	61.1	58.4	56.6	59.9	64.7	55.9	57.5	57.4	55.1	54.2	55.5	59.6	56.2	63.2	63.3
TiO_2	0.2	0.1	0.2	0.3	0.1	0.1	0.1	0.1	0.2	0.2	0.2	0.2	0.1	n.d.	n.d.	0.1
Al_2O_3	20.5	20.9	21.6	21.5	21.3	19.7	21.5	21.1	21.4	21.9	21.8	22.1	20.8	18.2	19.5	19.4
FeO	0.2	0.1	0.1	0.2	0.1	0.1	0.2	0.2	0.2	0.2	0.2	0.2	0.1	0.1	0.1	0.2
MgO	n.d.	n.d.	n.d.	n.d.	n.d.	n.d.	n.d.	n.d.	n.d.	n.d.	n.d.	n.d.	n.d.	n.d.	n.d.	n.d.
CaO	1.5	0.9	0.8	1.0	1.1	0.6	1.1	0.7	0.8	0.9	1.4	1.3	0.9	5.3	0.4	0.4
Na_2O	6.9	5.1	4.9	4.5	5.3	4.8	3.8	4.3	4.5	4.5	4.8	4.6	5.4	3.8	4.6	4.4
K_2O	5.8	6.7	6.4	6.3	6.0	9.5	7.1	7.0	6.6	6.0	4.7	5.3	6.6	9.6	9.9	10.5
P_2O_5	0.1	n.d.	0.1	0.2	n.d.	n.d.	0.1	n.d.	n.d.	n.d.	n.d.	n.d.	n.d.	3.9	n.d.	n.d.
SrO	1.1	1.9	2.0	1.9	2.2	0.3	2.4	1.9	2.1	2.4	2.7	2.8	1.8	0.6	0.2	0.2
BaO	1.2	2.9	5.0	5.9	3.0	0.1	4.9	5.4	5.5	5.9	4.8	5.9	2.2	0.1	n.d.	0.1
Total	99.1	99.7	99.5	98.5	98.9	99.9	97.1	98.3	98.6	97.1	94.8	97.8	97.4	97.9	98.0	98.6
AB%	58.70	48.05	46.10	43.22	50.76	42.26	37.93	41.60	43.14	44.38	49.70	45.99	50.62	29.05	40.22	38.12
OR%	32.08	41.88	40.04	39.81	37.65	54.64	46.33	44.07	41.87	38.88	31.97	35.15	40.71	48.47	57.72	59.77
AN%	7.16	4.50	4.24	5.49	5.79	2.95	5.95	3.77	4.33	5.06	8.31	7.03	4.53	22.29	2.05	2.00
CS%	2.06	5.57	9.62	11.48	5.81	0.15	9.78	10.56	10.66	11.67	10.02	11.83	4.15	0.19	0.01	0.10

Appendix A: Microprobe Mineral Analyses
Feldspars

	15.1-16	15.1-17	15.1-18	15.1-19	15.1-20	15.1-21	15.1- 22	15.1-23	15.1-24	15.1-25	15.1-26	15.1-27	15.1-28	15.1-29	15.1-30
								Tepv							
	85 micron wide, tabular, skeletal grain					*580 micron wide, tabular, euhedral pheno, ~0.5 mm from crack*					*~40 micron wide, anhedral grain, ~ 0.5 mm from analcime-filled crack*			*125 X 20 micron groundmass grain*	
Oxide wt%	rim	core	core	core	rim	rim	core	core	core	rim	rim	core	rim	rim	rim
SiO_2	60.7	61.7	62.8	63.6	65.5	65.9	64.3	65.1	65.7	62.6	64.0	63.1	63.0	64.2	63.9
TiO_2	0.1	0.1	0.1	0.1	0.1	0.1	0.1	n.d.	0.1	0.1	n.d.	n.d.	0.1	0.1	n.d.
Al_2O_3	19.5	19.5	19.7	19.5	19.9	19.3	19.0	19.1	19.5	18.4	19.5	19.4	19.3	19.3	19.1
FeO	0.1	0.1	0.2	0.2	0.2	0.3	0.2	0.2	0.2	0.2	0.3	0.3	0.3	0.2	0.2
MgO	n.d.	n.d.	n.d.	0.1	n.d.	n.d.	n.d.	n.d.	n.d.	n.d.	n.d.	n.d.	n.d.	n.d.	n.d.
CaO	0.6	0.7	0.7	0.5	0.4	0.1	0.1	0.1	0.1	1.9	0.3	0.3	0.3	0.3	0.1
Na_2O	3.1	3.6	4.0	4.1	3.7	3.8	4.2	4.0	4.1	3.3	3.1	3.0	2.6	1.5	1.7
K_2O	11.8	11.1	10.3	10.3	11.3	12.2	11.0	11.7	11.4	12.2	12.2	12.5	13.1	14.7	14.6
P_2O_5	n.d.	n.d.	n.d.	n.d.	n.d.	n.d.	n.d.	n.d.	n.d.	1.1	n.d.	n.d.	n.d.	n.d.	n.d.
SrO	0.5	0.5	0.6	0.6	0.6	0.1	0.1	0.1	0.1	0.1	0.4	0.4	0.4	0.3	0.2
BaO	0.1	0.2	0.3	0.3	0.3	n.d.	n.d.	n.d.	n.d.	n.d.	0.2	0.2	0.1	0.3	0.1
Total	96.6	97.5	98.6	99.3	102.0	101.7	99.1	100.2	101.1	99.8	99.9	99.4	99.2	101.0	100.0
AB%	27.64	31.81	35.56	36.61	32.42	31.86	36.80	33.88	34.97	26.42	27.63	26.33	22.80	13.17	14.75
OR%	69.01	64.67	60.61	60.14	65.17	67.62	62.69	65.77	64.67	64.99	70.54	71.62	75.74	85.01	84.33
AN%	3.09	3.20	3.25	2.61	1.89	0.48	0.51	0.30	0.29	8.59	1.52	1.63	1.30	1.36	0.67
CS%	0.26	0.31	0.58	0.63	0.52	0.05	0.01	0.04	0.07	0.00	0.31	0.42	0.17	0.47	0.25

Appendix A: Microprobe Mineral Analyses
Feldspars

	15.1-31	15.1-32	15.1-33	15.1-34	15.1-36	15.1-37	15.1-38	15.1-39	21.1-1	21.1-2	21.1-3
	100 X 125 micron skeletal, tabular grain; points taken ~20 microns from edge				Tepv *>1mm subequant, corroded phenocryst*		*70 micron grain*	*25 micron grain*	*Ground-mass*	*Ground-mass*	*Ground-mass*
Oxide wt%	rim	rim	rim	rim	core	core	rim	rim	core	core	core
SiO_2	63.8	64.0	63.4	62.3	56.3	64.8	62.7	64.7	64.2	60.0	65.7
TiO_2	n.d.	n.d.	0.1	n.d.	n.a.	n.a.	n.a.	n.a.	n.d.	0.1	n.d.
Al_2O_3	19.1	18.7	18.9	18.7	21.9	18.8	20.0	18.9	19.0	20.7	20.0
FeO	0.2	0.2	0.2	0.2	0.1	0.2	0.3	0.2	0.1	0.1	0.1
MgO	n.d.	n.d.	n.d.	n.d.	n.d.	n.d.	0.2	n.d.	n.d.	n.d.	n.d.
CaO	0.1	n.d.	n.d.	n.d.	0.7	0.1	0.9	0.1	0.3	0.7	0.7
Na_2O	2.6	2.6	2.5	2.0	4.0	4.1	4.8	4.2	4.5	4.8	5.1
K_2O	13.6	13.5	13.6	14.2	6.0	11.1	8.5	10.7	10.1	7.2	9.0
P_2O_5	n.d.	n.d.	n.d.	n.d.	n.a.	n.a.	n.a.	n.a.	n.d.	n.d.	n.d.
SrO	n.d.	0.1	0.1	0.1	2.2	0.1	0.8	0.2	0.1	1.2	0.3
BaO	n.d.	n.d.	n.d.	n.d.	7.8	n.d.	0.4	0.1	0.1	3.8	n.d.
Total	99.5	99.1	98.7	97.6	99.1	99.3	98.5	99.2	98.4	98.6	100.8
AB%	22.03	22.77	22.00	17.75	40.30	35.50	43.63	37.35	39.41	45.12	44.57
OR%	77.32	77.08	77.75	82.22	39.76	63.77	51.22	61.71	58.82	44.19	52.20
AN%	0.59	0.15	0.18	0.00	4.05	0.65	4.40	0.71	1.68	3.52	3.19
CS%	0.05	0.00	0.08	0.03	15.88	0.08	0.75	0.22	0.10	7.17	0.04

Appendix A: Microprobe Mineral Analyses
Nepheline

	1b-110	1b-111	19a1-1	19a1-2	19a1-3	19a1-13	19a1-72	19a1-73	19a1-74
	Tepv					Tepb1			
Oxide wt%	*~50 micron, anhedral grain in core of large, euhedral cpx*		*Anhedral grain in salic segregation* rim	core	*Apatite(?) contamination*	*Anhedral groundmass grain*	*Anhedral groundmass grain*	*Anhedral groundmass grain*	*Anhedral groundmass grain*
SiO_2	47.6	48.8	45.5	46.3	42.0	45.0	48.7	45.5	46.7
Al_2O_3	30.8	30.8	32.3	31.3	29.7	31.9	32.1	32.9	31.3
TiO_2	n.d.	n.d.	0.1	n.d.	0.1	0.1	n.a.	n.a.	n.a.
MgO	n.d.	n.d.	n.d.	0.3	0.1	n.d.	n.d.	n.a.	0.6
FeO^t	0.5	0.4	0.8	0.8	0.7	0.9	0.7	0.8	0.9
CaO	1.1	1.2	0.4	0.7	4.6	0.7	0.2	0.3	1.3
Na_2O	16.5	16.0	16.4	14.5	14.3	16.2	17.2	16.9	15.0
K_2O	2.5	2.3	4.2	3.6	3.7	4.2	3.2	4.1	3.6
SrO	n.d.	n.d.	n.d.	n.d.	0.2	n.d.	n.d.	n.d.	n.d.
BaO	n.d.	n.d.	n.d.	0.1	n.d.	n.d.	n.d.	n.a.	n.a.
P_2O_5	n.d.	0.1	n.d.	n.d.	3.3	n.d.	n.a.	n.a.	n.a.
Total	98.9	99.5	99.8	97.6	98.8	99.1	102.3	100.4	99.4
NE%	85.11	85.20	83.62	82.01	65.53	81.85	88.01	85.08	79.79
KS%	8.34	7.92	14.22	13.32	11.14	14.11	10.89	13.46	12.69
AN%	6.55	6.88	2.16	4.67	23.33	4.04	1.10	1.47	7.51

NE: Nepheline (Na-rich)
KS: Kalsilite (K-rich)
AN: Anorthite (Ca-rich)
n.a.: not analyzed
n.d.: below detection limit

Appendix A: Microprobe Mineral Analyses
Fe-Ti oxides

	19a1-18	19a1-19	1b-1	1b-2	1b-3	1b-4	1b-5	1b-6	1b-12	1b-13	1b-7	1b-8	1b-9	1b-10	1b-11	1b-14	1b-15
	Tepb1									Tepv							
	Two domain, inclusion-rich, anhedral grain		*0.5 X 0.75 mm hopper-textured phenocryst. Abundant exolution lamellae.*								*0.5 X 0.25 mm anhedral phenocryst*					*Nucleated on cpx*	
Oxide wt%	Ilm_{93}	Ilm_{24}	$Usp_{2.0}$(?)	Ilm_{81}(?)	$Usp_{2.4}$(?)	$Usp_{1.5}$(?)	Ilm_{36}(?)	Ilm_{61}(?)	Ilm_{66}(?)	Ilm_{88}(?)	Ilm_{64}(?)	$Usp_{2.8}$(?)	Ilm_{98}(?)	$Usp_{4.5}$(?)	Ilm_{59}(?)	b.a.	Ilm2.7
SiO_2	0.8	0.1	0.1	0.1	0.0	0.0	0.0	0.0	0.1	0.0	0.0	0.0	0.0	0.0	0.1	0.0	0.1
TiO_2	51.7	15.9	1.4	40.5	1.8	1.3	19.4	31.5	33.2	43.4	32.1	1.0	48.9	1.6	29.9	37.8	2.2
Al_2O_3	0.5	1.9	6.0	0.6	6.1	8.1	0.9	0.8	0.9	0.7	0.5	2.9	0.3	7.1	0.6	0.2	0.9
FeO^t	36.4	70.2	70.4	50.8	68.7	65.0	69.4	60.1	56.6	47.0	58.8	84.2	44.5	79.5	61.9	46.8	84.4
MnO	0.8	0.6	6.6	0.5	7.3	8.5	0.8	0.6	0.6	0.6	0.5	2.3	0.3	2.2	0.5	0.7	0.7
MgO	8.8	3.7	7.9	0.9	8.0	8.9	1.5	1.3	1.1	1.0	0.8	1.6	0.4	2.6	0.7	0.9	0.3
CaO	0.1	0.1	0.0	0.0	0.0	0.0	0.0	0.0	0.0	0.0	0.0	0.0	0.0	0.0	0.0	1.2	0.0
Cr_2O_3	0.2	1.7	0.1	0.0	0.0	0.0	0.0	0.0	0.0	0.0	0.0	0.0	0.0	0.0	0.0	0.0	0.0
V_2O_3	n.a.	0.3	0.2	0.2	0.2	0.2	0.3	0.3	0.1	0.1	0.3	0.3	0.2	0.2	0.2	0.0	0.1
NiO	0.0	0.2	0.1	0.0	0.2	0.4	0.1	0.1	0.0	0.0	0.0	0.1	0.0	0.1	0.0	0.1	0.1
ZnO	0.0	0.2	0.9	0.0	0.8	0.8	0.1	0.0	0.0	0.1	0.0	0.1	0.0	0.5	0.0	0.0	0.1
Sum	99.3	94.7	93.5	93.6	93.2	93.2	92.5	94.7	92.7	92.9	93.1	92.6	94.7	93.9	93.8	87.7	88.8
Ulvospinel-Magnetite:																	
FeO		39.0	13.7		12.9	10.0	44.6	56.3			57.3	27.2		26.8	55.7		30.4
Fe_2O_3		34.6	63.0		61.9	61.0	27.6	4.2			1.7	63.3		58.6	6.8		60.0
Total		98.2	99.8		99.4	99.3	95.2	95.1			93.3	98.9		99.8	94.5		94.9
Ilmenite-Hematite:																	
FeO	30.8	6.8		34.3			13.9	25.4	27.4	36.6	27.0		43.0		25.2	30.1	0.7
Fe_2O_3	6.2	70.4		18.3			61.7	38.6	32.4	11.5	35.3		1.6		40.8	18.5	93.0
Total	100.0	101.8		95.5			98.6	98.5	95.9	94.1	96.7		94.8		97.9	89.5	98.2

FeO^t: Total iron expressed as FeO
Ilm: Ilmenite
Usp: Ulvospinel
?: Phase identification is problematic
n.a.: not analyzed
n.d.: below detection limit
b.a.: bad analysis
Blank fields denote negative values for partitioned iron.
Underlines denote suspect values.

Appendix A: Microprobe Mineral Analyses
Fe-Ti oxides

	1b-16	1b-17	1b-18	1b-19	1b-20	21.1-31	21.1-32	21.1-33	21.1-34	21.1-35	21.1-36	21.1-37	21.1-38	21.1-39	21.1-40	21.1-41
	~50 micron microphenocryst of Fig. 7. Abundant exolution lamellae				*~10 micron gndmas*	*Nucleate at cpx margin*	*Nucleate at cpx margin*	Tepv *~300 micron long, anhedral grain nearly surrounded by small cpx phenocryst*					*~50 micron grain without apparent exolution lamellae*			
Oxide wt%	Ilm3.3	b.a.	b.a.	$Usp_{2.7}$	Ilm9.5	Ilm_{48}	Ilm_{56}	Ilm_{47}	Ilm_{93}	Ilm_{63}	Ilm_{45}	b.a.	$Usp_{0.2}$	$Usp_{0.2}$	$Usp_{0.0}$	$Usp_{0.1}$
SiO_2	0.1	0.1	2.0	0.1	0.1	0.0	0.1	0.0	0.0	0.0	0.0	0.1	0.1	0.2	0.2	0.3
TiO_2	5.0	61.8	57.4	1.1	6.3	24.4	27.4	23.6	46.1	31.3	22.9	49.0	0.1	0.1	0.0	0.0
Al_2O_3	8.7	1.3	1.8	4.3	0.4	0.4	0.3	2.6	1.5	3.9	1.5	3.6	0.1	0.1	0.1	0.3
FeO^t	74.9	32.1	32.4	77.0	81.2	63.4	63.3	65.8	43.5	56.5	67.1	38.6	85.0	85.9	86.1	84.8
MnO	0.5	0.2	0.2	7.4	1.3	0.7	0.1	0.5	1.8	0.7	0.8	1.6	0.3	0.1	0.2	0.2
MgO	1.7	0.4	2.0	1.2	0.5	0.7	0.1	0.8	0.8	1.2	0.7	1.4	0.0	0.0	0.1	0.1
CaO	0.0	0.0	0.4	0.0	0.0	0.2	0.2	0.0	0.0	0.0	0.0	0.0	1.7	1.2	1.1	1.5
Cr_2O_3	0.0	0.0	0.0	0.0	0.0	0.0	0.0	0.0	0.1	0.1	0.0	0.0	0.0	0.0	0.0	0.0
V_2O_3	0.2	0.1	0.0	0.0	0.0	0.1	0.0	0.3	0.1	0.3	0.3	0.1	0.1	0.0	0.0	0.0
NiO	0.1	0.0	0.0	0.1	0.0	0.3	0.1	0.1	0.1	0.1	0.0	0.1	0.0	0.0	0.0	0.2
ZnO	0.6	0.2	0.0	0.1	0.5	0.2	0.0	0.1	0.1	0.2	0.1	0.3	0.0	0.0	0.0	0.1
Sum	91.9	96.1	96.2	91.4	90.3	90.5	91.6	93.7	94.0	94.2	93.4	94.8	87.3	87.7	87.8	87.6
FeO	32.4			22.6	33.1	48.8	53.9	50.3		56.3	49.3		27.0	27.9	27.9	27.2
Fe_2O_3	47.2			60.5	53.5	16.2	10.4	17.2		0.2	19.8		64.4	64.5	64.7	64.0
Total	96.6			97.4	95.6	92.1	92.6	95.5		94.2	95.3		93.8	94.1	94.3	94.0
FeO	0.4				3.0	19.2	24.2	19.3	38.1	25.1	18.5					
Fe_2O_3	82.9				86.9	49.1	43.4	51.7	6.0	34.9	54.0					
Total	100.2				99.0	95.4	95.9	98.9	94.6	97.7	98.8					

APPENDIX B: Thin Section Petrography

This appendix consists of annotated laboratory notes. Sample numbers include the date on which samples were collected; however, the characters to the right of hyphens are unique. Therefore, only these latter characters are referenced in the body of the paper and in illustrations and other tables. Figures referenced in the descriptions will be found in Lofgren, 1980. Modes listed were visually estimated during petrographic analysis. Attempts to identify opaque phases were generally unsuccessful; and these are grouped together as Fe-Ti oxides with few exceptions.

941214-1A

Loose clast from east side of El Porticito

Wall rock phenocrysts (≥200 μm):

Mode %	Phase	Description
8	Olivine	≤600 μm. All grains fractured. Margins & some interiors altered to Fe-Ti oxides, iddingsite & clay.
8	Fe-Ti oxides	≤400 μm. Euhedral to anhedral with embayed margins. Most anhedral grains have limonite stain around margins. Larger grains fractured. Abundant silicate inclusions. Components have separated to form exsolution lamellae.
4	Titanaugite	≤2 mm; most <500 μm. Brownish-violet, similar to titanaugite in veins, but lighter. Margins corroded, with alteration products of Fe-Ti oxides, chlorite, & clay. Corrosion much less severe than in olivine.

Wall rock groundmass (<200 μm):

Mode %	Phase	Description
56	Augite	Euhedral, prismatic. Opaque inclusions (≤10 μm) common. Some apatite inclusions. Occurs as individual grains found in veinlets and leucocratic segregations.
16	Fe-Ti oxides	Embayed margins altered to limonite.
2	Alkali feldspar	Anhedral. Interstitial and in leucocratic segregations and veinlets. Apatite inclusions. Most grains have undergone partial alteration to sericite and clay.
2	Nepheline	Anhedral. Interstitial and in leucocratic segregations and veinlets. Apatite inclusions. Many grains partially altered to clay.
2	Sericite & clay	Very fine-grained.
1	Analcime	Anhedral. Interstitial. Apatite inclusions.
1	Biotite	Tabular, straight sides, ragged ends.
tr.	Apatite	Acicular. Included in other phases; often needles penetrate boundaries between adjacent crystals. Most common in leucocratic segregations and veinlets.

Coarse-grained vein:

Mode %	Phase	Description
30	Alkali feldspar	Various morphologies (Figures refer to those in Lofgren, 1980): 1. Fan-spherulitic (open-coarse) (Fig. 6E): Blades ≤500 × ≤75 μm. Most are twinned parallel to long axis of blade. Some have sharp twin planes, similar to plagioclase. Some blades are curved, as in 7B. These fan-spherulitic (open coarse) textures are interpreted as corresponding to Lofgren's experimental results with low An content feldspars grown from water-rich melts. 2. Skeletal (Fig. 10-875, -800, -740): ≤1 mm long. Unfractured or slightly fractured. Some exhibit zonation subparallel to long axes. These skeletal textures are interpreted as corresponding to quenching from relatively high temperatures in Lofgren's experiments. 3. Skeletal to well-formed (Fig. 10-700 to 8-600): Grains often >1 mm long; some originally >4 mm long. Textures and grain sizes are interpreted as indicating more extensive crystal growth prior to cooling through the magma solidus than for 1 and 2 above. About 30% of these crystals exhibit the ragged ends and tartan twinning common in anorthoclase; one small subgrain (200 × 500 μm) exhibits intergrowth texture similar to Fig. 20B (rt. side). Grains tend to be highly fractured, with largest ones having undergone most grain size reduction and most extensive alteration to sericite and clay. Some grains exhibit undulose extinction and/or deformational cleaving parallel to long axis; are twinned and/or zoned; and partially or totally enclose opaque minerals, pyroxene, smaller feldspar and apatite crystals.
27	Titanaugite	Two dominant morphologies: 1. ≤400 μm long, usually wedge-shaped, with irregular, ragged ends. Most crystals have inhomogeneously nucleated and have grown into the vein from the wall rock margin.. 2. 200 μm ≤ length ≤5 mm long. Usually tabular, sometimes skeletal, with straight to irregular sides. Ends are straight to ragged. Many have centers consisting of feldspar (partially altered to sericite) and/or Fe-Ti oxides. Most margins, and some interiors, of larger grains are corroded and altered to clay, chlorite, and Fe-Ti oxides which in turn are altered to limonite. Some grains of both morphologies have 'necklaces' of Fe-Ti microphenocrysts around their margins. Some augites continued to grow a few 10's of μm beyond these necklaces. Both morphologies are pleochroic violet to brownish violet; concentric- and/or sector-zoned; often twinned parallel to

		the long axis.
15	Nepheline	≤500 μm. Uniaxial negative, δ≈0.004. Very similar to tabular feldspar morphology. Some have inclusions of apatite; some grains are slightly altered to clay.
11	Fe-Ti oxides	≤2 mm. Occur as phenocrysts and as alteration products of titanaugites. Also occurs as acicular, sometimes vermicular, grains and radiating sheaves near vein-wall rock contact, enclosed in analcime and sericite. All exhibit exsolution blebs or lamellae. Larger subhedral to euhedral grains often exhibit hopper morphology. Inclusions are pyroxene, feldspar and apatite. Commonly partially altered to limonite.
7	Sericite(?)	Colorless, fibrous groundmass phase containing numerous inclusions of vermicular Fe-Ti oxides. Concentrated at vein-wall rock contact; may be unidentified zeolite. Also as an alteration product of feldspar.
5	Analcime	Nearly isotropic. Structureless except for pervasive fractures, which tend to be filled with very fine-grained material. Most common at vein-wall rock contact.
1	Natrolite	Yellowish, very fine-grained, fibrous.
1	Hematite	≤2 mm. Bright red, translucent. Pseudomorphing hopper-morphology Fe-Ti oxides.
1	Apatite	≤100 μm across base. Acicular grains, sometimes with aspect ratios >30:1. Abundant basal sections probably indicate a local shape-preferred orientation ⊥ plane of thin section. All grains enclosed by one or more other crystalline phases. Fluid inclusions are common in central portions of basal sections.
1	Augite	≤200 μm. Anhedral, interstitial. Light green.
1	Calcite	Filling sharply-defined veinlets that crosscut vein-wall rock interfaces.
tr.	Limonite	Very fine-grained, orange to reddish-brown, translucent, non-pleochroic, non-birefringent.

The multiple textures exhibited by feldspar and titanaugite in the vein are interpreted as indicating multiple stages of nucleation and crystallization, with the coarser, more developed grains having grown at depth and been carried into their present positions during vein emplacement, and the finer-grained phases having nucleated and grown later.

In this thin section is seen a partially-detached fragment of wall rock at the vein-wall rock interface. The fragment is wedge-shaped, ~2.5 cm long × 1.5 cm at its base, where it remains attached to the wall rock. The fragment, as well as the main body of wall rock, is laced with leucocratic veinlets. Between the fragment and the wall rock proper is a wedge of vein that narrows to become a veinlet within the wall rock. The phases in this veinlet, as well as others in the thin section, are identical to the leucocratic phases in the vein. Alteration of wall rock is noticeably more extensive along the vein-wall rock interface than in the wall rock interior, with a resulting increase in Fe-Ti oxide crystals, clay, and limonite. This alteration is most intense around the margin of the wall rock fragment.

941214-1B

Thin section cut perpendicular to that of 941214-1A. No partially-detached wall rock fragments are included in this section.

Wall rock phenocrysts (≥200 μm):

Mode %	Phase	Description
5	Olivine	Similar to 941214-1A.
4	Fe-Ti oxides	Similar to 941214-1A.
2	Titanaugite	Similar to 941214-1A.

Wall rock groundmass (<200 μm):

Mode %	Phase	Description
78	Augite	Similar to 941214-1A.
6	Fe-Ti oxides	Similar to 941214-1A.
2	Alkali feldspar	Similar to 941214-1A.
1	Nepheline	Similar to 941214-1A.
1	Sericite & clay	Similar to 941214-1A.
1	Analcime	Similar to 941214-1A.
tr.	Apatite	Similar to 941214-1A.

Vein:

Mode %	Phase	Description
40	Alkali feldspar	Similar to 941214-1A.
25	Titanaugite	Similar to 941214-1A.
9	Nepheline	Similar to 941214-1A.
9	Fe-Ti oxides	Similar to 941214-1A.
8	Analcime	Similar to 941214-1A.
5	Sericite	Similar to 941214-1A.
2	Hematite	Similar to 941214-1A.
1	Augite	Similar to 941214-1A.
1	Apatite	Similar to 941214-1A.
tr.	Calcite	Similar to 941214-1A.
tr.	Limonite	Similar to 941214-1A.

Wall rock veinlets and leucocratic segregations appear to grade into wall rock ground mass, and are distinguished from it by predominance of

leucocratic, and scarcity of melanocratic, minerals. Where leucocratic wall rock veinlets extend to the vein-wall rock interface, they merge with the vein groundmass without noticeable change in leucocratic phases.

Solidification sequence at vein-wall rock interface in 941214-1A & -1B:

Apatite (crystallized throughout solidification history.)

Inhomogeneously nucleated titanaugite

Vermicular to acicular magnetite

K-spar

Glass

Post-solidification processes included corrosion of titanaugite grain margins to Fe-Ti oxides, alteration of Fe-Ti oxide to limonite, corrosion of feldspar to sericite and clay, and alteration of glass to analcime and sericite.

950204-2.1

El Porticito weathered coarse-grained subvertical vein on north end of east side, ~7m above colluvium. No wall rock is included in this thin section.

Vein:

Mode %	Phase	Description
40	Alkali feldspar	Morphologies similar to those of 941214-1A & -1B, but tabular grains range in length to ~3 mm. $\delta \leq 0.012$. Finer-grained, bladed, radiating grains are essentially undeformed and unaltered. Larger grains have generally undergone grain size reduction through fracturing and partial alteration to sericite and clay. Undulose extinction is common. About 25% of larger grains exhibit tartan twinning typical of anorthoclase. $2V \approx 20°$ for these grains, within the range for anorthoclase.
17	Stilbite	In groundmass. Radiating bundles, low negative relief, $\delta \approx 0.007$. Occasional 'bow tie' morphology.
15	Analcime	$\delta \approx 0$. Low relief. Irregular masses with abundant inclusions of Fe-Ti oxides, apatite, and feldspar.
10	Titanaugite	Tabular to bladed, subhedral to euhedral, brownish-purple. Most are fractured and have undergone varying degrees of alteration to Fe-Ti oxides, chlorite, and clay. Some grains have rows of fluid inclusions across them.
10	Fe-Ti oxides	Occur as alteration phase of titanaugite and as phenocrystic grains, sometimes exhibiting hopper texture; also as radiating, acicular grains. Some grains partially altered, surrounded by limonite. Inclusions in hopper voids are primarily analcime.
7	Calcite	Vein- (crack-?) filling phase and alteration product of large feldspar grains.
1	Hematite	Replacement product of Fe-Ti oxides, sometimes exhibiting hopper texture.
tr.	Apatite	Acicular grains included in most phases except fan spherulitic and skeletal feldspars.
tr.	Augite	Occurs as isolated grains and near margins of titanaugite, of which it may be an alteration product.
tr.	Sericite	Alteration product of feldspar.
tr.	Limonite	Occurs as small, isolated masses and around margins of Fe-Ti oxides

950204-5A

El Porticito east side subvertical, fine-grained vein with wall rock inclusion:

Wall rock inclusion ~1 cm × 500 μm (no phenocrysts):

Mode %	Phase	Description
59	Titanaugite	<150 μm long. Brownish purple; pleochroic. Tabular to bladed, some with swallow tails. Rare grains appear to be alteration products of olivine.
27	Alteration products	Dark, reddish-brown, very fine-grained material. Probably clay, limonite, and sericite.
8	Fe-Ti oxides	Opaque, metallic gray. Anhedral. Extensively altered to very fine-grained, reddish-orange limonite.
5	Feldspar(?)	<100 μm. Colorless grains
1	Analcime(?)	Nearly isotropic linear zones up to 250 μm wide with numerous <10 μm long, birefringent crystallites.

Vein:

Mode %	Phase	Description
30	Alkali feldspar	Morphologies and sizes similar to those in 941214-1A. At least one blade like Fig. 9F (a skeletal interior). Larger grains are pervasively fractured; some are twinned and/or zoned. Some larger grains altered up to ~50% sericite. As many as 3 generations of feldspar can be distinguished.
30	Analcime	Colorless, nearly isotropic. Most abundant adjacent to wall rock inclusion.
15	Nepheline	Morphology and size similar to 941214-1A. Uniaxial negative, δ≈0.004. Unambiguously identified crystals tend to be tabular with straight to slightly embayed margins. Some alteration to clay.
10	Titanaugite	Similar in size and morphology to those in 941214-1A. Tabular to slightly wedge-shaped. Small (<1 mm) crystals have nucleated on opaque minerals around margin of inclusion.
7	Fe-Ti oxides	Occurs as small grains around margin of inclusion, as alteration products in and around titanaugite grains, and as separate phenocrysts.
5	Augite	Pleochroic green to brownish-green. Tabular to skeletal, with apatite and opaque inclusions.
3	Apatite	Acicular grains included in other phases.
tr.	Stilbite	Colorless, bladed, radiating.
tr.	Limonite	Alteration product of Fe-Ti oxides.

The interface between the wall rock inclusion and vein appears to be gradational, especially when viewed between crossed polars. The transition zone is made up primarily of analcime, with inclusions of titanaugite, feldspar, dendritic and subequant Fe-Ti oxides, and crystallites similar to those found in the inclusion. Silicate grains within the inclusion are fractured. The compositions and textures observed are interpreted as representing partial melting and 'digestion' of the inclusion by the vein magma.

950204-5B

Thin section cut ⊥ to 950204-5A; both wall rock and vein are included.

Wall rock:

Mode %	Phase	Description
55	Titanaugite	Similar to -5A. Clay, Fe-Ti oxides, and chlorite alteration products visible in some microphenocrysts.
16	Alteration products	Dark, reddish-brown, very fine-grained material. Probably clay, limonite, and sericite concentrated along wall rock-vein interface.
15	Olivine	Occurs as phenocrysts ≤500 μm and in groundmass. Phenocrysts are extensively altered to opaque minerals; most are fractured.
8	Fe-Ti oxides	Similar to -5A.
5	Feldspar(?)	Similar to -5A.
1	Analcime(?)	Nearly isotropic linear zones up to 250 μm wide with numerous <10 μm long, birefringent crystallites.
tr.	Apatite	Ubiquitous as inclusions in feldspar and analcime.

Vein:

Mode %	Phase	Description
20	Alkali feldspar	Grains tend to be slightly larger than those in -5A. Morphologies similar to those in 941214-1A. Larger grains are pervasively fractured. Largely altered to sericite & clay.
20	Titanaugite	Similar morphologies to -5A, but grains much larger (up to 5 mm long). Larger grains often contain cores of Fe-Ti oxides and feldspars; the latter exhibit fluid inclusions and alteration to sericite.
20	Analcime	Colorless, nearly isotropic. Most abundant adjacent to wall rock inclusion.
20	Sericite	Alteration product of feldspars (and titanaugite?) and as groundmass phase. (The latter may be an unidentified zeolite.)
10	Fe-Ti oxides	Similar to -5A. Some larger grains exhibit hopper texture.
5	Nepheline	Similar to -5A.
4	Stilbite	Fan-spherulitic, colorless, low relief.
1	Augite	Similar to -5A.
tr.	Apatite	Acicular grains included in other phases.

950317-6B

Wall rock adjacent to 0.3 m thick vein at north end of El Porticito above Largo Creek. Thin section contains an olivine glomerocryst.

Wall rock glomerocryst:

Mode %	Phase	Description
2	Olivine	500 μm × 500 μm glomerocryst consists of 24 individual fractured, equant olivine crystals. Crystal margins, and some fracture surfaces, are altered to iddingsite (brown) and chlorophaeite (green). Fe-Ti oxide alteration products are confined to the glomerocryst margin. Groundmass crystals around the glomerocryst exhibit no shape-preferred orientation. Crystals contain ≤10 μm oblong to round inclusions. Locally these inclusions are tabular and densely clustered into multiple rows in which the long axes of the inclusions, if they are elongate, are oblique ~20° to the axes of rows. In reflected light, inclusions exposed on the surface form pits. These inclusions appear to be fluid inclusions lying along lattice planes.

Wall rock phenocrysts (≥200 μm):

Mode %	Phase	Description
12	Olivine	≤2 mm. All grains are fractured. Chemical alteration is variable from margins replaced by Fe-Ti oxides and iddingsite, to replacement of entire grains. Rows of fluid inclusions are visible in least altered grains.
5	Fe-Ti oxides	≤400 μm. Euhedral to subhedral; some embayed. Mostly alteration products of olivine and titanaugite; but ~40% are not obviously associated with silicate phases. All exhibit exsolution of Fe and Ti components. Margins are altered to limonite.
3	Titanaugite	≤1.5 mm. Euhedral, fractured. Some, but not all, larger grains contain abundant ≤25 μm inclusions in central, and some concentric, zones. These inclusions are multiphase: metallic oxides and silicates. Inclusions appear to be growth-, rather than alteration-, related. Titanaugite is variably altered to Fe-Ti oxides, clay, and limonite, with much less alteration than olivine. Most alteration confined to margins and around inclusions. Occasional fluid inclusions also present.

Groundmass:

Mode %	Phase	Description
56	Augite	Subhedral to euhedral, tabular. Some grains have lobate margins shared with alkali feldspar. ~20% have some limonite alteration.
14	Alkali feldspar	Anhedral. Interstitial to augite, as isolated grains and as irregular, sometimes elongate, masses. Interstitial relationship to augite microphenocrysts is indicated by cuspate margins of feldspar vs. lobate margins of augite where the two phases share boundaries. Some grains exhibit tartan twinning; some are partially altered to sericite; and some have fluid(?) inclusions.
8	Fe-Ti oxides	Anhedral to subhedral. All exhibit exsolution lamellae.
tr.	Biotite	Brown, green, and greenish-brown with faint birdseye extinction. Occasional skeletal, tabular grains with Fe-Ti oxide and apatite inclusions.
tr.	Apatite	Acicular inclusions in other phases, primarily feldspar.

Silicate veinlets in groundmass cross-cut feldspar and augite microphenocrysts, as well as the glomerocryst. Were microphenocrysts have been broken, extinction domains are the same on either side of veinlets. These veinlets consist primarily of sericite and sericitized feldspar with occasional isolated augite microphenocrysts included. Immediately adjacent rock exhibits no more alteration than that farther removed.

950318-8C1

Tejana Mesa wall rock-vein contact.

Wall rock phenocrysts (≥200 μm):

Mode %	Phase	Description
10	Fe-Ti oxides	Subhedral to anhedral ≤250 μm grains, some with margins altered to limonite.
10	Iddingsite	Pseudomorphic alteration products of olivine (and augite?), some with fractures interpreted to be relict from original minerals.
1	Titanaugite	≤500 μm, concentric zonation, typically twinned lengthwise, most are fractured. Inclusions of opaques and iddingsite.
1	Olivine	≤300 μm grains with margins replaced by iddingsite. Some grains contain silicate inclusions that exhibit weak shape-preferred orientation.

Wall rock groundmass (≤200 μm):

Mode %	Phase	Description
64	Augite	≤100 μm, straight grain boundaries. Some twinned grains.
6	Alkali feldspar	Anhedral, colorless, biaxial interference figures, occasional twinning and undulose extinction. Microprobe analyses indicate that tartan-twinned, subtabular grains are Ba-rich ($Cs_{0.9}$ to $Cs_{8.2}$) anorthoclase (<Or_{37}). These grains have rounded, embayed margins.
6	Sericite & clay	Very fine-grained.
2	Analcime	Nearly isotropic, colorless.
tr.	Biotite	Tabular to skeletal. No observed association with other mafic phases.
tr.	Apatite	Acicular inclusions in felsic groundmass phases.

Wall rock phenocrysts and microphenocrysts exhibit shape preferred orientation inclined ~30° to 40° counterclockwise from long edge of thin section.

Vein:

Mode %	Phase	Description
30	Alkali feldspar	Biaxial (-), δ≤0.009, 2V≅60°. Twinned lengthwise, sometimes with pericline twinning crosswise. Skeletal, sub-tabular, undulose extinction. Also occurs as occasional small, radial, spherulitic (Fig. 6E) and spherulitic closed, fine (Fig. 6F) blades. Most grains are extensively altered to sericite and clay, and some have Fe-Ti inclusions. Apatite and opaque inclusions are common. Smaller grains form part of groundmass.
23	Zeolite(?) & clay	Very fine-grained groundmass phases.
20	Titanaugite	≤3 mm long. Occurs as larger grains in the vein proper and as smaller, inhomogeneously-nucleated grains on the wall rock margin. Most grains are skeletal, prismatic-skeletal or dendritic-skeletal, twinned, fractured, and have abundant opaque phases, including Fe-Ti oxides around their margins. The larger, more euhedral grains in the vein proper appear to have reacted with the melt to form Fe-Ti oxides and fine-grained uralite(?) and sericite. Some Fe-Ti oxides have reddish-orange, fine-grained limonite around their margins. Centimeter scale masses of dendritic titanaugite, Fe-Ti oxides, and fine-grained, colorless sericite are all that are left of some crystals.
15	Fe-Ti oxides	<1 cm. Euhedral to anhedral. Larger grains often exhibit hopper texture. Limonite alteration around margins of many grains.
10	Nephelene	Uniaxial (-), δ≤0.009. No twinning, undulose extinction.
2	Analcime	Nearly isotropic, colorless. Confined to vein-wall rock interface.
tr.	Biotite	Tabular to skeletal. No observed association with other mafic phases.
tr.	Augite	≤200 μm, anhedral, green. Grains are usually associated with sericite.
tr.	Apatite	Acicular inclusions in most other phases.

No shape-preferred orientation of grains or other flow direction indicators were observed in the vein. Wall rock fragments >1 cm in vein. Augite microphenocrysts in wall rock fragments often have rounded ends, somewhat curved sides, opaque inclusions and opaques concentrated along margins, similar to augite phenocrysts in vein.

950318-8C2

Thin section cut ⊥ to -8C1.

Wall rock phenocrysts (≥200 μm):

Mode %	Phase	Description
10	Iddingsite	≤500 μm. Pseudomorphic alteration products of olivine (and augite?), some with fractures interpreted to be relict from original minerals.
7	Fe-Ti oxides	Generally anhedral, ≤500 μm; some grains with margins altered to limonite. Most grains associated with altered olivine and augite.
2	Titanaugite	≤500 μm, anhedral to subhedral, concentric zonation, typically twinned lengthwise, most are fractured. Grain margins are irregular, fractured into small fragments, but not extensively altered chemically, except for limonite/iddingsite patches. Some very small (≤10μm) anhedral to euhedral Fe-Ti inclusions, most of which exhibit no exsolution lamellae visible with ×50 objective. Fluid(?) inclusions concentrated in concentric growth rings.
1	Olivine	≤300 μm grains with margins replaced by iddingsite and Fe-Ti oxides. Some grains contain silicate inclusions that exhibit weak shape-preferred orientation.

Wall rock groundmass (≤200 μm):

Mode %	Phase	Description
64	Augite	≤100 μm, tablets with straight grain boundaries. Some twinned grains.
8	Alkali feldspar	Interstitial, anhedral, colorless, biaxial interference figures, occasional twinning and undulose extinction. Some alteration to sericite.
4	Analcime	Nearly isotropic, colorless.
4	Fe-Ti oxides	Euhedral to subhedral grains. Some exhibit limonite alteration around margins.
tr.	Apatite	Acicular inclusions in alkali feldspar and analcime.
tr.	Nepheline	Isolated uniaxial grains in analcime.

Vein:

Mode %	Phase	Description
35	Alkali feldspar	Biaxial (-), $\delta \leq 0.009$, $2V \cong 60°$. Twinned lengthwise, sometimes with pericline twinning crosswise. Skeletal, sub-tabular, undulose extinction. Also occurs as occasional small, radial, spherulitic (Fig. 6E) and spherulitic closed, fine (Fig. 6F) blades. Most grains are extensively altered to sericite and clay, and some have Fe-Ti inclusions. Apatite and opaque inclusions are common. Smaller grains form part of groundmass.
20	Zeolite(?) & clay	Very fine-grained groundmass phases.
15	Titanaugite	≤3 mm long. Occurs as larger grains in the vein proper and as smaller, inhomogeneously nucleated grains on the wall rock margin. Most grains are skeletal, prismatic-skeletal or dendritic-skeletal, twinned, fractured, and have abundant opaque phases, including Fe-Ti oxides around their margins. The larger, more euhedral grains in the vein proper appear to have reacted with the melt to form Fe-Ti oxides and fine-grained chlorite, clay, sericite, and green augite. Some Fe-Ti oxides have reddish-orange, fine-grained limonite around their margins. Centimeter scale masses of dendritic titanaugite, Fe-Ti oxides, and fine-grained, colorless sericite are all that are left of some crystals.
15	Fe-Ti oxides	<1 cm. Euhedral to anhedral. Larger grains often exhibit hopper texture. Limonite alteration around margins of many grains. Also occurs as acicular, vermicular, and radiating grains and masses.
8	Nephelene	Uniaxial (-), $\delta \leq 0.009$. No twinning, undulose extinction.
5	Stilbite	Crack-filling, fan-spherulitic, colorless masses.
2	Analcime	Nearly isotropic, colorless. Not necessarily confined to vein-wall rock interface.
tr.	Apatite	Acicular grains found primarily included in feldspar and sericite masses; some are partially enclosed by titanaugite.
tr.	Augite	≤200 μm, anhedral, green. Grains are usually associated with sericite.
tr.	Apatite	Acicular inclusions in most other phases.

No shape-preferred orientation of grains, or other flow direction indicators were observed. Wall rock fragments, >1 cm across and similar in mineralogy to the adjacent wall rock except for more extensive alteration, are found in vein.

950423-15.1

Horizontal, 1.25 m thick, medium-grained vein ~8 m below top of east face of El Porticito. No wall rock is included in this thin section.

Vein:

Mode %	Phase	Description
35	Alkali feldspar	Morphologies similar to those of 941214-1A & -1B veins. No tartan twinning observed in tabular grains. Some large grains are skeletal.
35	Titanaugite	≤4 mm. Tabular to bladed, subhedral to euhedral, brownish-purple. Most are fractured and have undergone varying degrees of alteration to Fe-Ti oxides, clay, and chlorite. Some grains include hopper-textured Fe-Ti oxide crystals. Titanaugite and alkali feldspar are sometimes intergrown.
16	Fe-Ti oxides	≤1.2 mm. Occur as alteration phase of titanaugite and as phenocrystic grains, sometimes exhibiting hopper texture. Some grains partially altered, surrounded by limonite.
8	Analcime	$\delta \approx 0$. Low relief. Irregular masses with abundant inclusions of Fe-Ti oxides, apatite, and feldspar.
5	Stilbite	In groundmass. Radiating bundles, low negative relief, $\delta \approx 0.007$. Occasional 'bow tie' morphology.
1	Hematite	Replacement product of Fe-Ti oxides, sometimes exhibiting hopper texture.
tr.	Apatite	Acicular grains included in most other phases except fan spherulitic and skeletal feldspars.
tr.	Augite	Occurs as isolated grains and near margins of titanaugite, of which it may be an alteration product. Some apatite inclusions
tr.	Sericite	Alteration product of feldspar.
tr.	Limonite	Occurs as small, isolated masses and around margins of Fe-Ti oxides

This section includes a grain that was originally >2.5 cm long and ~1 mm wide. The grain has been completely replaced by Fe-Ti oxides, feldspar, sericite, limonite, and clay. Similar grains have been observed occasionally in outcrop and hand specimen in various veins of El Porticito. The original phase has not been determined.

950515-19A1

El Porticito early basanite phenocrysts . No vein is included in this thin section.

Lava phenocrysts (≥200 μm):

Mode %	Phase	Description
16	Olivine	≤3 mm anhedral to subhedral, fractured. Many fractures filled with very fine-grained greenish chlorophaeite. Margins sometimes surrounded by Fe-Ti oxides.
2	Augite	≤3 mm. Subhedral, usually twinned and fractured, colorless to beige. Some exhibit faint concentric zoning, with central and outermost zones containing fine-grained Fe-Ti oxide and other inclusions.
2	Fe-Ti oxides	All grains are anhedral.
tr.	Plagioclase	One corroded, originally euhedral grain with first order birefringence, polysynthetic twinning, and undulose extinction observed. Composition is ~An_{60} (angle between extinctions is between 31° and 37°). Birefringence pattern suggestsconcentric compositional zonation.

Lava groundmass (≤200 μm):

Mode %	Phase	Description
68	Augite	≤50 μm long × ≤15 μm wide, greenish-yellow tablets with slightly lobate grain boundaries. Crystals tend to be aligned around sides of phenocrysts of augite and olivine, as though flowing around them.
8	Fe-Ti oxides	Generally irregularly shaped masses consisting of gray, metallic (magnetite?) centers surrounded by dull black material. Occasional subhedral to euhedral grains.
3	Interstitial phase(s)	1st order birefringent, anhedral grains, some with undulose extinction (probably feldspar). Some contain abundant, very fine-grained inclusions. Also orange clay masses that have a waxy luster.
1	Olivine	Anhedral microphenocrysts.
tr.	Analcime	Colorless, isotropic.
tr.	Calcite	Interspersed with interstitial phases.

950515-21.1

Horizontal, ~1m thick, fine-grained vein 1.5m below top of El Porticito. No wallrock is included in this thin section.

Vein:

Mode %	Phase	Description
25	Alkali feldspar	Biaxial (-), 2V≅50°, δ≅0.007, tabular, low relief, some concentrically zoned. Also finer-grained, bladed, skeletal, radiating, twinned grains, similar to those in -1A.
25	Stilbite	In groundmass. Radiating bundles, low negative relief, δ ≈ 0.007.
20	Titanaugite	≤2 mm long; most <1 mm. Tabular to bladed, subhedral to euhedral, some skeletal, brownish-purple, usually twinned par allel to long axis, sometimes glomeromorphic. Most are fractured and have undergone varying degrees of alteration to Fe-Ti oxides, clay, chlorite, and occasionally biotite. Some are al most completely replaced.
11	Analcime	δ ≈ 0, uniaxial when interference figure is observed, low negative relief. Occurs as masses ≤5 mm across with abundant inclusions, including Fe-Ti oxides and hematite.
10	Fe-Ti oxides	≤1 mm. Occur as anhedral to subhedral alteration phase of titanaugite and as phenocrystic grains, sometimes exhibiting hopper texture. Some grains partially altered, surrounded by limonite. Inclusions in hopper voids are primarily analcime.
6	Sericite	Fibrous, colorless groundmass phase.
3	Nepheline	Uniaxial (-), anhedral, highly fractured. Some pyroxene inclusions and zeolite inclusions/alteration products.
tr.	Apatite	Acicular, very thin (≤20 μm), hexagonal basal sections, color less to brownish, medium to high positive relief, parallel extinction, length fast.
tr.	Augite	≤50 μm, anhedral, pleochroic green, inclined extinction.
tr.	Limonite	Occurs as small, isolated masses and around margins of Fe-Ti oxides

950522-27D

Amygdaloidal bomb from thick, coarse-grained, structureless layer near base of phreatomagmatic deposit at southeast corner of Tejana Mesa.

Phenocrysts:

Mode %	Phase	Description
23	Augite	≤500 μm, euhedral to subhedral, usually colorless, fractured, seldom twinned, not zoned. Margins (≤100 μm deep) and some interiors corroded, with alteration product of fine-grained uralite.
11	Olivine	≤300 μm, euhedral to subhedral, fractured. Some grains exhibit iddingsite alteration around margins.
8	Calcite	Filling cracks and subrounded to elongate amygdules.
3	Clay	Orange, very fine-grained, waxy luster. Shares void-filling role with calcite.
1	Feldspar	≤2 mm, euhedral, biaxial, not twinned. (Only semirandom sections observed; this phase not probed)

In reflected light the groundmass is seen to consist of ≤5 μm euhedral to anhedral Fe-Ti oxide grains and ≤40 μm tabular to subequant pyroxene(?) crystals set in an opaque, glassy matrix. Some, but not all, oxide grains exhibit exsolution blebs and concentric zones. Amygdules found in groundmass range in size to ~2 mm.

APPENDIX C: Whole Rock Compositions

Element	c.v.	a.m.	27C	27D	49E	19A	20	25A	28	29	39AB
				Tp				Tepb1			
wt%:											
SiO2	0.4	XRF	39.93	40.50	41.63	42.05	41.57	41.59	42.49	42.55	42.32
TiO2	1.3	XRF	2.78	2.78	2.67	2.90	2.96	2.90	2.89	2.98	2.85
Al2O3	0.4	XRF	8.41	8.55	8.62	8.80	8.71	9.04	8.91	9.09	8.99
Fe2O3	1.3	XRF	12.00	11.95	11.81	12.69	12.68	12.45	12.60	12.75	12.54
MnO	1.4	XRF	0.17	0.17	0.16	0.18	0.17	0.17	0.18	0.19	0.18
MgO	1.4	XRF	13.71	13.50	11.13	14.36	14.13	13.86	13.63	13.65	13.68
CaO	1.0	XRF	14.98	14.37	14.41	12.87	13.17	12.75	12.35	12.67	12.41
Na2O	0.7	XRF	2.12	2.86	1.99	2.34	1.92	1.95	3.44	3.62	3.08
K2O	0.9	XRF	0.35	0.39	0.56	1.00	0.56	0.78	1.01	0.49	1.04
P2O5	1.3	XRF	0.89	0.88	0.85	0.91	0.95	0.93	0.93	0.97	0.90
LOI	1.9	Grav	4.27	3.26	5.36	1.57	3.29	3.15	0.60	1.08	0.98
Total			99.61	99.21	99.19	99.67	100.13	99.56	99.04	100.05	98.97
ppm:	c.v. / d.l.										
V	6 / 2	XRF	226	231	274	250	232	250	246	249	251
Sc	1 / 2	INAA	23.2	23.4	22.3	24.1	23.9	n.a.	n.a.	24.1	24.1
Cr	5 / 2	INAA	708	714	684	710	689	n.a.	n.a.	697	704
Ni	12 /2	XRF	433	423	414	391	379	374	396	389	392
Cu	17 / 2	XRF	82	80	69	84	77	91	82	73	86
Zn	2 / 2	XRF	115	114	113	107	104	103	109	106	109
Ga	3 / 2	XRF	15	15	15	17	16	17	17	19	18
As	23 / 3	INAA	n.d.	n.d.	18	n.d.	n.a.	n.a.	n.a.	n.d.	n.d.
Rb	1 / 2	XRF	13.0	12.1	52.4	16.5	26.1	23.4	20.1	15.6	21.2
Sr	1 / 2	XRF	1242	931	1016	1126	1158	1308	1062	1070	1099
Y	8 / 2	XRF	24	25	23	25	25	25	26	26	26
Zr	3 / 2	XRF	239	240	231	248	248	247	252	256	253
Nb	8 / 2	XRF	74	74	70	72	71	73	75	74	75
Mo	55 / 2	XRF	n.d.	n.d.	n.d.	n.d.	n.d.	n.d.	n.d.	n.d.	n.d.
Sb	14 / 2	INAA	n.d.	0.04	0.03	0.07	n.d.	n.a.	n.a.	0.06	n.d.
Cs	2 / 2	INAA	4.51	4.17	5.07	n.d.	n.d.	n.a.	n.a.	n.d.	n.d.
Ba	2 / 2	XRF	1040	932	1498	1300	1447	1475	1295	1370	1342
La	2 / 2	INAA	72.7	73.2	69.8	74.9	75.0	n.a.	n.a.	78.6	76.3
Ce	1 / 2	INAA	141	142	133	143	144	n.a.	n.a.	150	146
Nd	4 / 2	INAA	55	54	54	57	58	n.a.	n.a.	66	55
Sm	2 / 2	INAA	11.1	11.0	10.7	11.8	12.1	n.a.	n.a.	11.8	11.5
Eu	2 / 2	INAA	3.12	3.17	2.98	3.26	3.23	n.a.	n.a.	3.36	3.24
Tb	3 / 2	INAA	1.12	1.09	1.10	1.22	1.13	n.a.	n.a.	1.17	1.11
Yb	3 / 2	INAA	1.53	1.40	1.36	1.45	1.43	n.a.	n.a.	1.52	1.48
Lu	3 / 2	INAA	0.196	0.167	0.196	0.203	0.207	n.a.	n.a.	0.175	0.165
Hf	3 / 2	INAA	5.68	5.69	5.60	6.06	5.94	n.a.	n.a.	5.92	6.14
Ta	2 / 2	INAA	4.13	4.17	3.95	4.20	4.21	n.a.	n.a.	4.36	4.19
Pb	9 / 2	XRF	6	5	6	8	5	9	6	6	7
Th	2 / 2	INAA	14.2	14.0	13.4	13.8	14.1	n.a.	n.a.	14.8	14.5
U	10 / 2	INAA	n.d.	n.d.	n.d.	n.d.	n.d.	n.a.	n.a.	n.d.	n.d.
Au	2 / 0.3	FA	n.a.	n.a.	n.a.	n.a.	n.a.	n.a.	n.a.	n.a.	n.a.
Ag	2 / 3	FA	n.a.	n.a.	n.a.	n.a.	n.a.	n.a.	n.a.	n.a.	n.a.
$^{143}Nd/^{144}Nd$		MS	n.a.	n.a.	n.a.	0.512802	n.a.	n.a.	n.a.	n.a.	n.a.

c.v. / d.l.: Estimated precisions (coefficients of variation (%)) / detection limits (ppm)
For XRF measurements, 17 aliquots of in-house reference NMR were analysed to obtain the listed coefficients of variation.
For INAA measurements, 28 aliquots of BCR-1 and 31 aliquots of G-2 USGS standards were analysed.
For gravimetric measurements, 9 aliquots of sample 7A were analysed.

a.m.: analysis method
XRF: wavelength dispersive X-ray fluorescence
INAA: instrumental neutron activation analysis
FA: fire assay (Precisions and detection limits provided by A. Gundiler, personal communication.)
Grav: gravimetric
MS: mass spectroscopy. Data normalized to 146Nd/144Nd=0.7219; 143Nd/144Nd precision to +/- 0.000010

n.a.: not analyzed

n.d.: below detection limit

APPENDIX C: Whole Rock Compositions

Element	49F	55	6B1	7B	8B	11B	19B	23C	24	25C
	Tepb1		Tepb2							
wt%:										
SiO2	43.28	42.11	42.19	42.26	42.14	42.31	42.78	42.07	42.19	41.77
TiO2	2.91	2.92	3.13	3.14	3.16	3.18	3.17	3.21	3.11	3.08
Al2O3	8.93	9.09	11.48	11.29	11.08	11.22	11.38	11.04	10.54	10.89
Fe2O3	12.71	12.69	12.39	12.42	12.51	12.77	13.07	12.97	12.66	12.51
MnO	0.17	0.19	0.18	0.18	0.18	0.18	0.19	0.18	0.18	0.18
MgO	13.65	13.08	10.07	10.09	10.51	10.23	10.64	10.10	11.56	10.80
CaO	12.33	13.05	12.48	12.62	12.72	12.42	12.94	11.90	12.32	12.37
Na2O	3.16	3.66	2.44	2.54	2.23	2.96	3.19	3.69	2.84	2.66
K2O	0.94	0.59	0.98	0.95	0.96	0.94	0.89	1.11	0.89	0.99
P2O5	0.93	0.94	1.00	0.99	1.01	0.99	1.02	1.01	0.98	0.98
LOI	0.74	1.27	3.53	3.46	2.91	2.64	2.76	2.70	2.53	3.00
Total	99.76	99.58	99.87	99.93	99.42	99.83	102.03	99.98	99.80	99.23
ppm:										
V	260	260	248	254	256	249	247	258	261	275
Sc	23.9	23.9	n.a.	n.a.	n.a.	n.a.	19.9	n.a.	n.a.	n.a.
Cr	693	672	n.a.	n.a.	n.a.	n.a.	371	n.a.	n.a.	n.a.
Ni	408	385	216	215	220	220	224	210	278	252
Cu	73	80	101	109	98	101	98	136	96	100
Zn	113	110	98	107	99	102	101	104	104	105
Ga	18	18	18	20	18	19	20	19	19	19
As	n.d.	n.d.	n.a.	n.a.	n.a.	n.a.	n.d.	n.a.	n.a.	n.a.
Rb	13.3	6.4	34.2	32.3	28.9	29.2	31.6	51.9	18.0	25.4
Sr	1093	1094	1466	1543	1331	1371	1155	1401	1655	1326
Y	26	25	28	28	28	28	28	29	28	28
Zr	254	254	263	266	264	265	269	266	261	266
Nb	76	74	74	78	74	77	77	74	75	80
Mo	2.1	n.d.	n.d.	2.2	2.0	2.0	2.2	2.2	2.6	n.d.
Sb	n.d.	n.d.	n.a.	n.a.	n.a.	n.a.	n.d.	n.a.	n.a.	n.a.
Cs	n.d.	n.d.	n.a.	n.a.	n.a.	n.a.	n.d.	n.a.	n.a.	n.a.
Ba	1354	1342	1761	1829	1734	1766	1664	1706	1668	1684
La	77.4	78.2	n.a.	n.a.	n.a.	n.a.	82.0	n.a.	n.a.	n.a.
Ce	149	149	n.a.	n.a.	n.a.	n.a.	158	n.a.	n.a.	n.a.
Nd	65	60	n.a.	n.a.	n.a.	n.a.	63	n.a.	n.a.	n.a.
Sm	11.6	12.6	n.a.	n.a.	n.a.	n.a.	12.3	n.a.	n.a.	n.a.
Eu	3.32	3.31	n.a.	n.a.	n.a.	n.a.	3.52	n.a.	n.a.	n.a.
Tb	1.19	1.21	n.a.	n.a.	n.a.	n.a.	1.22	n.a.	n.a.	n.a.
Yb	1.53	1.42	n.a.	n.a.	n.a.	n.a.	1.79	n.a.	n.a.	n.a.
Lu	0.182	0.179	n.a.	n.a.	n.a.	n.a.	0.219	n.a.	n.a.	n.a.
Hf	5.87	6.12	n.a.	n.a.	n.a.	n.a.	6.26	n.a.	n.a.	n.a.
Ta	4.32	4.39	n.a.	n.a.	n.a.	n.a.	4.63	n.a.	n.a.	n.a.
Pb	6	8	7	7	7	7	8	6	8	7
Th	14.7	14.2	n.a.	n.a.	n.a.	n.a.	16.0	n.a.	n.a.	n.a.
U	n.d.	n.d.	n.a.	n.a.	n.a.	n.a.	n.d.	n.a.	n.a.	n.a.
Au	n.a.	n.a.	n.a.	n.a.	n.a.	n.a.	n.a.	n.a.	n.a.	n.a.
Ag	n.a.	n.a.	n.a.	n.a.	n.a.	n.a.	n.a.	n.a.	n.a.	n.a.
$^{143}Nd/^{144}Nd$	n.a.	n.a.	n.a.	n.a.	n.a.	n.a.	0.512803	n.a.	n.a.	n.a.

APPENDIX C: Whole Rock Compositions

Element	37A	37F	37G	37K	44F	56	58	NM1104av	2	6A2
					Tepb2				Tepv	
wt%:										
SiO2	42.25	41.68	41.93	41.64	41.33	42.87	42.44	41.68	46.57	45.95
TiO2	3.14	3.11	3.14	3.11	3.13	3.15	3.11	3.18	2.60	2.62
Al2O3	11.41	11.02	11.13	11.07	10.78	11.26	10.71	10.85	16.78	16.89
Fe2O3	12.71	12.64	12.78	12.65	12.78	12.78	12.77	12.78	9.06	8.98
MnO	0.18	0.18	0.18	0.18	0.18	0.19	0.18	0.19	0.15	0.15
MgO	9.85	10.12	9.98	10.15	10.46	9.50	10.79	10.36	3.01	3.44
CaO	12.28	12.27	12.59	12.61	12.70	12.54	12.65	12.03	7.89	9.00
Na2O	2.78	2.55	2.73	2.59	2.44	4.03	2.42	4.00	3.72	4.70
K2O	1.07	1.09	0.88	0.91	0.82	0.93	0.98	0.90	4.05	3.31
P2O5	0.97	0.94	0.97	0.96	0.99	1.00	0.99	0.97	0.95	1.25
LOI	3.13	3.27	3.49	3.23	3.09	1.23	2.78	2.53	3.73	3.48
Total	99.78	98.87	99.81	99.09	98.69	99.48	99.82	99.47	98.51	99.76
ppm:										
V	248	255	250	252	267	283	270	248	131	135
Sc	n.a.	n.a.	19.4	n.a.	20.3	19.8	20.4	20.8	n.a.	n.a.
Cr	n.a.	n.a.	363	n.a.	390	367	425	385	n.a.	n.a.
Ni	218	225	218	222	232	233	274	201	17	30
Cu	112	118	120	120	100	98	93	91	136	164
Zn	108	109	110	107	107	116	117	93	94	88
Ga	21	20	21	20	20	21	19	18	22	20
As	n.a.	n.a.	n.d.	n.a.	n.d.	n.d.	n.d.	n.a.	n.a.	n.a.
Rb	49.9	56.9	57.5	51.9	22.4	17.0	30.5	48.0	120	78.7
Sr	1390	1489	1168	1344	1376	1228	1405	1368	3941	2206
Y	29	29	27	27	28	29	27	28	29	34
Zr	266	263	264	260	259	274	262	266	331	350
Nb	78	77	77	74	73	83	81	71	147	149
Mo	n.d.	n.d.	n.d.	n.d.	n.d.	n.d.	n.d.	n.a.	2.8	3.3
Sb	n.a.	n.a.	0.05	n.a.	0.09	0.04	n.d.	0.05	n.a.	n.a.
Cs	n.a.	n.a.	n.d.	n.a.	n.d.	n.d.	n.d.	n.d.	n.a.	n.a.
Ba	1894	1866	1710	1690	1662	1552	1555	1727	4014	3344
La	n.a.	n.a.	81.9	n.a.	82.5	84.2	82.4	79.4	n.a.	n.a.
Ce	n.a.	n.a.	156	n.a.	158	161	157	154	n.a.	n.a.
Nd	n.a.	n.a.	66	n.a.	65	61	55	63	n.a.	n.a.
Sm	n.a.	n.a.	12.1	n.a.	13.1	12.5	12.2	12.3	n.a.	n.a.
Eu	n.a.	n.a.	3.44	n.a.	3.52	3.52	3.36	3.50	n.a.	n.a.
Tb	n.a.	n.a.	1.18	n.a.	1.19	1.20	1.31	1.15	n.a.	n.a.
Yb	n.a.	n.a.	1.84	n.a.	1.61	1.73	1.44	1.69	n.a.	n.a.
Lu	n.a.	n.a.	0.207	n.a.	0.214	0.238	0.201	0.194	n.a.	n.a.
Hf	n.a.	n.a.	6.25	n.a.	6.46	6.50	6.31	6.36	n.a.	n.a.
Ta	n.a.	n.a.	4.76	n.a.	4.47	4.80	4.60	4.45	n.a.	n.a.
Pb	6	6	8	7	7	8	8	7	16	11
Th	n.a.	n.a.	15.8	n.a.	15.3	16.5	15.9	15.0	n.a.	n.a.
U	n.a.	n.a.	n.d.	n.a.	n.d.	n.d.	n.d.	4.4	n.a.	n.a.
Au	n.a.	n.a.	n.a.	n.a.	n.a.	n.a.	n.a.	n.a.	n.a.	n.a.
Ag	n.a.	n.a.	n.a.	n.a.	n.a.	n.a.	n.a.	n.a.	n.a.	n.a.
$^{143}Nd/^{144}Nd$	n.a.	n.a.	n.a.	n.a.	n.a.	n.a.	n.a.	n.a.	n.a.	n.a.

APPENDIX C: Whole Rock Compositions

Element	7A	8A	15	21	23B	25B	37B	37C	37D	37E
wt%:					Tepv					
SiO2	46.27	44.87	43.50	44.42	41.73	41.91	44.87	44.62	44.76	43.12
TiO2	2.56	2.94	3.26	2.85	3.92	3.38	2.72	2.69	2.80	3.03
Al2O3	17.67	16.50	15.27	16.13	14.43	14.00	17.61	17.38	16.78	16.43
Fe2O3	8.91	9.75	11.07	10.03	12.75	11.10	10.01	9.86	9.59	10.03
MnO	0.15	0.17	0.18	0.17	0.18	0.17	0.17	0.17	0.16	0.16
MgO	2.98	3.83	4.04	3.71	5.03	5.19	3.09	3.07	3.34	3.70
CaO	8.25	8.83	11.01	9.95	10.94	12.09	7.14	7.14	8.06	8.89
Na2O	4.61	3.69	2.98	3.45	2.65	2.44	6.59	6.50	6.08	6.33
K2O	3.62	3.74	2.95	3.23	2.72	2.20	2.70	2.89	2.86	2.24
P2O5	1.02	1.17	1.47	1.28	1.68	1.70	1.19	1.16	1.23	1.42
LOI	3.21	3.45	4.55	4.23	3.33	4.55	3.40	3.54	3.29	3.18
Total	99.25	98.93	100.28	99.46	99.36	98.73	99.47	99.03	98.95	98.52
ppm:										
V	129	177	200	156	296	268	153	155	172	201
Sc	n.a.	n.a.	5.1	3.8	n.a.	8.5	n.a.	2.5	n.a.	n.a.
Cr	n.a.	n.a.	n.d.	n.d.	n.a.	32	n.a.	n.d.	n.a.	n.a.
Ni	21	18	33	27	57	52	27	24	30	37
Cu	159	216	181	166	210	181	152	158	156	138
Zn	99	92	111	100	102	98	114	124	107	108
Ga	21	23	18	22	22	20	20	21	19	21
As	n.a.	n.a.	n.d.	n.d.	n.a.	5	n.a.	n.d.	n.a.	n.a.
Rb	82.2	92.9	96.5	69.1	73.5	44.1	54.6	58.5	52.0	30.6
Sr	2758	2693	2315	2281	2949	2119	2385	2319	2262	1975
Y	32	33	33	33	36	36	32	34	34	36
Zr	341	344	320	319	325	332	313	341	330	331
Nb	150	143	122	133	112	125	142	160	142	138
Mo	3.5	4.0	3.3	3.5	3.2	3.4	2.4	2.9	3.3	2.7
Sb	n.a.	n.a.	n.d.	0.11	n.a.	0.10	n.a.	0.20	n.a.	n.a.
Cs	n.a.	n.a.	n.d.	n.d.	n.a.	n.d.	n.a.	n.d.	n.a.	n.a.
Ba	3779	3294	3108	3356	2608	2800	3386	3373	3206	2560
La	n.a.	n.a.	128	127	n.a.	137	n.a.	135	n.a.	n.a.
Ce	n.a.	n.a.	237	231	n.a.	253	n.a.	240	n.a.	n.a.
Nd	n.a.	n.a.	88	88	n.a.	101	n.a.	89	n.a.	n.a.
Sm	n.a.	n.a.	15.7	14.7	n.a.	17.2	n.a.	14.4	n.a.	n.a.
Eu	n.a.	n.a.	4.28	4.05	n.a.	4.78	n.a.	4.09	n.a.	n.a.
Tb	n.a.	n.a.	1.42	1.36	n.a.	1.59	n.a.	1.35	n.a.	n.a.
Yb	n.a.	n.a.	2.30	2.22	n.a.	2.28	n.a.	2.20	n.a.	n.a.
Lu	n.a.	n.a.	0.267	0.269	n.a.	0.274	n.a.	0.301	n.a.	n.a.
Hf	n.a.	n.a.	6.33	6.14	n.a.	6.94	n.a.	6.17	n.a.	n.a.
Ta	n.a.	n.a.	7.76	7.94	n.a.	7.97	n.a.	8.96	n.a.	n.a.
Pb	15	11	14	12	12	11	14	16	14	11
Th	n.a.	n.a.	26.1	28.1	n.a.	28.5	n.a.	31.8	n.a.	n.a.
U	n.a.	n.a.	n.d.	n.d.	n.a.	n.d.	n.a.	n.d.	n.a.	n.a.
Au	n.a.	n.a.	n.a.	n.a.	n.a.	n.a.	n.a.	n.a.	n.a.	n.a.
Ag	n.a.	n.a.	n.a.	n.a.	n.a.	n.a.	n.a.	n.a.	n.a.	n.a.
$^{143}Nd/^{144}Nd$	n.a.	n.a.	n.a.	n.a.	n.a.	n.a.	n.a.	n.a.	n.a.	n.a.

APPENDIX C: Whole Rock Compositions

	37H	37I	37J	41A	41B	42	43A	43B	43C	43D
Element					Tepv					
wt%:										
SiO2	44.90	44.71	43.71	44.32	44.21	44.74	44.81	45.33	44.16	44.22
TiO2	2.76	2.97	3.01	2.81	2.68	2.83	2.71	2.67	2.99	3.03
Al2O3	16.92	16.54	15.98	16.29	16.14	16.06	16.42	16.58	15.76	15.84
Fe2O3	9.66	10.27	10.26	9.81	9.53	9.87	9.59	9.76	10.03	10.30
MnO	0.16	0.17	0.17	0.17	0.16	0.18	0.17	0.17	0.17	0.18
MgO	3.21	3.47	3.97	3.51	3.41	3.74	3.60	3.27	3.71	3.97
CaO	8.42	9.16	9.76	9.15	9.12	8.89	9.13	9.32	9.99	10.22
Na2O	5.30	4.58	4.72	3.82	3.69	4.74	3.97	3.09	3.83	3.71
K2O	3.03	3.12	2.77	3.27	3.37	3.45	3.64	3.59	3.70	3.85
P2O5	1.11	1.25	1.37	1.23	1.26	1.38	1.28	1.25	1.41	1.54
LOI	3.34	3.21	3.05	5.02	5.11	2.30	3.23	3.83	2.43	2.25
Total	98.82	99.44	98.76	99.40	98.68	98.19	98.54	98.86	98.18	99.12
ppm:										
V	150	173	196	146	148	185	162	154	212	206
Sc	n.a.	n.a.	4.8	n.a.	n.a.	4.1	n.a.	n.a.	n.a.	n.a.
Cr	n.a.	n.a.	n.d.	n.a.	n.a.	n.d.	n.a.	n.a.	n.a.	n.a.
Ni	25	28	36	27	28	38	32	27	39	40
Cu	144	155	145	179	167	158	154	161	153	172
Zn	103	106	104	101	98	103	100	111	104	106
Ga	20	18	19	19	18	24	22	21	24	23
As	n.a.	n.a.	n.d.	n.a.	n.a.	n.d.	n.a.	n.a.	n.a.	n.a.
Rb	70.1	84.2	68.8	135	128	77.4	94.7	89.5	79.1	101
Sr	2102	2326	2116	2140	2235	2680	2711	3916	3033	2422
Y	34	32	34	33	33	34	33	30	35	35
Zr	339	316	330	313	315	313	321	304	312	318
Nb	146	133	128	129	133	123	132	134	124	127
Mo	3.0	2.8	2.9	2.3	2.6	2.3	2.4	2.7	n.d.	3.9
Sb	n.a.	n.a.	n.d.	n.a.	n.a.	0.10	n.a.	n.a.	n.a.	n.a.
Cs	n.a.	n.a.	n.d.	n.a.	n.a.	n.d.	n.a.	n.a.	n.a.	n.a.
Ba	3308	3279	3093	3627	3945	3434	3448	3346	3352	3231
La	n.a.	n.a.	128	n.a.	n.a.	130	n.a.	n.a.	n.a.	n.a.
Ce	n.a.	n.a.	237	n.a.	n.a.	237	n.a.	n.a.	n.a.	n.a.
Nd	n.a.	n.a.	88	n.a.	n.a.	95	n.a.	n.a.	n.a.	n.a.
Sm	n.a.	n.a.	15.7	n.a.	n.a.	15.5	n.a.	n.a.	n.a.	n.a.
Eu	n.a.	n.a.	4.35	n.a.	n.a.	4.38	n.a.	n.a.	n.a.	n.a.
Tb	n.a.	n.a.	1.43	n.a.	n.a.	1.39	n.a.	n.a.	n.a.	n.a.
Yb	n.a.	n.a.	2.16	n.a.	n.a.	2.20	n.a.	n.a.	n.a.	n.a.
Lu	n.a.	n.a.	0.265	n.a.	n.a.	0.275	n.a.	n.a.	n.a.	n.a.
Hf	n.a.	n.a.	6.37	n.a.	n.a.	6.27	n.a.	n.a.	n.a.	n.a.
Ta	n.a.	n.a.	7.76	n.a.	n.a.	7.60	n.a.	n.a.	n.a.	n.a.
Pb	13	10	12	11	9	11	10	15	12	12
Th	n.a.	n.a.	26.7	n.a.	n.a.	25.7	n.a.	n.a.	n.a.	n.a.
U	n.a.	n.a.	n.d.	n.a.	n.a.	n.d.	n.a.	n.a.	n.a.	n.a.
Au	n.a.	n.a.	n.a.	n.a.	n.a.	n.a.	n.a.	n.a.	n.a.	n.a.
Ag	n.a.	n.a.	n.a.	n.a.	n.a.	n.a.	n.a.	n.a.	n.a.	n.a.
$^{143}Nd/^{144}Nd$	n.a.	n.a.	n.a.	n.a.	n.a.	n.a.	n.a.	n.a.	n.a.	n.a.

APPENDIX C: Whole Rock Compositions

Element	44A	44B	44C	44D	44E	45A	45B	45C	46A	46B
					Tepv					
wt%:										
SiO2	44.83	45.03	47.29	45.04	43.89	47.91	48.34	44.30	44.73	44.93
TiO2	2.75	2.29	1.58	2.65	2.84	2.12	2.09	3.14	2.85	2.95
Al2O3	16.31	17.34	19.31	17.15	16.20	17.95	18.65	15.42	15.58	16.06
Fe2O3	9.57	8.27	6.73	9.12	9.74	7.67	7.53	10.24	9.51	10.07
MnO	0.16	0.15	0.14	0.19	0.16	0.13	0.13	0.15	0.15	0.15
MgO	3.72	2.88	1.57	3.05	4.76	2.72	2.44	4.19	4.25	3.84
CaO	9.35	9.08	6.15	8.58	9.71	7.54	6.59	10.31	10.55	9.54
Na2O	3.32	3.69	6.87	5.04	2.83	3.91	5.71	4.22	4.31	4.76
K2O	3.49	3.50	3.08	2.85	3.30	3.74	3.89	2.97	3.12	3.42
P2O5	1.18	0.89	0.50	1.07	1.27	0.82	0.79	1.50	1.70	1.45
LOI	4.47	5.47	5.88	4.46	4.05	4.27	2.59	2.44	2.19	1.80
Total	99.14	98.59	99.11	99.20	98.75	98.78	98.76	98.87	98.94	98.97
ppm:										
V	146	102	29	122	167	90	84	220	194	210
Sc	n.a.	n.d.	n.d.	n.a.	n.a.	1.7	1.3	5.1	n.a.	n.a.
Cr	n.a.	5	n.d.	n.a.	n.a.	5	n.d.	n.d.	n.a.	n.a.
Ni	24	16	5	22	28	26	16	54	49	46
Cu	154	134	118	156	164	109	119	150	116	140
Zn	96	95	83	103	95	84	87	103	96	103
Ga	20	22	21	21	24	21	23	22	24	23
As	n.a.	4	3	n.a.	n.a.	4	n.d.	n.d.	n.a.	n.a.
Rb	105	78.1	29.0	31.4	75.5	75.6	82.1	58.0	76.9	80.5
Sr	2460	4336	2360	2216	2905	4317	3357	2767	2728	2525
Y	33	29	25	32	32	27	29	36	36	34
Zr	321	324	300	320	314	314	326	326	327	318
Nb	139	153	168	137	131	156	162	121	127	129
Mo	2.6	n.d.	n.d.	n.d.	2.2	n.d.	2.6	2.1	2.3	3.6
Sb	n.a.	0.05	0.20	n.a.	n.a.	0.15	0.12	0.09	n.a.	n.a.
Cs	n.a.	n.d.	n.d.	n.a.	n.a.	n.d.	n.d.	n.d.	n.a.	n.a.
Ba	3405	3571	3968	3323	3355	4896	4043	3014	3083	3229
La	n.a.	128	117	n.a.	n.a.	121	123	128	n.a.	n.a.
Ce	n.a.	229	199	n.a.	n.a.	211	217	233	n.a.	n.a.
Nd	n.a.	77	73	n.a.	n.a.	83	77	98	n.a.	n.a.
Sm	n.a.	13.3	10.0	n.a.	n.a.	12.2	12.3	16.3	n.a.	n.a.
Eu	n.a.	3.75	3.10	n.a.	n.a.	3.52	3.60	4.44	n.a.	n.a.
Tb	n.a.	1.26	0.93	n.a.	n.a.	1.14	1.16	1.51	n.a.	n.a.
Yb	n.a.	2.30	2.00	n.a.	n.a.	2.04	2.22	2.19	n.a.	n.a.
Lu	n.a.	0.274	0.248	n.a.	n.a.	0.249	0.262	0.273	n.a.	n.a.
Hf	n.a.	5.87	5.01	n.a.	n.a.	5.86	5.72	6.91	n.a.	n.a.
Ta	n.a.	8.99	9.29	n.a.	n.a.	8.80	9.13	7.42	n.a.	n.a.
Pb	11	16	15	11	11	16	15	13	13	12
Th	n.a.	31.8	34.0	n.a.	n.a.	31.6	32.2	24.6	n.a.	n.a.
U	n.a.	n.d.	n.d.	n.a.	n.a.	n.d.	n.d.	n.d.	n.a.	n.a.
Au	n.a.	n.a.	n.a.	n.a.	n.a.	n.a.	n.d.	n.d.	n.a.	n.a.
Ag	n.a.	n.a.	n.a.	n.a.	n.a.	n.a.	n.d.	n.d.	n.a.	n.a.
$^{143}Nd/^{144}Nd$	n.a.	n.a.	n.a.	n.a.	n.a.	n.a.	n.a.	n.a.	n.a.	n.a.

APPENDIX C: Whole Rock Compositions

Element	47A	47B	47C	51A	51B	51C	51D	51E	51F	51H
					Tepv					
wt%:										
SiO2	47.04	43.69	44.01	44.03	43.91	46.74	44.82	43.37	43.87	48.30
TiO2	2.51	2.95	2.75	3.10	3.12	2.63	2.79	3.23	3.11	1.98
Al2O3	17.18	16.13	16.50	15.69	15.98	17.09	17.04	15.61	15.37	18.81
Fe2O3	8.81	9.80	9.50	10.32	10.25	9.16	9.34	10.65	10.42	7.61
MnO	0.16	0.16	0.16	0.17	0.16	0.16	0.16	0.16	0.17	0.14
MgO	2.96	3.65	4.27	4.28	4.65	2.96	3.33	4.30	4.14	2.24
CaO	8.08	9.33	8.96	10.78	9.67	7.51	8.01	9.63	10.43	6.38
Na2O	4.75	4.67	3.30	3.40	3.62	5.44	4.43	5.34	3.43	4.97
K2O	4.38	2.81	4.09	2.87	3.37	4.34	4.68	2.28	3.59	5.56
P2O5	1.05	1.29	1.18	1.34	1.39	1.01	1.05	1.53	1.49	0.64
LOI	1.92	3.90	4.27	3.01	2.82	1.65	2.76	2.63	2.59	2.47
Total	98.85	98.38	98.98	98.98	98.95	98.68	98.41	98.73	98.60	99.10
ppm:										
V	133	194	165	218	220	127	170	238	225	63
Sc	n.a.	n.a.	n.a.	n.a.	n.a.	2.1	n.a.	n.a.	5.0	n.a.
Cr	n.a.	n.a.	n.a.	n.a.	n.a.	n.d.	n.a.	n.a.	n.d.	n.a.
Ni	17	25	23	34	37	14	14	52	34	8
Cu	210	171	217	165	131	226	218	120	193	220
Zn	97	99	95	97	102	106	110	101	106	93
Ga	22	19	26	21	20	23	24	20	21	23
As	n.a.	n.a.	n.a.	n.a.	n.a.	n.a.	n.a.	n.a.	8	n.a.
Rb	92.9	59.6	82.8	44.6	103	98.7	104	37.0	96.1	125
Sr	2729	2166	2669	2218	2548	2536	2477	1795	3030	2821
Y	32	35	35	35	35	31	32	37	35	27
Zr	341	335	340	347	347	351	346	350	334	314
Nb	151	135	139	135	141	159	156	138	132	162
Mo	4.7	4.8	4.2	5.1	3.2	4.6	3.9	3.0	4.6	4.4
Sb	n.a.	n.a.	n.a.	n.a.	n.a.	0.05	n.a.	n.a.	0.06	n.a.
Cs	n.a.	n.a.	n.a.	n.a.	n.a.	n.d.	n.a.	n.a.	n.d.	n.a.
Ba	3525	3040	3368	2887	3233	3576	3392	2794	3172	4138
La	n.a.	n.a.	n.a.	n.a.	n.a.	133	n.a.	n.a.	133	n.a.
Ce	n.a.	n.a.	n.a.	n.a.	n.a.	239	n.a.	n.a.	243	n.a.
Nd	n.a.	n.a.	n.a.	n.a.	n.a.	82	n.a.	n.a.	93	n.a.
Sm	n.a.	n.a.	n.a.	n.a.	n.a.	14.1	n.a.	n.a.	15.8	n.a.
Eu	n.a.	n.a.	n.a.	n.a.	n.a.	3.96	n.a.	n.a.	4.39	n.a.
Tb	n.a.	n.a.	n.a.	n.a.	n.a.	1.38	n.a.	n.a.	1.52	n.a.
Yb	n.a.	n.a.	n.a.	n.a.	n.a.	2.16	n.a.	n.a.	2.17	n.a.
Lu	n.a.	n.a.	n.a.	n.a.	n.a.	0.260	n.a.	n.a.	0.283	n.a.
Hf	n.a.	n.a.	n.a.	n.a.	n.a.	6.42	n.a.	n.a.	6.59	n.a.
Ta	n.a.	n.a.	n.a.	n.a.	n.a.	9.14	n.a.	n.a.	7.93	n.a.
Pb	16	11	13	12	13	16	15	13	14	16
Th	n.a.	n.a.	n.a.	n.a.	n.a.	27.1	n.a.	n.a.	28.0	n.a.
U	n.a.	n.a.	n.a.	n.a.	n.a.	n.d.	n.a.	n.a.	n.d.	n.a.
Au	n.a.	n.a.	n.a.	n.a.	n.a.	n.d.	n.a.	n.a.	n.a.	n.a.
Ag	n.a.	n.a.	n.a.	n.a.	n.a.	n.d.	n.a.	n.a.	n.a.	n.a.
$^{143}Nd/^{144}Nd$	n.a.	n.a.	n.a.	n.a.	n.a.	n.a.	n.a.	n.a.	n.a.	n.a.

APPENDIX C: Whole Rock Compositions

Element	94NM2A	94NM2B	94NM2C	NM1105av
		Tepv		
wt%:				
SiO2	42.76	43.03	40.11	42.81
TiO2	2.95	3.10	3.39	2.95
Al2O3	15.73	15.70	14.80	14.43
Fe2O3	10.11	10.34	11.06	10.37
MnO	0.17	0.18	0.17	0.17
MgO	3.80	3.80	4.21	5.13
CaO	10.62	10.23	10.47	10.56
Na2O	4.20	3.66	4.10	3.18
K2O	2.15	2.93	2.05	2.80
P2O5	1.48	1.37	1.48	1.30
LOI	4.94	5.23	4.83	4.92
Total	98.91	99.57	96.67	98.62
ppm:				
V	163	144	190	163
Sc	5.0	3.6	5.8	7.5
Cr	5	n.d.	8	72
Ni	34	24	34	60
Cu	155	212	166	138
Zn	90	107	88	89
Ga	22	19	20	20
As	n.a.	n.a.	n.a.	n.a.
Rb	58.0	47.0	17.0	74.0
Sr	2022	2522	2273	2266
Y	34	34	34	31
Zr	321	322	309	298
Nb	123	115	105	101
Mo	n.a.	n.a.	n.a.	n.a.
Sb	0.11	0.12	0.10	0.12
Cs	n.d.	n.d.	n.d.	n.d.
Ba	3124	3291	2515	2811
La	126	133	125	115
Ce	234	240	232	207
Nd	96	93	92	76
Sm	15.1	15.6	15.4	14.0
Eu	4.37	4.46	4.39	3.97
Tb	1.45	1.45	1.48	1.36
Yb	2.12	2.23	2.18	1.97
Lu	0.255	0.267	0.255	0.261
Hf	6.35	6.48	6.74	6.06
Ta	7.48	7.90	6.87	6.68
Pb	12	9	9	11
Th	26.8	26.7	24.5	23.4
U	6.9	6.4	4.9	6.3
Au	n.a.	n.a.	n.a.	n.a.
Ag	n.a.	n.a.	n.a.	n.a.
$^{143}Nd/^{144}Nd$	n.a.	n.a.	n.a.	n.a.

APPENDIX D: Pyroclastic deposits stratigraphic column

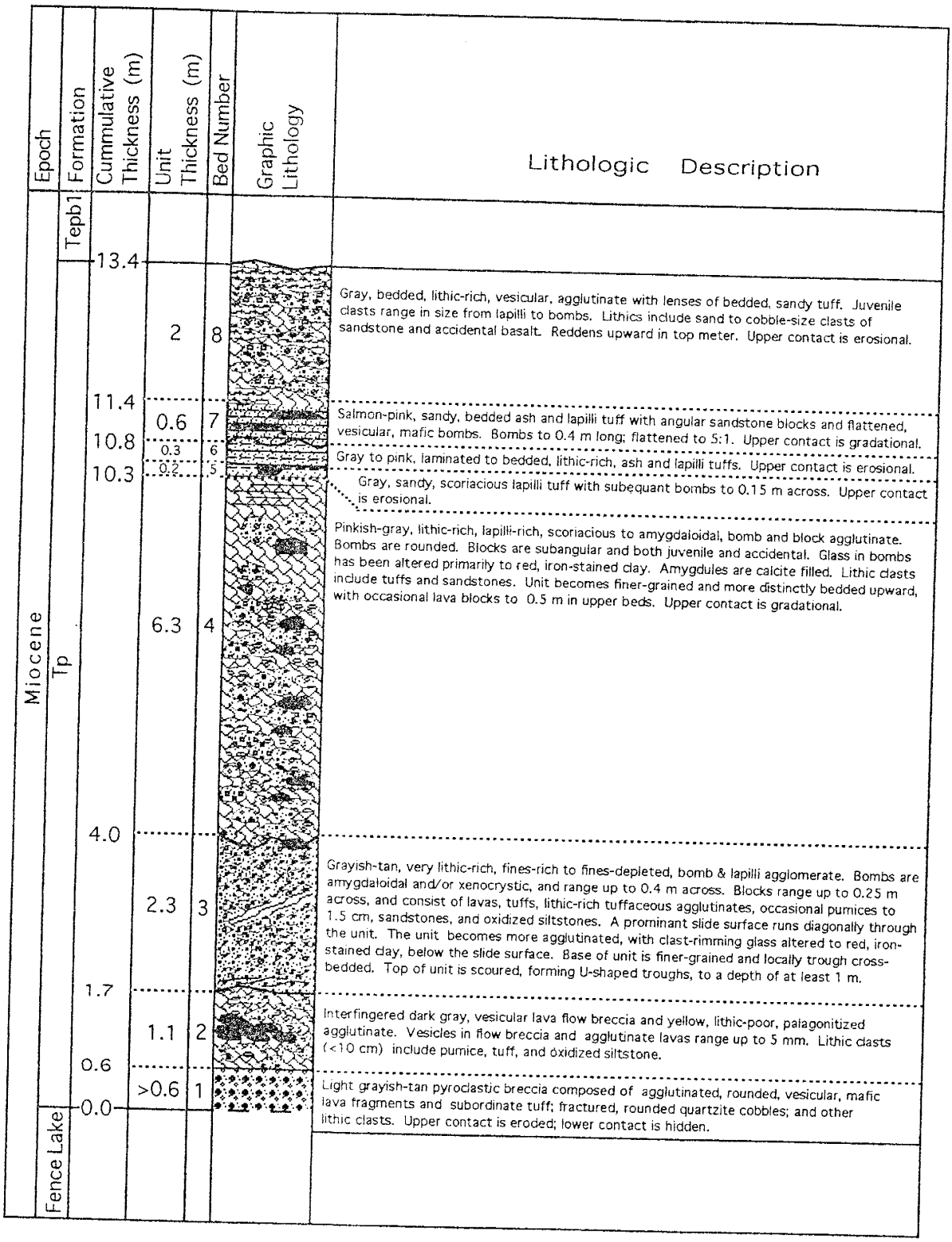

APPENDIX E: Sample Locations

This appendix includes a list of the locations of samples described in Appendices A through C. Locations are plotted on the Sample Location Map (Plate 1), which is in the jacket pocket.

APPENDIX E: Sample Locations

Sample	Unit	Location
1A, 1B	Tepv, Tepb2	Loose clast, E side, El Porticito
2	Tepv	In situ, base of cliff, E side, El Porticito
5A, 5B	Tepv, Tepb2	In situ, base of cliff, E side, El Porticito
6A	Tepv	In situ, base of cliff, N end, El Porticito
6B	Tepb2	In situ, base of cliff, N end, El Porticito
7A	Tepv	In situ, base of cliff, N end, El Porticito
7B	Tepb2	In situ, base of cliff, N end, El Porticito
8A	Tepv	In situ, base of cliff,S-central Tejana Mesa
8B	Tepb2	In situ, base of cliff,S-central Tejana Mesa
8C	Tepv, Tepb2	In situ, base of cliff,S-central Tejana Mesa
11B	Tepb2	In situ, upper W side, El Porticito
15	Tepv	In situ, top of cliff, E side El Porticito
19A	Tepb1	In situ, top of S end, El Porticito
19B	Tepb2	In situ, near top of S end, El Porticito
20	Tepb1	In situ, top of central El Porticito
21	Tepv	In situ, top of central El Porticito
23B	Tepv	In situ, base of cliff,S-central Tejana Mesa
23C	Tepb2	In situ, base of cliff,S-central Tejana Mesa
24	Tepb2	In situ, base of cliff,S-central Tejana Mesa
25A	Tepb1	In situ, base of cliff,S-central Tejana Mesa
25B	Tepv	In situ, base of cliff,S-central Tejana Mesa
25C	Tepb2	In situ, base of cliff,S-central Tejana Mesa
27C	Tepv	In situ, SE corner, Tejana Mesa
27D	Tepv	In situ, SE corner, Tejana Mesa
28	Tepb1	In situ, SE corner, Tejana Mesa
29	Tepb1	In situ, SE corner, Tejana Mesa
37A	Tepb2	In situ, near top, W side El Porticito
37B	Tepv	In situ, near top, W side El Porticito
37C	Tepv	In situ, near top, W side El Porticito
37D	Tepv	In situ, near top, W side El Porticito
37E	Tepv	In situ, near top, W side El Porticito
37F	Tepb2	In situ, near top, W side El Porticito
37G	Tepb2	In situ, near top, W side El Porticito
37H	Tepv	In situ, near top, W side El Porticito
37I	Tepv	In situ, near top, W side El Porticito
37J	Tepv	In situ, near top, W side El Porticito
37K	Tepb2	In situ, near top, W side El Porticito
39AB	Tepb1	In situ, S end, E side, El Porticito
41A	Tepv	Loose clast, E side, El Porticito
41B	Tepv	Loose clast, E side, El Porticito
42	Tepv	Loose clast, E side, El Porticito
43A	Tepv	Loose clast, E side, El Porticito
43B	Tepv	Loose clast, E side, El Porticito
43C	Tepv	Loose clast, E side, El Porticito
43D	Tepv	Loose clast, E side, El Porticito
44A	Tepv	In situ, base of cliff, N end, El Porticito
44B	Tepv	Loose clast, N end, El Porticito
44C	Tepv	Loose clast, N end, El Porticito
44D	Tepv	Loose clast, N end, El Porticito
44E	Tepv	Loose clast, N end, El Porticito
44F	Tepb2	Loose clast, N end, El Porticito
45A	Tepv	In situ, base of cliff, N end, El Porticito
45B	Tepv	In situ, base of cliff, N end, El Porticito
45C	Tepv	In situ, base of cliff, N end, El Porticito
46A	Tepv	Loose clast, S-central Tejana Mesa
46B	Tepv	Loose clast, S-central Tejana Mesa
47A	Tepv	Loose clast, S-central Tejana Mesa
47B	Tepv	Loose clast, S-central Tejana Mesa
47C	Tepv	Loose clast, S-central Tejana Mesa
49E	Tp	In situ, SW corner, Tejana Mesa
49F	Tepb1	In situ, SW corner, Tejana Mesa
51A	Tepv	Loose clast, SW Tejana Mesa
51B	Tepv	Loose clast, SW Tejana Mesa
51C	Tepv	Loose clast, SW Tejana Mesa
51D	Tepv	Loose clast, SW Tejana Mesa
51E	Tepv	Loose clast, SW Tejana Mesa
51F	Tepv	Loose clast, SW Tejana Mesa
51H	Tepv	Loose clast, SW Tejana Mesa
55	Tepb1	In situ, top, SE corner, Tejana Mesa
56	Tepb2	In situ, base of cliff, SE Tejana Mesa
58	Tepb2	In situ, near top, SW corner, Tejana Mesa
NM1104av	Tepb2	Loose clast, E side, El Porticito
NM1105av	Tepv	Loose clast, E side, El Porticito
94NM2A	Tepv	Loose clast, E side, El Porticito
94NM2B	Tepv	Loose clast, E side, El Porticito
94NM2C	Tepv	Loose clast, E side, El Porticito

REFERENCES

Aoki, K. I., 1964. Clinopyroxenes from alkaline rocks of Japan. *American Mineralogist* 49, 1199-1223.

Arzi, A. A., 1978. Critical phenomena in the rheology of partially melted rocks. *Tectonophysics* 44, 173-184.

Aubele, J. C., Crumpler, L. S. & Elston, W. E., 1988. Vesicle zonation and vertical structure of basalt flows. *Journal of Volcanology and Geothermal Research* 35, 349-374.

Baldridge, W. S., 1979. Mafic and ultramafic inclusion suites from the Rio Grande rift (New Mexico) and their bearing on the composition and thermal state of the lithosphere. *Journal of Volcanology and Geothermal Research* 6, 319-351.

Baldridge, W. S., 1994. Petrographic summary of Late Miocene volcanic rocks of El Porticito. In: Chamberlin, R. M., Kues, B. S., Cather, S. M., Barker, J. M. & McIntosh, W. C. (eds.) *Mogollon Slope, West-Central New Mexico and East-Central Arizona.* New Mexico Geological Society, p 61.

Baldridge, W. S., Perry, F. V., Nealey, L. D., Laughlin, A. W. & Wohletz, K. H., 1989. Field guide to excursion 8A: Oligocene to Holocene magmatism and extensional tectonics, central Rio Grande rift and southeastern Colorado Plateau, New Mexico and Arizona. In: Chapin, C. E. and Zidek, J. (eds.) *Field excursions to volcanic terranes in the western United States,*

Volume I: Southern Rock Mountain region, Memoir 46. New Mexico Bureau of Mines and Mineral Resources, Socorro, NM, p219.

Barksdale, J. D., 1937. The Shonkin Sag laccolith. *American Journal of Science* 33, 321-359.

Barksdale, J. D., 1952. The pegmatite layer in the Shonkin Sag laccolith, Montana. *American Journal of Science* 250, 705-720.

Bryan, W. B., Finger, L. W. & Chayes, F., 1969. Estimating proportions in petrographic mixing equations by least-squares approximation. *Science* 163, 926-927.

Bugbee, E. E., 1940. *A Textbook of Fire Assaying.* New York: John Wiley & Sons.

Carmichael, I. S. E., Nicholls, J. & Smith, A. L., 1970. Silica activity in igneous rocks. *American Mineralogist* 55, 246-263.

Carmichael, I. S. E., Turner, F. J. & Verhoogen, J., 1974. *Igneous Petrology.* New York: McGraw-Hill.

Caroff, M., Maury, R. C., Leterrier, J., Joron, J. L., Cotten, J. & Guille, G., 1993. Trace element behavior in the alkali basalt-comenditic trachyte series from Mururoa Atoll, French Polynesia. *Lithos* 30, 1-22.

Cas, R. A. F. & Wright, J. V., 1993. *Volcanic Successions Modern and Ancient,* London: Chapman & Hall.

Chamberlin, R. M., Cather, S. M., Anderson, O. J. & Jones, G. E., 1994. *Reconnaissance geologic map of the Quemado 30 × 60 minute*

quadrangle, Catron County, New Mexico. Open File Report 406, New Mexico Bureau of Mines and Mineral Resources, Socorro, New Mexico.

Chapin, C. E., Chamberlin, R. M., Osborn, G. R., Sanford, A. R. & White, D. W., 1978. Exploration framework of the Socorro geothermal area, New Mexico. In: Chapin, C. E. and Elston, W. E. (eds.) *Field Guide to Selected Cauldrons and Mining Districts of the Datil-Mogollon Volcanic Field New Mexico.* New Mexico Geological Society, Special Publication No. 7, 114-129.

Dalrymple, G. B., Alexander, E. C., Jr., Lanphere, M. A. & Kraker, G. P., 1981. Irradiation of samples for $^{40}Ar/^{39}Ar$ dating using the Geological Survey TRIGA reactor. U.S.G.S. Professional Paper 1176.

Davis, P. M., Parker, E. C., Evans, J. R., Iyer, H. M. & Olson, K. H., 1984. Teleseismic deep sounding of the velocity structure beneath the Rio Grande rift. In: Baldridge, W. S., Dickerson, P. W., Riecker, R. E. & Zidek, J. (eds.) *Rio Grande Rift: Northern New Mexico,* New Mexico Geological Society, p29.

Decker, R. W., 1987. Dynamics of Hawaiian volcanoes: an overview. In: Decker, R. W., Wright, T. L. & Stauffer, P. H. (eds.) *Volcanism in Hawaii.* U.S.G.S. Professional Paper 1350, pp 1395-1447.

Deer, W. A., Howie, R. A. & Zussman, J., 1992. *The Rock-Forming Minerals.* New York: Longman Scientific & Technical.

DePaolo, D. J., 1981. Neodymium isotopes in the Colorado Front Range and implications for crust formation and mantle evolution in the Proterozoic. *Nature* 291, 193-197.

Dethier, D. P., Aldrich, M. J., Jr. & Shafiqullah, M., 1986. New K-Ar ages for Miocene volcanic rocks from the northeastern Jemez Mountains and Tejana Mesa, New Mexico. *Isochron/West* 47, New Mexico Bureau of Mines and Mineral Resources, Socorro, New Mexico & Nevada Bureau of Mines and Geology, Reno, Nevada, 12-14.

Dunbar, N. W., Jacobs, G. K. & Naney, M. T., 1995. Crystallization processes in an artificial magma: variations in crystal shape, growth rate and composition with melt cooling history. *Contributions to Mineralogy and Petrology* 120, 412-425.

Frey, F. A., Green, D. H. & Roy, S. D., 1978. Integrated models of basalt petrogenesis: A study of quartz tholeiites to olivine melilitites from southeastern Australia utilizing geochemical and experimental petrological data. *Journal of Petrology* 19, 463-513.

Gibb, F. G. F., 1973. The zoned clinopyroxenes of the Shiant Isles Sill, Scotland. *Journal of Petrology* 14, 203-230.

Guilinger, D. R., 1982. Geology and Uranium Potential of the Tejana Mesa-Hubbell Draw area, Catron County, New Mexico. Unpublished New Mexico Institute of Mining and Technology MS thesis.

Hallett, R. B. & Kyle, P. R., 1993. XRF and INAA determinations of major and trace elements in Geological Survey of Japan igneous and sedimentary rock standards. *Geostandards Newsletter* 17, 127-133.

Hamilton, W., Hayes, P. T., Calvert, R., Smith, V. C., Elmore, P. S. D., Barnett, P. R. & Conklin, N., 1965. *Diabase Sheets of the Taylor Glacier Region Victoria Land, Antarctica.* U.S.G.S. Professional Paper 456-B.

Helz, R. T., Kirschenbaum, H., & Marinenko, J. W., 1989. Diapiric transfer of melt in Kilauea Iki lava lake, Hawaii: A quick, efficient process of igneous differentiation. *Geological Society of America Bulletin* 101, 578-594.

Höller, H. & Wirsching, U., 1978. Experiments on the formation of zeolites by hydrothermal alteration of volcanic glasses. In: Sand, L. B. & Mumpton, F. A. (eds.) *Natural Zeolites Occurrence, Properties, Use.* New York: Pergamon Press, pp 329-336.

Hurlbut, C. S. & Griggs, D. T., 1939. Igneous rocks of the Highwood Mountains, Montana: Part I. The Laccoliths. *Geological Society of America Bulletin.* 50, 1043-1112.

Iyengar, S., Jenkins, R. & Renault, J. R., in press. General Introduction. In: Buhrke, V. E., Jenkins, R. & Smith, D. K. (eds.) *Specimen Preparation in X-ray Fluorescence and X-ray Diffraction.* New York: John Wiley.

Karlstrom, K. E. & Bowring, S. A., 1993. Proterozoic orogenic history of Arizona. In: Van Schmus, R. A. & Bickford, M. E. (eds.) *Precambrian*

Coterminous United States. Geology of North America C-2. Boulder, Colorado: Geological Society of America, pp 188-211.

Karlstrom, K. E. & Daniel, C. G., 1993. Restoration of Laramide right-lateral strike slip in northern New Mexico by using Proterozoic piercing points: Tectonic implications from the Proterozoic to the Cenozoic. *Geology* 21, 1139-1142.

Keil, K, Fodor, R. V. & Bunch, T. E., 1972. Contributions to the mineral chemistry of Hawaiian rocks II. Feldspars and interstitial material in rocks from Haleakala and West Maui volcanoes, Maui, Hawaii. *Contributions to Mineralogy and Petrology* 37, 253-276.

Klein, K. & Hurlbut, C. S., Jr., 1993. *Manual of Mineralogy*. New York: John Wiley.

Köhler, T. P. & Brey, G. P., 1990. Calcium exchange between olivine and clinopyroxene calibrated as a geothermobarometer for natural peridotites from 2 to 60 kb with applications. *Geochimica et Cosmochimica Acta* 54, 2375-2388.

Kyle, P. R., 1981. Mineralogy and geochemistry of a basanite to phonolite sequence at Hut Point Peninsula, Antarctica, based on core from Dry Valley Drilling Project drillholes 1, 2 and 3. *Journal of Petrology* 22, 451-500.

Larsen, L. M., 1979. Distribution of REE and other trace elements between phenocrysts and peralkaline undersaturated magmas, exemplified by

rocks from the Gardar igneous province, South Greenland. *Lithos* 12, 303-315.

LeMaitre, R. W., 1989. *A Classification of Igneous Rocks and Glossary of Terms*. Oxford: Blackwell Scientific Publications.

Lemarchand, F., Villemant, B. & Calas, G., 1987. Trace element distribution coefficients in alkaline series. *Geochimica et Cosmochimica Acta* 51, 1071-1081.

Leung, I. S., 1974. Sector-zoned titanaugites: morphology, crystal chemistry, and growth. *American Mineralogist* 59, 127-138.

Lo, H. J., 1978. Composition and origin of analcime in taiwanite, a glassy basaltic rock in the Eastern Coastal Range, Taiwan. In: Sand, L. B. & Mumpton, F. A. (eds.) *Natural Zeolites Occurrence, Properties, Use*. New York: Pergamon Press, pp 303-307.

Lofgren, G. E., 1980. Experimental studies on the dynamic crystallization of silicate melts. In: Hargraves, R. B. (ed.) *Physics of Magmatic Processes.* Princeton: Princeton University Press, pp 487-551.

Lofgren, G. E., 1983. Effect of heterogeneous nucleation on basaltic textures: A dynamic crystallization study. *Journal of Petrology* 24, 229-255.

Mahood, G. A. & Cornejo, P. C., 1992. Evidence for ascent of differentiated liquids in a silicic magma chamber found in a granitic pluton. *Transactions of the Royal Society of Edinburgh: Earth Sciences* 83, 63-69.

Marsh, B. D., Gunnarsson, B. Congdon, R. & Carmody, R., 1991. Hawaiian basalt and Icelandic rhyolite: indicators of differentiation and partial melting. *Geologische Rundschau* 80/2, 481-510.

McDougall, I. & Harrison, T. M., 1988. *Geochronology and Thermochronology by the $^{40}Ar/^{39}Ar$ Method.* London: Oxford University Press.

McIntosh, W. C. & Cather, S. M., 1994. $^{40}Ar/^{39}Ar$ geochronology of basaltic rocks and constraints on Late Cenozoic stratigraphy and landscape development in the Red Hill-Quemado area, New Mexico. In: Chamberlin, R. M., Kues, B. S., Cather, S. M., Barker, J. M. & McIntosh, W. C. (eds.) *Mogollon Slope, West-Central New Mexico and East-Central Arizona.* New Mexico Geological Society, pp 209-215.

Meijer, A., Kwon, T. & Tilton, G. R., 1990. U-Th-Pb partitioning behavior during partial melting in the upper mantle: implications for the origin of high mu components and the "Pb Paradox". *Journal of Geophysical Research* 95-B1, 433-448.

Menzies, M. A., Kempton, P. & Dungan, M., 1985. Interaction of continental lithosphere and asthenospheric melts below the Geronimo Volcanic Field, Arizona, U.S.A. *Journal of Petrology* 26, 663-693.

Menzies, M. A., Kyle, P. R., Jones M. & Ingram, G., 1991. Enriched and depleted source components for tholeiitic and alkaline lavas from Zuni-Bandera, New Mexico: Inferences about intraplate processes and stratified lithosphere. *Journal of Geophysical Research* 96-B8, 13,645-13,671.

Minier, J. & Reiter, M., 1991. Heat flow on the southern Colorado Plateau. *Tectonophysics* 200, 51-66.

Moore, J. G. & Evans, B. W., 1967. The role of olivine in the crystallization of the prehistoric Makaophui tholeiitic lava lake, Hawaii. *Contributions to Mineralogy and Petrology* 15, 202-223.

Morimoto, N., 1988. Nomenclature of pyroxenes. *Mineralogy and Petrology* 39, 55-76.

Nakamura, N., 1974. Determination of REE, Ba, Fe, Mg, Na and K in carbonaceous and ordinary chondrites. *Geochimica et Cosmochimica Acta* 38, 757-775.

Nash, W. P. & Wilkinson, J. F. G., 1970. Shonkin Sag laccolith, Montana: I. Mafic minerals and estimates of temperature, pressure oxygen fugacity and silica activity. *Contributions to Mineralogy and Petrology* 25, 241-269.

Norrish, K. & Chappell, B. W., 1977. X-ray fluorescence spectrometry. In: Zussman, J. (ed.) *Physical Methods in Determinative Mineralogy*. London: Academic Press, pp. 201-273.

Osborne, F. F. & Roberts, E. J., 1931. Differentiation in the Shonkin Sag laccolith, Montana. *American Journal of Science* 22, 331-353.

Parker, E. C., Davis, P. M., Evans. J. R., Iyer, H. M. & Olsen, K. H., 1984. Upwarp of anomalous asthenosphere beneath the Rio Grande rift. *Nature* 312, 354-356.

Perry, F. V., Baldridge, W. S. & DePaolo, D. J., 1987. Role of Asthenosphere and lithosphere in the genesis of Late Cenozoic basaltic rocks from the Rio Grande Rift and adjacent regions of the Southwestern United States. *Journal of Geophysical Research* 92-B9, 9193-9213.

Peterson, D. W. & Moore, R. B., 1987. Geologic history and evolution of geologic concepts, Island of Hawaii. In: Decker, R. W., Wright, T. L. & Stauffer, P. H. (eds.) *Volcanism in Hawaii.* U.S.G.S. Professional Paper 1350, pp 149-189.

Philpotts, A. R., 1990. *Principles of Igneous and Metamorphic Petrology.* Englewood Cliffs, NJ: Prentice Hall.

Phillpotts, A. R. & Carroll, M., 1996. Physical properties of partly melted tholeiitic basalt. *Geology* 24, 1029-1032.

Philpotts, A. R., Carroll, M. & Hill, J. M., 1996. Crystal-mush compaction and the origin of pegmatitic segregation sheets in a thick flood-basalt flow in the Mesozoic Hartford Basin, Connecticut. *Journal of Petrology* 37, 811-836.

Pouchou, J. L. & Pichoir, F., 1985. "PAP" $\phi(\rho z)$ procedure for improved quantitative microanalysis. In: Armstrong, J. T. (ed.) *Microbeam Analysis—1985.* San Francisco: San Francisco Press.

Puffer, J. H. & Horter, D. L., 1993. Origin of pegmatitic segregation veins within flood basalts. *Geological Society of America Bulletin* 105, 738-748.

Reid, M. R., Hart, S. R., Padovani, E. R., & Wandless, G. A., 1989. Contribution of metapelitic sediments to the composition, heat production, and seismic velocity of the lower crust of southern New Mexico, U.S.A. *Earth and Planetary Science Letters* 95, 367-381.

Roden, M. F., Smith, D. & Murthy, V. R., 1990. Chemical constraints on lithosphere composition and evolution beneath the Colorado Plateau. *Journal of Geophysical Research* 95-B3, 2811-2831.

Rollinson, H., 1993. *Using Geochemical Data: Evaluation, Presentation, Interpretation.* New York: Longman Scientific & Technical.

Roybal, G. H., 1982. *Geology and coal resources of the Tejana Mesa quadrangle, Catron County, New Mexico.* Open File Report 178, New Mexico Bureau of Mines and Mineral Resources, Socorro, New Mexico.

Rudnick, R. L. & Fountain, D. M., 1995. Nature and composition of the continental crust: a lower crustal perspective. *Reviews of Geophysics* 33, 267-309.

Saemundsson, K., 1979. Outline of the geology of Iceland. *Jokull* 29, 7-28.

Slack, P. D., Davis, P. M., Baldridge, W. S., Olsen, K. H., Glahn, A., Achauer U. & Spence, W., 1996. The upper mantle structure of the central Rio Grande rift region from teleseismic P and S wave travel time delays and attenuation. *Journal of Geophysical Research* 101-B7, 16,003-16,023.

Spence, W. & Gross, R. S., 1990. A tomographic glimpse of the upper mantle source of magmas of the Jemez Lineament, New Mexico. *Journal of Geophysical Research* 95-B7, 10,829-10,849.

Stephenson, D., 1972. Alkali clinopyroxenes from nepheline syenites of the South Qôroq Center, south Greenland. *Lithos* 5, 187-201.

Stormer, J. C., Jr., 1973. Calcium zoning in olivine and its relationship to silica activity and pressure. *Geochimica et Cosmochimica Acta* 37, 1815-1821.

Stormer, J. C., Jr., 1983. The effects of recalculation on estimates of temperature and oxygen fugacity from analyses of multicomponent iron-titanium oxides. *American Mineralogist* 68, 586-594.

Sun, S. S. & McDonough, W. F., 1989. Chemical and isotopic systematics of oceanic basalts: implications for mantle composition and processes. In: Saunders, A. D. & Norry, M. J. (eds.) *Magmatism in the Ocean Basins.* Geological Society Special Publication 42, 313-345.

Takahashi, E., 1978. Partitioning of Ni^{2+}, Co^{2+}, Fe^{2+}, Mn^{2+}, and Mg^{2+} between olivine and silicate melts: compositional dependence of partition coefficient. *Geochimica et Cosmochimica Acta* 42, 1829-1844.

Tatsumi, Y., 1989. Migration of fluid phases and genesis of basalt magmas in subduction zones. *Journal of Geophysical Research* 94-B4, 4697-4707.

Thompson, R. N., 1972. Melting behavior of two Snake River lavas at pressures up to 35 kb. *Carnegie Institute Washington Geophysical Laboratory Yearbook* 71, 401-410.

Thompson, R. N., Morrison, M. A., Hendry, G. L. & Parry, S. J., 1984. An assessment of the relative roles of crust and mantle in magma genesis: an elemental approach. *Philosophical Transactions of the Royal Society of London* A310, 549-590.

Tschernich, R. W., 1992. *Zeolites of the World*, Phoenix, AZ: Geoscience Press, Inc.

van der Molen, I. & Paterson, M. S., 1979. Experimental deformation of partially-melted granite. *Contributions to Mineralogy and Petrology* 70, 299-318.

Watson, E. B., 1977. Partitioning of manganese between forsterite and silicate liquid. *Geochimica et Cosmochimica Acta* 41, 1363-1374.

Willard, M. E. & Weber, R. H., 1958. *Reconnaissance geologic map of Cañon Largo thirty-minute quadrangle*. Geologic Map 6, New Mexico Bureau of Mines and Mineral Resources, Socorro, New Mexico.

Wilson, M., 1989. *Igneous Petrogenesis*. London: HarperCollins Academic.

Wright, T. L. & Okamura, R. T., 1977. Cooling and crystallization of tholeiitic basalt, 1965 Makaopuhi lava lake, Hawaii. U. S. G. S. Professional Paper 1004.

Zindler, A. & Hart. S. R., 1986. Chemical geodynamics. *Annual Reviews in Earth and Planetary Science* 14, 493-571.

This thesis is accepted on behalf of the faculty

of the institute by the following committee:

Co-Advisor

Co-Advisor

29 August 1997

Date

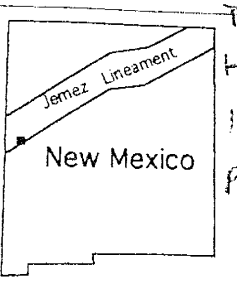

Location Map

Tejana Mesa

Mesa Tinaja fault zone

Largo Creek

7.17 +/- 0.70 Ma

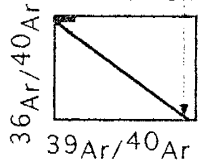

6.94 +/- 0.34 Ma

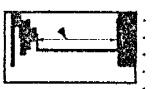

El Porticito

NM 601

Qal
Qco
Tepv
Tepb2
Ttmb
Tepb1
Tp

Qal Alluvium
Qco Colluvium and talus
Tepv Veins
Tepb2 Late basanite
Ttmb Basaltic flow
Tepb1 Early basanite
Tp Pyroclastic deposits

Symbols (dips in degrees)
14 Contact orientation
20 Bedding orientation
30 Vein orientation
39AB Sample location

Contacts (dashed where inferred, dotted where hidden)
Emplacement or depositional
Fault

13°
1972

0 100 200
Meters
Elevation in feet

El Porticito

Sample Location Map